UNIVERSIDAD AUTÓNOMA DE NUEVO LEÓN
FACULTAD DE CIENCIAS FÍSICO MATEMÁTICAS

STRUCTURAL, MICROSTRUCTURAL AND ELECTRICAL PROPERTIES OF YTTRIUM-DOPED BARIUM TITANATE FOR MULTILAYER CERAMIC CAPACITORS

POR
ANA MARÍA HERNÁNDEZ LÓPEZ

COMO REQUISITO PARCIAL PARA OBTENER EL GRADO DE DOCTOR EN INGENIERÍA FÍSICA INDUSTRIAL

OCTUBRE, 2018

UNIVERSIDAD AUTÓNOMA DE NUEVO LEÓN
FACULTAD DE CIENCIAS FÍSICO MATEMÁTICAS
CENTRO DE INVESTIGACIÓN EN CIENCIAS FÍSICO MATEMÁTICAS

STRUCTURAL, MICROSTRUCTURAL AND ELECTRICAL PROPERTIES OF YTTRIUM-DOPED BARIUM TITANATE FOR MULTILAYER CERAMIC CAPACITORS

POR

ANA MARÍA HERNÁNDEZ LÓPEZ

COMO REQUISITO PARCIAL PARA OBTENER EL GRADO DE DOCTOR EN INGENIERÍA FÍSICA INDUSTRIAL

SAN NICOLÁS DE LOS GARZA, NUEVO LEÓN, MÉXICO   OCTUBRE 2018

UNIVERSIDAD AUTÓNOMA DE NUEVO LEÓN

FACULTAD DE CIENCIAS FÍSICO MATEMÁTICAS

CENTRO DE INVESTIGACIÓN EN CIENCIAS FÍSICO MATEMÁTICAS

Los miembros del Comité de Tesis recomendamos que la Tesis "Structural, microstructural and electrical properties of yttrium-doped barium titanate for multilayer ceramic capacitors", realizada por la alumna ANA MARÍA HERNÁNDEZ LÓPEZ, con número de matrícula 1654647, sea aceptada para su defensa como opción al grado en Doctorado en Ingeniería Física Industrial.

El Comité de Tesis

Jorge Luis Menchaca Arredondo
Presidente

Juan Antonio Aguilar Garib
Secretario

Sophie Guillemet-Fritsch
Vocal

Félix Sánchez de Jesús
Vocal

Román Jabir Nava Quintero
Vocal

Dr. Romeo de Jesús Selvas Aguilar
Subdirector de Estudios de Posgrado
Centro de Investigación en Ciencias Físico Matemáticas

San Nicolás de los Garza, Nuevo León, octubre 2018

AGRADECIMIENTOS

Soy muy afortunada por haber podido tomar lo mejor de México y Francia para crecer profesional y personalmente. Agradezco a la Universidad Autónoma de Nuevo León y a la Universidad de Toulouse 3 – Paul Sabatier por el honor de ser doctoranda en ellas así como por el apoyo para el desarrollo de esta cotutela.

Quiero darle mis más sinceros agradecimientos por haber aportado enormemente a mi formación a la Dr. Sophie Guillemet-Fritsch, al Dr. Juan Antonio Aguilar Garib, al Dr. Zarel Valdez Nava y al Prof. Bernard Durand por haberme abierto las puertas y creer en mí para afrontar este importante reto asesorándome con tanta paciencia durante estos años. Muchas gracias por aportar tanto de ustedes a mi formación, por su disponibilidad y por haberme impulsado a crecer como persona y como profesional bajo su guía y apoyo constante. Mil gracias por las largas discusiones, por animarme siempre a ir un poco más lejos y a ver desde más puntos de vista, les debo mucho de mi crecimiento.

Al Dr. Christophe Tenailleau y al Dr. Pascal Dufour, muchas gracias por su apoyo y por brindarme su tiempo para valiosas discusiones y darme la oportunidad de aprender tanto de ustedes. Gracias por sus consejos y guía durante el desarrollo de mi tesis.

Duployer por su apoyo técnico para llevar a cabo mis experimentos. Con gran aprecio agradezco también a Ly, Nahum, Abdé, Romain, Precious, Mohamed, Guillaume, Cédric, Cyril, Mateusz, Hélène y Trong por su compañía, por los cafés compartidos, por su apoyo en los momentos difíciles y por las risas.

Gracias también a mis compañeros y maestros en el CICFIM por contribuir con sus enseñanzas a mi formación.

Un profundo agradecimiento a quienes me brindaron su amistad y apoyo durante estos años en Monterrey: Mónica, Roberto, Liz, Juan de Dios, Maricela, Armando, Jeane, Marco, Fernando, Oswaldo, David y Abraham, soy afortunada por poder contar con tanto cariño de su parte, gracias por tantos lindos momentos, por sus abrazos y sonrisas.

Amanda, gracias por haber entrado con tanta alegría en mi vida y permitirme ser parte de la tuya, gracias por tanto cariño y esa energía que ilumina más de lo que imaginas. Gracias por tus palabras siempre acompañadas de una gran y cálida sonrisa.

Codorniz, gracias por acogerme en tu hogar y compartir conmigo esa familia tan especial, por los abrazos y palabras reconfortantes, por tantas risas, por abrirme las puertas incondicionalmente y por no dejarme sola.

A todos aquellos que a pesar de la distancia siempre han estado conmigo, Papitas, Pardito, Diani, Flaquito, Cesitar, Carlitos, Lau, David, Félix, Karencita, Jenn, gracias por esta gran amistad que nos ha visto crecer y hacer nuestros sueños realidad, los quiero.

Siempre le agradeceré a la vida que durante estos años me haya dado el gran regalo de agrandar mi familia. Por su inmenso e incondicional apoyo, la fuerza que me dan, tanto cariño y alegría, por ayudarme a hacer mis sueños realidad y permitirme ser parte de sus vidas: *Gaby, Jime, Santi,*

Roberto, Pepe, Guille y MariaJo, merecen mi agradecimiento infinito por permitirme escribir estas palabras hoy, a ustedes les debo gran parte de este logro.

En mi querida Colombia siempre hallarán un pedazo inmenso de quien soy, de mi corazón: mi hermosa familia. ¿Cómo agradecer por tanto amor? *A mi abuelita, mis tías y tíos, a mis hermanitas y hermanitos prestados, a mis sobrinos, Yaneth y Yas*: son ustedes quienes a diario aparecen en mis pensamientos, gracias por iluminar mi vida con su existencia, gracias por apoyarme y creer siempre en mí. Gracias por dar tanto para mi felicidad, por animarme a soñar siempre en grande y recibirme en sus brazos cada vez y sin importar nada. Los amo inmensamente.

Al amor de mi vida, quien no permite que pase un solo día sin que tenga un motivo para enamorarme más y ser más feliz. Mi vida contigo es la luz de mis ojos, mis sueños a tu lado sólo logran ser más grandes y el mundo para mí es mejor desde que tú y yo vamos recorriéndolo de la mano. Es por ti *Rho* y por todo lo que nos espera, siempre juntos.

A quienes han dado todo de sí para que mis alas sean cada vez más grandes: *mis padres*. Gracias por apoyar mis decisiones y darme fuerza cuando dudo de ellas. Gracias por siempre estar a mi lado y creer lo suficiente en mí para que le dé sentido a todos estos años lejos de ustedes. Gracias por demostrarme su amor de tantas maneras, por cuidarme y cuidar de *mis angelitos perrunos* que tanto extraño. Los llevo conmigo siempre, cada paso que he dado y daré tendrá su huella.

CONVENTION DE COTUTELLE INTERNATIONALE DE THESE

Entre l'Université Toulouse III - Paul Sabatier, établissement public à caractère scientifique, culturel et professionnel –sis 118, route de Narbonne – 31062 TOULOUSE CEDEX 9,
représentée par son Président, Monsieur Bertrand MONTHUBERT,
ci-après dénommée « UPS ».

Et l'Université Autonome de Nuevo León établissement public à caractère scientifique, culturel et professionnel –sis Ave. Universidad s/n, Ciudad Universitaria, San Nicolás de los Garza, NL 66428,
représentée par son Président, Monsieur Jesús ANCER-RODRÍGUEZ,
ci-après dénommé « UANL ».

Ci-après dénommés les établissements partenaires

Vu le code de l'éducation, notamment les articles L121-3, L123-7 ; L612-7 ; D123-12 ;

Vu l'arrêté du 6 janvier 2005 modifié relatif à la création d'une procédure de cotutelle de thèse entre établissements d'enseignement supérieur français et étrangers ;

Vu l'arrêté du 7 août 2006 relatif à la formation doctorale ;

Vu l'arrêté du 7 août 2006 relatif aux modalités de dépôt, de signalement, de reproduction, de diffusion et de conservation des thèses ou des travaux présentés en soutenance en vue du doctorat ;

Vu la charte des thèses de l'Université de Toulouse (jointe à la présente convention)

Vu la délibération de la commission de la recherche du conseil académique de l'Université Toulouse III - Paul Sabatier en date du septembre 2013

vu L'Unversité Autonome de Nuevo Leon certifie : L'Université Autonome de Nuevo León est un établissement public d'enseignement supérieur, avec statut juridique complet et capacité, afin de créer, de conserver et de diffuser la connaissance et la culture au profit de la société, conformément aux statuts fixées dans le décret numéro 60 émis par le Honorable Congrès de l'état de Nuevo León publié le 7 juillet 1971.

Les établissements partenaires conviennent d'instituer une procédure de cotutelle internationale de thèse dans les conditions suivantes, aux fins de conforter la construction de l'espace européen de l'enseignement supérieur et de la recherche et de développer la coopération scientifique entre les équipes françaises et étrangères.

La présente convention concerne :

Mme, ~~Mlle, M~~. HERNANDEZ LOPEZ Ana Maria
Né(e) le 3 mars 1989 à Bogota
de nationalité Colombienne

Cocher la case :

X titulaire du Master in Industrial Physics Engineering

o dispensé(e) du Master et autorisé(e) à s'inscrire par dérogation accordée par le président de l'Université Toulouse III - Paul Sabatier sur proposition du responsable de l'école doctorale ....

Article I : Inscription

Les candidats à une préparation de doctorat en cotutelle internationale doivent satisfaire aux conditions d'inscription en thèse dans chacun des établissements partenaires.
La doctorante ou le doctorant doit s'inscrire obligatoirement chaque année dans les deux établissements.

La doctorante ou le doctorant est inscrit(e) à compter de l'année universitaire 2014/2015

1 - à l'Université Toulouse III - Paul Sabatier
en doctorat en Ingenierie Physique Industrial
relevant de l'école doctorale : Sciences de la Matière

ET

2 - à l'établissement d'enseignement supérieur partenaire de UANL................................
en Doctorat en Ingenierie Physique Industrial...

Le sujet de thèse déposé par la doctorante ou le doctorant est « Impact de phases secondaires sur les propriétés diélectriques de condensateurs multicouches à base de titanate de baryum »...

Article II : Droits d'inscription

La doctorante ou le doctorant acquitte les droits d'inscription

Cocher la case :

X dans l'établissement dans lequel sera effectuée la soutenance de thèse
o dans l'établissement dans lequel, il séjourne le plus longtemps, chaque année universitaire
o dans l'établissement de son pays d'origine

Article III : Encadrement de la thèse

La doctorante ou le doctorant effectue sa scolarité et ses travaux de recherche sous la responsabilité conjointe d'une directrice ou d'un directeur de thèse dans les deux établissements partenaires qui s'engagent à exercer pleinement leurs fonctions d'encadrement en collaboration avec leur homologue.

A l'Université Toulouse III - Paul Sabatier, la directrice ou le directeur de thèse est :
Mme Sophie Guillemet , Directrice de Recherches au CIRIMAT
Mr Zarel Valdez Nava , chargé de Recherches au LAPLACE

A l'établissement d'enseignement supérieur partenaire, la directrice ou le directeur de thèse est :
Mr Juan Antonio Aguilar Garib

Article IV : Durée de la thèse

La durée de préparation de la thèse est normalement de trois ans. Cette durée peut être prolongée sur proposition conjointe des directeurs de thèse. Au dlà de 4 mois de cette échéance, il est impératif de prévoir les modalités de la prolongation de la thèse en cotutelle par avenant à la présente.

Article V : Calendrier de la thèse
La doctorante ou le doctorant effectue sa scolarité et ses travaux de recherche en alternance entre les deux établissements, par **périodes déterminées d'un commun accord** entre les deux directrices ou directeurs de thèse, selon les modalités suivantes :

Périodes prévisionnelles à l'Université Toulouse III - Paul Sabatier (indiquer les années et cocher les cases correspondant aux mois où la doctorante ou le doctorant sera présent(e)).

Années	Oct	Nov	Déc	Jan	Fev	Mar	Avr	Mai	Juin	Juil	Aout	Sept
2014/2015												X
2015/2016	X	X	X	X								X
2016/2017	X	X	X									X

2017/2018	X	X										

Périodes prévisionnelles dans l'établissement partenaire : UANL

Années	Oct	Nov	Déc	Jan	Fev	Mar	Avr	Mai	Juin	Juil	Aout	Sept
2014/2015					X	X	X	X	X	X	X	
2015/2016					X	X	X	X	X	X	X	
2016/2017				X	X	X	X	X	X	X	X	
2017/2018			X	X								

Article VI : Frais de mission

Les frais d'hébergement et de bouche sont à la charge du doctorant ou de la doctorante qui atteste avoir les moyens de subvenir à ses moyens de subsistance dans chacun des pays des établissements partenaires.
Ses frais de transports entre les établissements partenaires seront pris en charge de la manière suivante :
  • PCP-RU2I Programme de coopération international. Réseau Universitaire Franco-Mexicain
Les frais de transports des co-directeurs entre les établissements partenaires sont pris en charge par leur employeur.

Article VII : Couverture sociale et responsabilité civile

La doctorante ou le doctorant bénéficie de la couverture sociale inhérente à l'acquittement des droits de scolarité dans l'un des établissements partenaires *(cocher la case correspondante et compléter avec les années en cas d'alternance de régime)* :

o adhésion à la Sécurité Sociale régime étudiant   o français ou o étranger
o adhésion au Régime général de Sécurité Sociale (cas des salariés)
X un autre régime *(préciser et joindre le justificatif)* : Assurée par l'ISSSTE (CONACYT)

En tout état de cause, la doctorante ou le doctorant souscrit une assurance- responsabilité civile : (joindre l'attestation d'assurance).

Article VIII : Langue

La thèse sera rédigée et soutenue en langue :(cocher la case correspondante, sachant que lorsque cette langue n'est pas le français, la rédaction est complétée par un résumé substantiel en langue française).
o Française   X autre : Anglais

Un résumé substantiel de la thèse sera rédigé et présenté en langue :
X Française   o autre : Anglais

Tout étudiant non francophone qui s'inscrit dans une école doctorale de l'Université Toulouse III - Paul Sabatier sera tenu de suivre des enseignements de français langue étrangère. Le niveau de maîtrise de la langue française est apprécié au regard du Cadre européen commun de référence pour les langues (CECRL), dont le niveau B2 est exigible lors de la soutenance.

Article IX : Soutenance

La soutenance de la thèse est unique et reconnue par les deux établissements partenaires. L'établissement de soutenance, désigné d'un commun accord est :
o l'Université Toulouse III - Paul Sabatier
X l'établissement d'enseignement supérieur de : UANL

3/5

La répartition des frais occasionnés par la soutenance est déterminée conjointement par les deux établissements, selon les modalités suivantes : **PCP-RU2I**

....

....

....

....

L'admission en soutenance sera décidée conjointement par les chefs d'établissement concernés au terme d'une procédure préalable.

Cet examen est engagé sur avis conjoint des directeurs de recherche et fait intervenir une évaluation par au moins deux rapporteurs. Un rapporteur sera choisi par l'établissement partenaire, l'autre par l'Université Toulouse III - Paul Sabatier.

Les deux rapporteurs sont désignés conjointement par les deux établissements partenaires parmi des personnalités extérieures aux universités d'inscription.
Un rapport est rédigé en français ou traduit en français, dans ce dernier cas la traduction est authentifiée par les codirecteurs.

Article X : Jury

Le jury de soutenance, désigné par les deux établissements partenaires, est composé sur la base d'une proportion équilibrée de membres de chaque établissement. En cas de désaccord sur la composition du jury, la décision appartient au Président de l'établissement dans lequel a lieu la soutenance de la thèse.
Il comprend de quatre à huit membres dont les deux directeurs de thèse.
Le jury élit en son sein un président dont la voix est prépondérante en cas de partage.

Le jury établit après délibération un procès-verbal consignant sa décision et un rapport relatant le déroulement de la soutenance. Le procès-verbal est établi dans les deux langues officielles des établissements de tutelle. Il comporte les propositions de mention et distinctions pertinentes à l'Université Toulouse III - Paul Sabatier et à l'établissement d'enseignement supérieur de UANL...

Article XI : Délivrance et reconnaissance des diplômes de doctorat

Après soutenance de la thèse, les établissements partenaires délivrent à l'étudiant :
o un diplôme de docteur qu'ils confèrent conjointement ;
X simultanément un diplôme de docteur de chacun d'entre eux.

Le ou les diplômes de docteur sont délivrés par les autorités académiques habilitées à le faire, sur proposition conforme du jury, après la soutenance de la thèse ;
Sur le ou les diplômes de docteur figurent une indication de spécialité ou de discipline, le titre de la thèse ou l'intitulé des principaux travaux, la mention de la cotutelle internationale, les noms et titres des membres du jury et la date de soutenance.

Dans chaque pays, la protection du sujet, le dépôt, le signalement et la reproduction de la thèse seront effectués selon la réglementation en vigueur.

Article XII : Modifications et résiliation

Il est de la responsabilité de la doctorante ou du doctorant d'informer **par écrit** les responsables de l'école doctorale des changements apportés à la présente convention.

La convention est résiliée de plein droit en cas d'absence d'inscription de la doctorante ou du doctorant constatée par l'un ou l'autre établissement.

Elle l'est également en cas de renonciation recueillie par l'un des deux établissements. Dans ce cas, la doctorante ou le doctorant est tenu d'en informer ses deux directeurs de recherche ainsi que les responsables des écoles doctorales

Fait en 2 exemplaires originaux

Université Toulouse III - Paul Sabatier	Établissement partenaire
Le Président de l'Université Toulouse III - Paul Sabatier M. Bertrand MONTHUBERT Nom, Signature et cachet de l'établissement L'Administrateur Provisoire Amal SAYAH Date : 2 2 OCT. 2015	Le Président de l'Universidad Autónoma de Nuevo León M. Jesús ANCER-RODRÍGUEZ Nom, Signature et cachet de l'établissement Date : 24 de Sept. 2015 RECTORIA
Le directeur ou la directrice de thèse de l'Université Toulouse III - Paul Sabatier Mme. Sophie GUILLEMET — Nom, Signature FRITSCH Date : 1|07|2015	Le directeur ou la directrice de thèse de l'Universidad Autónoma de Nuevo León M. Juan Antonio AGUILAR GARIB Nom de l'établissement partenaire Nom, Signature Date : 17 /o7 / 2o15
Le directeur ou la directrice de l'école doctorale de rattachement : M. Eric BENOIST .... Nom, Signature Date : 13/10/15	Le directeur ou la directrice de l'école doctorale de rattachement (ou équivalent) : M. Rogelio J. SEPÚLVEDA GUERRERO .... Nom, Signature Date :

Signature du doctorant ou de la doctorante :

Mme. Ana María HERNÁNDEZ LÓPEZ

Avenant à la convention de cotutelle de thèse
Amendment to the joint doctoral supervision agreement

LE PRESENT AVENANT fait suite à la convention de cotutelle conclue entre l'Universidad Autónoma de Nuevo León et l'Université Toulouse III Paul Sabatier signée le 22 octobre 2015.

The PRESENT AMENDMENT follows the cotutelle agreement signed between the Universidad Autónoma de Nuevo León and the University Toulouse III Paul Sabatier; on October 22nd, 2015.

- AU PROFIT DE Mme. Ana María HERNÁNDEZ LÓPEZ (Doctorant)
- *FOR Ms. Ana María HERNÁNDEZ LÓPEZ (Doctorate)*
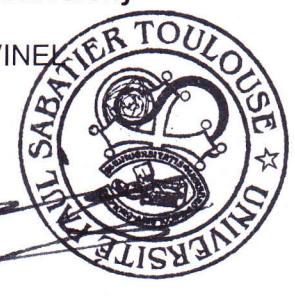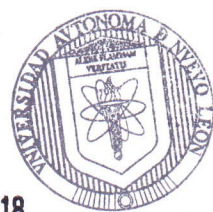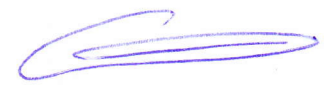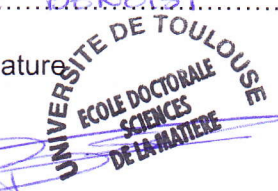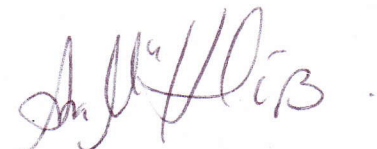
La durée de la thèse est prolongée de 8 mois
The duration of the thesis is extended for 8 months.

La soutenance aura lieu au mois de octobre 2018.
The defense will take place in October 2018.

Done in 2 original copies

Paul Sabatier - Toulouse III University	Partner Institution
President of Paul Sabatier - Toulouse III University M. Jean Pierre VINEL Date:	**Rector de la Universidad Autónoma de Nuevo León** M. Rogelio G. GARZA RIVERA Date: 0 1 JUN. 2018 RECTORIA
Thesis supervisor at Paul Sabatier - Toulouse III University Name, signature Mme. Sophie GUILLEMET-FRITSCH Date: 30/03/2018	**Thesis supervisor at Universidad Autónoma de Nuevo León** Name, signature M. Juan Antonio AGUILAR GARIB Date: 20.03.2018
Head of the Doctoral School in Material Sciences, ED SdM n°482) ....Eric....BENOIST............... Name, Signature Date: 30.03.2018	**Head of the Doctoral School (or equivalent) Faculty of Physics and Mathematics Sciences** Name, Signature M. Rogelio J. SEPÚLVEDA GUERRERO Date:
Doctoral student	
Name, Signature Mme. Ana María HERNÁNDEZ LÓPEZ Date: 20.03.2018	

Contents

Contents

Figure Index

Table Index

Introduction

General Introduction

Nowadays, the electronic devices are part of our lives; computers, telephones, electrical appliances are some examples. Currently the presence of electronic components is increasing more and more in industries such as the automobile and aeronautics, as well as in in the devices or processes that require automation. One of the principal components of these devices is the capacitor, which main function is the energy storage. There are multiple types of capacitors, one of the most used are the multilayer ceramic capacitors (MLCCs). The MLCCs offer essential advantages due to their low cost, one of the reasons of its predominance in the electronics market. According to the application there are different kinds of MLCCs to choose, regarding principally the capacitance they offer but also the dielectric material and its performance under different conditions, such as the temperature. The characteristics of the MLCCs are going to be determined by extrinsic and intrinsic parameters; i.e., the nature, characteristics, synthesis and treatment of the dielectric material and the production process of the capacitors. These factors can influence on the final reliability of the capacitors and hence of the devices. For this reason, it is highly important to develop ceramic materials suitable for the different markets. One of the principal strategies to obtain reliable capacitors is to focus in the tailoring of the dielectric ceramic by modifying the material composition.

Barium titanate ($BaTiO_3$) has been the most used material as the base for the dielectric of the MLCCs due to properties such as its large permittivity. To enhance its electrical properties, it needs to be modified through the inclusion of several additives and dopants in the base formulation for the dielectric. The perovskite structure of the $BaTiO_3$ has the ability to host these dopants, which according to different conditions will occupy the A or B sites in the lattice. The occupation of the dopants within the cell structure will determine the initial electrical properties, and it is assumed

that it will also determine the reliability (lifetime) of the final product. The formulation of barium titanate powders includes as dopants rare-earth elements (REE). Among them, the Y_2O_3 is the most common for the fabrication of multilayer ceramic capacitors with base-metal electrodes (BME-MLCCs) because it has a lower cost than Ho_2O_3, Er_2O_3 and Dy_2O_3 and provides similar properties. Also, cations such as Mn^{2+}, Mg^{2+} and Ca^{2+}, that can contribute to the global distribution of the electronic defects generated when the doping ions are introduced into the lattice and during the capacitors fabrication process. In addition to these dopants, additives are added aiming to modify the production conditions, like the SiO_2 used to lower sintering temperatures. The final properties will result from the interactions that barium titanate, dopants and additives can have among each other under the specific sintering conditions. The complexity of the system is increased when given some conditions, secondary phases are formed. In previous works, these secondary phases, particularly those related to Y_2O_3 doping, are believed to be responsible for the long-term failure mechanisms of MLCC's under nominal operation.

This thesis work has the objective to analyze the role of Y_2O_3 as $BaTiO_3$ dopant and its possible contribution to the formation of secondary phases. The achievement of this objective involves two experimental blocks. First, the electrical characterization of MLCCs with Y_2O_3-doped $BaTiO_3$ as dielectric by the performance of high accelerated life tests (HALT) that lead to obtain life indicators. Secondly, the development of a doping study that includes the preparation of powders and ceramics under different sintering conditions using Y_2O_3 as dopant and two kinds of $BaTiO_3$ powders (one pure and two formulated for industrial applications).

This thesis manuscript is divided in four chapters.

The first chapter is a bibliographic introduction in order to situate this work in the current context. It presents the general properties of the $BaTiO_3$, and how they can be enhanced by the use of dopants such as the Y_2O_3 in formulations that are used for its application as the dielectric material of multilayer ceramic capacitors.

The Chapter 2 describes the different experimental methods as well as the characterization techniques used in this work.

In the Chapter 3 is presented the electrical characterization of multilayer ceramic capacitors (MLCCs) using accelerated life tests (HALT) to determine the mean time to failure (MTTF) of each group of samples and perform Weibull statistical analyses that can be used in conjunction with the Arrhenius model to obtain the activation energy (E_a) value related to the failure of the capacitors under determined conditions.

 In the Chapter 4 is presented the Y_2O_3-doping of two types of $BaTiO_3$ powders (one reagent grade and the other two commercially formulated) and the preparation of ceramics issued from those powders under different sintering conditions. The influence of the dopant and the presence of secondary phases over the structural and microstructural $BaTiO_3$ properties is described in this chapter.

CHAPTER 1

Chapter 1

Introduction

Barium titanate (BaTiO₃) has attracted the attention for decades both, in the fundamental research field as in industry for device applications. This is a noteworthy ferroelectric material because it has a high ferroelectric activity, dielectric constant and spontaneous polarization (Li, Xu, Chu, Fu, & Hao, 2009) and presents a high resistivity (10^{10}–10^{12} Ω cm) (Belous, V'yunov, Glinchuk, Laguta, & Makovez, 2008). For the above mentioned, barium titanate has a great potential for technological applications in the electronics industry. In fact, due to its high dielectric constant, low dielectric loss and superior performance at high frequency, one of its most common applications is as the dielectric material for ceramic capacitors (Wang, Chen, Gui, & Li, 2016). Among these BT-based ceramic capacitors, the multilayer ceramic capacitors (MLCCs) are widely used in military, automotive and telecommunication applications in which the devices are subjected to meaningful changes in temperature, voltages and frequencies (Wang et al, 2001). Nonetheless, when the BaTiO₃ is pure exhibits a great change in dielectric constant near the Curie temperature (Tc) which renders the ceramic material unsuitable for capacitor applications. For this reason, the capacitor BT-based formulations must be chemically modified to meet the required capacitance-temperature characteristics (X. H. Wang et al, 2001; J. Wang et al, 2016; T. Wang, 2009).

1.1. Ceramics

Ceramics are the first material that the humanity has produced by transformation of raw materials. The word is derived from Greek *keramikos*, which means *argil,* "especially potter's clay". Ceramics

own their distinctive qualities due to the composition of the raw materials as well as the way they are processed. They are divided in two types of materials: traditional and technical ceramics. The first group (alumino-silicate) is generally produced from natural raw materials (clay, feldspar, kaolin, quartz) and they are generally implemented by casting (slip). The latter (metal-metalloid associations) are obtained by sintering or by electrofusion (the oxides are poured directly into a mold) (Fantozzi, Niepce, & Bonnefont, 2013). Actually, the second group has inspired the definition of the term "ceramics", as expressed by M. Barsoum & M. W. Barsoum (2002): "solid compounds that are formed by the application of heat, and sometimes heat plus pressure, comprising at least two elements provided one of them is a non-metal or a nonmetallic element solid. The other element(s) may be a metal(s) or another nonmetallic elemental solid(s)".

This thesis work is focused on $BaTiO_3$ ceramics. These ceramics belong to the technical ceramics classification of the electronics that are semiconductors (thermistors, resistors).

1.2. BaTiO₃ – Structural characteristics

Barium titanate ($BaTiO_3$) is a ceramic material that has been widely studied due to its excellent dielectric, ferroelectric and piezoelectric properties (Nikulin, 1988; He et al., 2013). It presents a stoichiometric cubic perovskite of ABO_3-type (A = alkaline-earth element and B = transition metal) containing sties with cubic environments of oxygen while B-sites are in an octahedral environment with corner-linked octahedral, as shown in Fig. 1.1. Below the Curie temperature (Tc) the $BaTiO_3$ is non-centrosymmetric, and can present a crystal distortion (Valdez-Nava et al, 2010).

Barium titanate has five crystalline forms: hexagonal, cubic, tetragonal, orthorhombic and rhombohedral, occurring at various phase transition temperatures: 1432 °C, 130 °C, 5 °C and -90 °C, respectively. The most stable phase at room temperature is the tetragonal phase; this is the most used form because of its excellent ferroelectric, piezoelectric and thermoelectric properties (Li et al, 2009).
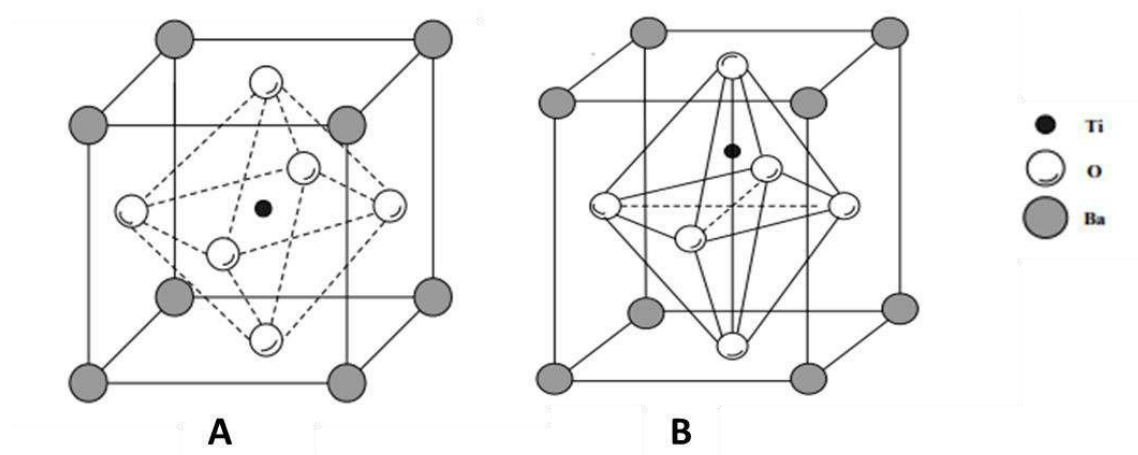
Figure 01.1. Scheme of the BaTiO$_3$ perovskite structure. A) Cubic lattice (above Curie temperature, 120°C). B) Tetragonal lattice (below Curie temperature, 120°C). (Richerson, 2005).

1.3. Role of the dopants on the electrical properties of BaTiO$_3$

The crystal structure of this oxide belongs to the perovskite type, as shown in Fig. 1.1. This structure allows it to present a high dielectric constant. Pure BT exhibits a great change in dielectric constant near Curie temperature (Tc) 120°C (X. H. Wang et al, 2001). As a ferroelectric material, BT has a temperature point known as the Curie temperature (Tc), above which it becomes substantially non-electric, i.e. dielectric (Nikulin, 1988). If the material is above Tc (and up to 1400°C) it is centrosymmetric and paraelectric. Although barium titanate presents great electrical properties, it cannot be used in its pure form as a dielectric material.

Many efforts have been done in order to enhance barium titanate electrical properties for its different applications. One of the most common and effective methods has been to design the formulation including several additives and dopants. The difference between additives and dopants is not defined with exactitude for this field of study. However, it is usually considered that the additives contribute to the improvement of the production process while the dopants are supposed to have a direct impact over the final properties of the material, i.e. the dielectric properties. In this work this is the considered differentiation.

Cations such as Mn^{2+}, Ca^{2+} and Mg^{2+} are added as dopants that can partially compensate the electrons and holes that the system might have due to the presence of oxygen vacancies (Yoon et al., 2007; Yoon, Kang, Kwon, & Hur, 2010).

Manganese can perform a double role; it can compensate the oxygen vacancies as an acceptor being incorporated at the Ti^{4+} sites, but it can act as well as an additive inhibiting an excessive grain growth. It can take different valences (Mn^{2+}, Mn^{3+} or even Mn^{4+}) during the post-sintering process, being considered as an unstable acceptor-type dopant (Paunovic, Mitic, Marjanovic, & Kocic, 2016) but helps the material to keep a high insulation resistance while accepting electrons to form a lower oxidation state (Lee, Tseng, & Hennings, 2001).

Calcium is added to contribute as well to limit the oxygen vacancies concentration which improves the reliability, and can dissolve in the BT lattice participating in the core-shell formation (Yoon et al., 2010). The mechanism by which calcium exerts these effects has been argued along decades, which is related to things like the final application of the Ca-doped BT materials and the different ways that Ca^{2+} can be added. However, it has been reported that the occupation site of Ca^{2+} is critical for it can exert the effect of increase the resistance degradation (Fang, & Shuei, 1999; Han, Appleby, & Smyth, 1987; Völtzke, Abicht, Pippel, & Woltersdorf, 2000; Zhu, Zhang, & Chen, 2013).

The introduction of dopants that can be donors or acceptors, also modify the structure of barium titanate and can contribute to the creation of chemical inhomogeneity like core-shell structure (T. Wang, X.H. Wang, Wen, & Li, 2009; Kim et al, 2008; Armstrong, & Buchanan, 1990). Magnesium has been reported as a key cation in the formation of the core-shell structure and the inhibition of grain grown since it remains at the grain boundaries while the RE ions dissolve in the BT lattice (Huang et al., 2015; Kim et al., 2008).

The core-shell structure consists of pure ferroelectric BT (tetragonal structure) in a core that is surrounded by a shell of BT containing dopants and additives (mixture of tetragonal and cubic phases) with paraelectric behavior, as shown in the Fig. 1.2. (Kim et al, 2008). Hennings and Rosenstein (1984) reported the formation mechanism of this structure. They were able to show that the cores are the same phases as the shells, since the paraelectric shells grew epitaxially on the ferroelectric cores. Considering the core-shell structures are not thermodynamically stable, its formation will be affected both by the sintering temperature and the donor-acceptor ratio (T. Wang et al, 2009).
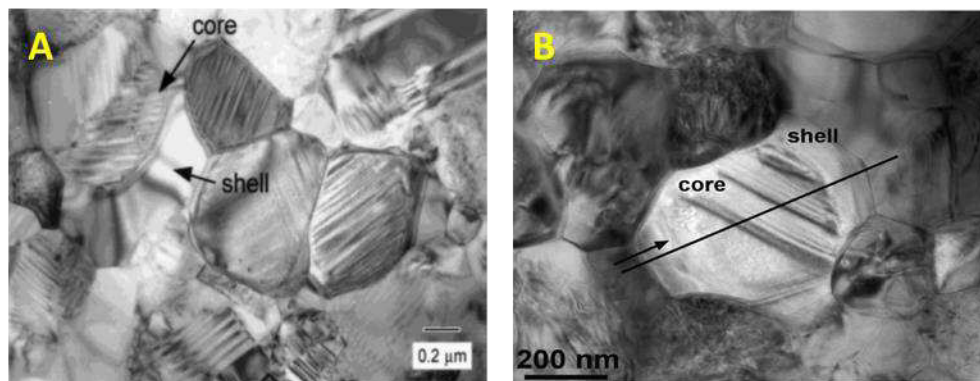
Figure 1.2. Transmission electron micrographs of core-shell structures in doped BT ceramics. (A) TEM bright field image of a X7R-type BaTiO$_3$ ceramics by Grogger, Hofer, Warbichler, Feltz, & Ottlinger, (1998). (B) TEM of a typical core-shell grain in a BT specimen doped with yttrium and magnesium by Kim et al., (2008).

The microstructure of the ceramics resulting from the elaboration process will have an influence on the dielectric properties. For instance, the milling process can cause defects on the particles' surface and activate the diffusion of the additives into the grains. It has been reported that as the milling time increases, the shell region gets thicker and the core region gets smaller, leading to a high chemical homogeneity at the core-shell interface increases (Wang et al., 2009).

The formulation of barium titanate for its use in ceramic capacitors also includes sintering aids like SiO$_2$. It is one of the most common because it has been reported to participate in the formation of a liquid phase that helps to reduce the sintering temperature and to a more uniform dispersion of the

dopants. SiO_2 has the ability to form a liquid phase from the ternary system $BaO\text{-}TiO_2\text{-}SiO_2$, diminishing the eutectic point from 1320°C to near 1260°C (Felgner, Müller, Langhammer, & Abicht, 2001; Liu & Roseman, 1999; Ösküz, Torman, S. Sen, & U. Sen, 2016). This ternary eutectic point is well known and corresponds to the $BaTiO_3 - Ba_6Ti_{17}O_{40}$ system at approximately 1330 °C (Felgner et al., 2001). When SiO_2 is present, this temperature decreases to about 1280 °C - 1260 °C. This is the reason why SiO_2 is considered as a suitable additive to produce ceramics with high density while lowering the sintering temperature, and it may even induce an improvement in the dielectric properties of BT (Öskus et al., 2016; Wu et al., 2007). Cheng (1989) also reported that the presence of SiO_2 and TiO_2, leaded to the formation of a liquid-phase former that enhanced the ionic diffusion, resulting in a uniform microstructure. This liquid phase also purified the grain interior, increasing the grain conductivity. He also evidenced that the SiO_2 and TiO_2 are located at the grain boundaries influencing only the microstructure, not the electrical properties. The liquid phase has been evidenced in studies such as the one conducted by Wu et al., (2007) through TEM analyses as shown in Fig. 1.3.
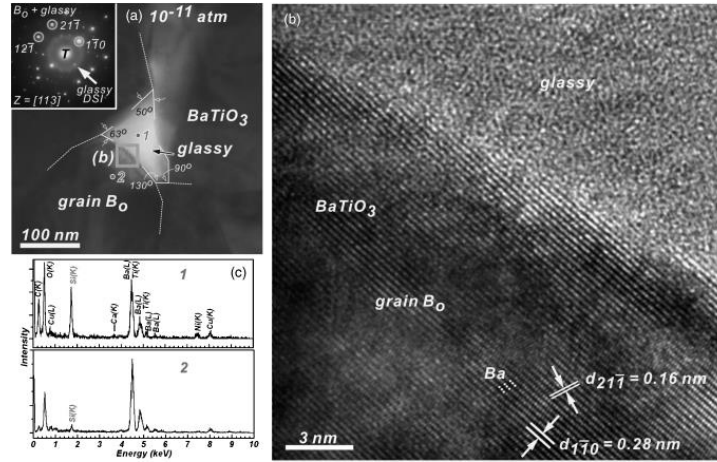
Figure 1.3. (a) Glassy second phase at triple-grain junction with selected area diffraction patterns of BaTiO₃ grain inset (BF image), (b) high-resolution image of BaTiO₃-glass interface showing an amorphous nature, and (c) energy-dispersive X-ray spectroscopy spectra for triple junction and BaTiO₃ grain (Bo) (TEM) (Wu et al., 2007).

Despite the advantages of using sintering additives, the interactions that can take place among them and the BT matrix, can turn the structural and electrical nature modifications of the doped material into undesired ways. Chemical defects and even secondary phases, such as $Ba_2TiSi_2O_8$ and $Ca_2Y_8Si_6O_{26}$ have been reported in formulated BT-based X7R MLCCs (Wu et al., 2007). Those phases could lead to the deterioration of the electrical properties that are supposed to be enhanced by the additives and dopants presence (Liu & Roseman, 1999; Öskus et al., 2016). Yan et al. (2016) reported that when adding to $BaTiO_3$ 0.5 wt% of SiO_2, no second phase was detected and it showed homogeneous microstructure with small grains. However, with further increase of SiO_2 addition to 1 and 2 wt%, $Ba_2TiSi_2O_8$ secondary phase was detected and the dielectric constant of those ceramics at the *Tc* decreased gradually.

Finally, rare-earth oxides are added as well as dopants and they can interact, due to their donor or acceptor ionic behavior, creating chemical defects and activating compensation mechanisms. The doping of BT with rare-earth ions (e.g. Y^{3+}, Dy^{3+}, Ho^{3+}) improves its dielectric performance. For this reason, the researches in materials science and electronics engineering to improve the dielectric properties of the $BaTiO_3$ as a dielectric base material and modify it directing the objectives towards the market necessities, has highly increase the last decades. Gong, Wang, Zhang, & Li (2016) reported an increase of the reliability of co-doped $BaTiO_3$-based MLCCs when using Ho^{3+} and Dy^{3+}. These dopants present a synergistic effect exhibiting a better insulation degradation behavior compared with the doped samples containing just one of the two. Similar results have been reported for donor- and acceptor-cosubstituted BT, which have shown a better insulation resistance and life stability. The most common of these systems is $BaTiO_3$-MgO-R_2O_3, with R = La^{3+}, Gd^{3+}, Dy^{3+}, Ho^{3+}, Er^{3+}, Y^{3+}, Yb^{3+} (Kuo, Wang & Tsai, 2006). The doping behaviors of R = Ho^{3+}, Dy^{3+} and Y^{3+} have been reported by authors like Makovek, Samardžija, & Drofenik, (2004). They observed that these ions have similar solubility in $BaTiO_3$ lattice and their incorporation into it is mainly dependent of the starting composition of the powders. The Ba- or Ti-richness of the powder affects

the measure in which the RE ions are going to be incorporated in each site. Park et al, (2009) compared the doping behaviors of these RE ions in $BaTiO_3$-MgO-R_2O_3 systems, obtaining the densest ceramics with the Dy^{3+} ions, which exhibited the better shell formation as well due to a higher solubility compared to the Y^{3+} and Ho^{3+} ions. However, Y- and Ho-doped ceramics showed a most stable microstructure at high temperature. The similarities in the doping behavior of these particular three ions can be due to its similar ionic radius. Some of the BT dopants with their respective ionic radii according the coordination site they can occupy are shown in the Table 1.1. The ionic radius determines the occupation site in the BT lattice of the RE dopants. Larger RE ions such as La^{3+} and Sm^{3+} are predominantly donor dopants, occupying the A-site. Smaller ions like the Yb^{3+} are acceptor dopants; they occupy the B-site. The ions with intermediate ionic size (Dy^{3+}, Ho^{3+}, Er^{3+}, Y^{3+}) can be placed both in A- and B-sites, presenting both donor and acceptor dopant behavior (Kuo et al, 2006; Park et al, 2009; Tsur, Hitomi, Scrymgeour, & Randall, 2001a).

Table 1.1. Effective ionic radii of various elements (Park et al, 2009; Tsur et al, 2001a).

Ion	Ionic radius (Å)	
	B-site (6 coordination)	A-site (12 coordination)
Ba^{2+}		1.610
Ti^{4+}	0.605	
Mg^{2+}	0.720	
Dy^{3+}	0.912	1.255
Ho^{3+}	0.901	1.234
Y^{3+}	0.900	1.234

One of the most common observations with the RE-doped BT systems is the change of the crystalline structure due to the insertion of RE ions into the BT lattice, either in A- or B-sites. The presence of dopants can lead to a transformation from a well-defined tetragonal phase to a mixture of tetragonal phases or even a new structural phase. In the literature this change of phase is usually described as a mixture of tetragonal and cubic phases and denominated as a "pseudo-cubic" phase. As previously mentioned, the additives and sintering conditions affect the microstructure as well. For instance, the diffusion of oxygen atoms through the grain boundaries into the grains, to annihilate oxygen vacancies, can be faster during the cooling step. As a result, barium vacancies remain at the grain boundaries and form high-resistance regions. This increases the ceramics resistivity (Cheng, 1989). Besides the dielectric properties, the ferroelectric characteristics can also be modified. Shifts in transition temperatures or the broadening of the ε-T curve (diffuseness of the ferroelectric transition) can be some of the effects of dopants. Depending on the nature of the incorporated dopant in the BT lattice, it can go from classical ferroelectric to diffuse ferroelectric or even relaxor (Petrović, Bobić, Ramoška, Banys, & Stojanović, 2011). Also, the electrical behavior can be altered by the dopant concentration, which can lead to a dielectric or semi-conductivity behavior (Urek, Drofenik, & Makovec, 2000).

Two of the most principal applications for barium titanate are the positive temperature coefficient resistors (PTCRs) and the multilayer ceramic capacitors (MLCCs). The formulation for both of them is tailored with the incorporation RE cations to control conductivity and electrical degradation, respectively (Tsur, Dunbar & Randall, 2001b). The trivalent RE cations are of particular interest thanks to its amphoteric behavior. These substitutions cause a charge imbalance in the system that can be compensated either ionically under oxidizing conditions or electronically under reducing conditions (Fu, Mi, Wessel, & Tietz 2008; Makovek et al., 2004). Compensation mechanisms have been proposed (J. Zhi, Chen, Y. Zhi, Vilarinho, & Baptista, 1999; Jeong, Lee, & Han, 2005;

Paredes-Olguín, Lira-Hernández, Gómez-Yañez, & Espino-Cortés, 2013) as illustrated below using the Kröger-Vink notation, when the dopant is Y_2O_3:

- When Ba^{2+} is substituted:

$$Y_2O_3 \ (in \ BaTiO_3) \rightarrow 2Y_{Ba}^{\cdot} + 2e' \qquad (1)$$

$$3Y_2O_3 \ (in \ BaTiO_3) \rightarrow 6Y_{Ba}^{\cdot} + V_{Ti}^{''''} + V_{Ba}^{''} \qquad (2)$$

- When Ti^{4+} is substituted:

$$Y_2O_3 \ (in \ BaTiO_3) \rightarrow 2Y_{Ti}' + 2h^{\cdot} \qquad (3)$$

$$Y_2O_3 \ (in \ BaTiO_3) \rightarrow 2Y_{Ti}' + V_O^{\cdot\cdot} \qquad (4)$$
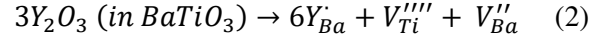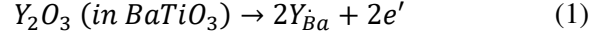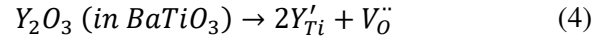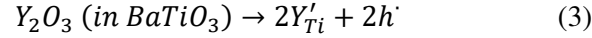
All mechanisms (1) to (4) might be active at the same time. However, the sintering parameters (temperature and P_{O_2}) will lead to the predominance of one of them. The dominant mechanism will determine the electrical properties of the doped sample, such as its resistivity. A decrease in the resistivity can be due to the presence of charge carriers, as in mechanisms (1) and (3). If (1) is the prevailing mechanism, ceramic will behave as an *n*-type semiconductor. Mechanism (3) will lead to a *p*-type behavior. On the other hand, if mechanism (4) is leading, the ceramic can be an oxygen conductor. On the basis of thermodynamic analyses, the mechanisms (3) and (4) are more probable to occur (Zhi et al., 1999; Paredes-Olguín et al., 2013). However, in Y-doping cases, it has been observed that if the concentration is less than 1 %, mechanism (1) is prevalent (Paredes-Olguín et al., 2013). The behavior as donor or acceptor of these RE cations will be also affected by the A/B ratio. An excess of BaO or TiO_2 will influence the probability of A- or B-site occupation. In the presence of an BaO excess, Y^{3+} acts as an acceptor, while it behaves like a donor if there is an TiO_2 excess (Makovek et al., 2004). Y_2O_3 is a common BT-dopant and the most suitable rare-earth oxide

for the MLCCs production because it offers the electrical properties enhancement advantages as the Ho$_2$O$_3$, Er$_2$O$_3$ and Dy$_2$O$_3$ at lower costs (Zhang et al., 2016).

Known as the "magic ions", Dy^{3+}, Ho^{3+} and Y^{3+}, are categorized as helpful for the lifetime of the MLCCs (Tsur et al., 2001a,b) for this reason, the amphoteric RE cations have been the most used for this type of applications. Since the optimization of industrial processes is crucial it is a determining factor as well at the moment to set the sintering parameters. Indeed, low sintering temperatures are preferred by industries for economic reasons.

In this work the Y$_2$O$_3$ was chosen as dopant because of its wide use in the dielectric formulations for ceramic capacitors. The thermodynamic and kinetic factors that might influence its occupation site as well as the electrical properties of the ceramics will be discussed below.

1.4. Role of Y$_2$O$_3$

The formulation of BaTiO$_3$ (BT) materials, used in the manufacturing of the MLCCs, must be tailored to control the electrical properties, especially at high temperature and under high electric field (Ashburn & Skamser, 2008; Yoon, Park, Hong & Sinn, 2007). For this purpose, several additives and dopants are added to BaTiO$_3$. One of the most used dopants is the Y$_2$O$_3$, which is added with the aim to generate compensation mechanisms that contribute to improving the reliability of the capacitors.

The Y$_2$O$_3$ has an ionic radius of 0.107 nm, it is intermediate between that of the Ba^{2+} ion (0.161 nm) and the Ti^{4+} ion (0.06 nm). Therefore Y^{3+} can occupy either Ba^{2+} or Ti^{4+} cation site in the BT lattice (Wang et al., 2014; Tsur et al., 2001a). This allows Y^{3+} to behave as acceptor or donor according to the position in the lattice. The inclusion of the Y^{3+} ion in the BT structure depends on kinetic and thermodynamic factors (Makovec et al., 2004). It is reported that the formation energy of $Y_{Ba}^{\cdot} + V_{Ba}''$ is 7.23 eV whereas it is only 4.35 eV to form a $Y_{Ba}^{\cdot} + V_{Ti}''''$ defect (Belous, V'yunov,

Kovalenko, & Makovec, 2005). The partial pressure of oxygen and sintering temperature will also induce the formation of Ba^{2+} or Ti^{4+} vacancies, leading Y^{3+} to occupy either both or one of the sites (Belous et al., 2005; Paredes-Olguín et al., 2013). This will be influenced also by the Ba/Ti ratio, the dopant concentration and its solubility. Yttrium cations have different solubility in Ba- and in Ti-sites. Zhi et al., (1999) indicated a solubility of Y^{3+} at the Ba-site of about 1.5 at% when sintered in air at 1440 – 1470°C, while it reaches 4 at% when sintered under reducing conditions (V'yunov, Kovalenko, Belous, & Belyakov, 2005). For the Ti-sites instead, the solubility is higher, approximately 12.2 at% at 1515°C when sintering in air. Wang et al. (2014) reported that the introduction of Y^{3+} in the BT lattice, can lead to structural changes, as the phase transformation from tetragonal to cubic.

The amount of yttrium ions can be spent in different processes occurring in the system during the processing of the ceramic materials. Belous et al. (2008) studied yttrium-doped BT, identifying in which processes is expended the dopant. It is known that the raw materials may contain impurities. In this case paramagnetic impurities were identified as able to occupy Ti-sites. Thus, some part of the Y^{3+} can participate in an exchange of them. Yttrium also influences the charge compensation mechanisms. And as a collateral effect, it has been found it can participate in the formation of precipitates such as $Ba_6Ti_{17}O_{40}$ and $Y_2Ti_2O_7$. These secondary phases have been usually found when the solid solubility of the dopant in the BT is surpassed.

With the appropriate amount of dopants, the structural, optical and electrical properties of a BT-doped system can be improved (Hernández Lara et al., 2017). On the other hand, there are numerous reports where the formation of secondary phases has been observed when doping BT with rare-earth elements (REE) (Belous et al., 2008; Yoon et al., 2007; Zhang et al., 2016). The formation of these precipitates depends on different factors, i.e. the sintering conditions and the dopant concentration (M. T. Buscaglia, Viviani, M. Buscaglia, Bottino, & Nanni, 2002). These secondary phases are usually formed when the amount of dopant is above of its solubility limit in

the BT-lattice. This excess of dopant can lead to its interaction with other free ions present in the system, like Ti^{4+}. Then, if the conditions are appropriate, a precipitate will be formed. Some of the secondary phases that have been observed are $Ba_2TiSi_2O_8$ (Wu, Wang, McCauley, Chu, & Lu, 2007), $Ba_6Ti_{17}O_{40}$ (Belous et al., 2008), Y_2TiO_5 (Yoon et al., 2007), and one of the most common when doping with RE oxides (Dy_2O_3, Er_2O_3, Y_2O_3 and Ho_2O_3), is the pyrochlore-type phase, $R_2Ti_2O_7$ (Jeong et al., 2005). Among the pyrochlores, $Er_2Ti_2O_7$ (Buscaglia et al., 2002), $Gd_2Ti_2O_7$ (Hernández Lara et al., 2017), $Ho_2Ti_2O_7$ (Makovec et al., 2004) and $Y_2Ti_2O_7$ (Yoon et al., 2007; Zhang et al., 2016) have been reported. $Y_2Ti_2O_7$ is suspected to be detrimental to the reliability of BT-based MLCCs (Yoon et al., 2007; Zhang et al., 2016).

The effect of the presence of these secondary phases over the $BaTiO_3$ structural and dielectric properties is of high interest for industrial applications. Several authors have reported a detrimental effect of $Y_2Ti_2O_7$ on BT dielectric performance (Wu et al., 2007; Yoon et al., 2007; Zhang et al., 2016). The yttrium pyrochlore ($Y_2Ti_2O_7$) has a highly conductive nature and is suspected to be related with the resistance degradation of the material through the acceleration of oxygen vacancies electromigration (Zhang et al., 2016). The investigation of the formation parameters and possible effects of this phase is of high interest in the academic and industrial field since Y_2O_3 is a one of the most frequent dopants used in the MLCCs production.

1.5. Sintering atmosphere influence over dopant occupancy in BT-doped ceramics

One of the most important parameters to obtain a BT material with the appropriate properties for its application as ceramic dielectric is the oxygen partial pressure (P_{O_2}) during sintering treatment. P_{O_2} affects the incorporation of dopants into the BT-lattice (Buscaglia et al., 2002; Tsur et al., 2001b). The site occupancy of dopants in BT-lattice is restrained by the valence of the ion, its size, the A/B ratio (i.e. the activity of Ti in the system) and by the oxygen vacancies concentration. It has

been observed that the P_{O_2} influences the charge compensation mechanisms (ionically or electronically) dictating a change in the A/B ratio in the perovskite lattice, which can lead to the formation of precipitates. Furthermore, the changes induced by the P_{O_2} significantly affects the electrical behavior (Fu et al., 2008).

Either a reducing or an oxidizing sintering atmosphere can be used for the production of BT-doped ceramics. However, taking into account the cost reduction at industry level due to the use of nickel for the inner electrodes instead of the expensive noble metals previously employed, (palladium or silver palladium alloys), one of the factors that forces the use of reducing atmospheres is to protect Ni-electrodes from oxidation. Thus, the process must to be carried out in reducing atmospheres, such as CO/CO_2 or N_2/H_2, being the latter the most used (Albertsen, Hennings, & Steigelmann, 1998; Hagenbeck & Waser, 1998; Okino et al., 1994). Meanwhile, in the research field, either reducing or oxidizing atmospheres have been utilized.

The control of P_{O_2} employed during the sintering of BT-doped ceramics can even contribute to the formation of Ti^{3+} ions, assuming the substitution of Y^{3+} for Ba^{2+} in the BT-lattice. Tien & Carlson (1963) performed some experiments to determine the relation between the degree of oxidation and the resistivity-temperature characteristics of Y-doped polycrystalline BT. They found that the oxygen partial pressure increases the slope of temperature-resistivity curves above Tc and the resistivity at room temperature. This behavior is related to the amount of Ti^{3+} present in the system. Under equilibrium conditions, the relation between P_{O_2} and Ti^{3+} concentration is described by: $2Ti^{4+} + O^{2-} \rightleftharpoons 2Ti^{3+} + \frac{1}{2} O_2$. Previous reaction is overlapped by the Y^{3+} dopant, its level and the prevailing equilibrium conditions will then determine the concentration of Ti^{3+}. Following the expression for the equilibrium constant $\left(K = \frac{(Ti^{3+})^2 P_{O_2}^{1/2}}{(Ti^{4+})^2 (O^{2-})} \right)$, [$Ti^{3+}$] is constant at a given temperature and equilibrium conditions as determined by dopant amount and the prevailing P_{O_2}. If the P_{O_2} is constant as the temperature is decreasing, then the equilibrium constant will be decreasing which as

well will dictate an increase of Ti^{3+} concentration, and this will influence the electrical behavior of the material (Tien & Carlson, 1963).

Tsur et al. (2001a, 2001b) investigated the site occupancy of rare earth ions in the BT-lattice according to the atmosphere conditions. They found that when BT is fired at low P_{O_2} and high temperatures, dopants such as Er, Y, Ho and Dy are amphoteric (Tsur et al., 2001a). They also observed that samples fired in air present larger cell volumes than the ones sintered in reduced atmospheres. The latter is due to the lower presence of oxygen vacancies in air sintered samples, thus site occupancy is directed towards more B-site occupancy (Tsur et al., 2001b).

1.6. Multilayer ceramic capacitors (MLCCs)

In the past decades, the electronic devices design has gone toward the miniaturization and reduction of power consumption. This trend requires high reliability for the electronic components (Shimada, Utsumi, Yonezawa, & Takamizawa, 1981). Among the most important electronic items are the Multilayer Ceramic Capacitors (MLCCs) (Fig. 1.4). MLCCs were developed in the 1960s and its use increased in the 1980s (Pan & Randall, 2010). These pieces are used in strongly growing markets (Acosta, Zang, Jo & Rödel, 2012), making up approximately 30% of the total components in a typical hybrid circuit module (Futureelectronics.com. (n.d.)). They present an economical volumetric efficiency for capacitance and high reliability. MLCCs are characterized by a high dielectric constant (K) and thinner dielectric layers (Jain, Fung, Hsiao, & Chan, 2010). MLCCs can be broadly divided, depending on the application, into two types: for temperature compensation and for high-dielectric constant. MLCCs for high-dielectric constant use barium titanate as the dielectric component. Among this type of capacitors, the X7R is the most stable, covering a broad spectrum of applications. X7R formulations are called "temperature stable" ceramics, which allows apply them widely in miniaturization of electronic components (Li, Zhang, Zhou, Chen, & Wang, 2007).
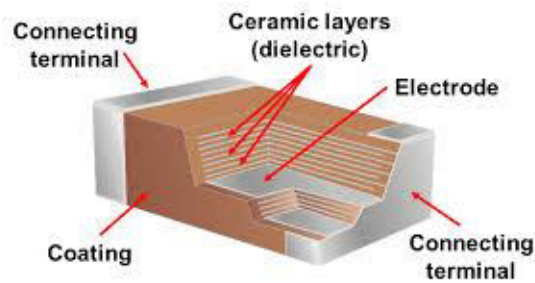
Figure 1.4. Basic structure of a multilayer ceramic capacitor.

Multilayer ceramic capacitors are classified in three classes according the Electronic Industry Alliance (EIA). Class I are Temperature Compensating capacitors, they are known as COG (a.k.a. NPO). Class II is known as Stable capacitors, the most common among them are X7R, X5R and Y5V. Finally, class III: Z5U, known as the General Purpose capacitors (Ashburn, & Skamser, 2008; Pan & Randall, 2010; Standard, E.I.A., 2002). The specifications of classes I and II are shown in Table 1.2. They can be classified by its rated voltage, tolerance, type of dielectric, capacitance, packaging type and case size. The most common values for capacitance are 10 nF, 100 nF and 1 μF. The rated voltage (RV) can be between 4 V and 10 kV, and the most common capacitors have a RV of 16, 25, 50 or 100 V (Futureelectronics.com. (n.d.)). The EIA specification for X7R MLCCs is a temperature variation of capacitance ($\Delta C/C$) within ± 15 % from -55 °C to 125 °C. (Li et al., 2007; Park et al., 2009).

Multilayer ceramic capacitors of Classes II and III exhibit aging characteristics. The capacitance of Class II devices typically falls 10 % with applied voltages of 50 to 70 % of the device's maximum working voltage. Class III devices lose capacitance starting at 10 % of the maximum working voltage and exhibit as little as 30% of their nameplate value at 90 % of their voltage range (Pan & Randall, 2010).

Table 1.2. Types of MLCCs and specifications ([Kahn, 1981; Kishi Mizuno, & Chazono, 2003]).

EIA Designation	Class	Temperature range (°C)	$\Delta C/C$ (%)	K value up to	BT content (%)	Other dopants	Grain size (µm)
C0G (NPO)	I	-55 to 125	± 30	100	10-50	TiO_2, $CaTiO_3$, $Nd_2Ti_2O_7$	1
X7R	II	-55 to 125	± 15	4000	90-98	MgO, MnO, Nb_2O_5, CoO, Rare-earth elements	< 1.5
Z5U	II	10 to 85	+ 22, -56	14000	80-90	$CaZrO_3$, $BaZrO_3$	3-10
Y5V	II	-30 to 85	+22, -82	18000	80-90	$CaZrO_3$, $BaZrO_3$	3-10

The capacitor technology has changed according to the industrial and commercial demands. Since many of MLCCs applications are manipulated at extreme operational conditions, like high temperatures (beyond 200 °C), the capacitors must be processed out under high degree requirements to ensure a high-yield, large-scale, low-cost production process ([Kahn, 1981]). MLCCs with X7R-formulation based on $BaTiO_3$ dielectric material, are usually produced under a sintering process with a temperature between 1200 °C and 1300 °C and low P_{O_2} of about 10^{-9} – 10^{-11} atm. This is followed by a re-oxidation step at 800° - 1000°C in P_{O_2} between 10^{-6} – 10^{-8} atm. ([Wu et al., 2007]). This last step contributes as well to the attempt to diminish the contribution of oxygen vacancies ([Pan & Randall, 2010]). A whole general view of the industrial production process of these capacitors is shown in the Fig. 1.5.
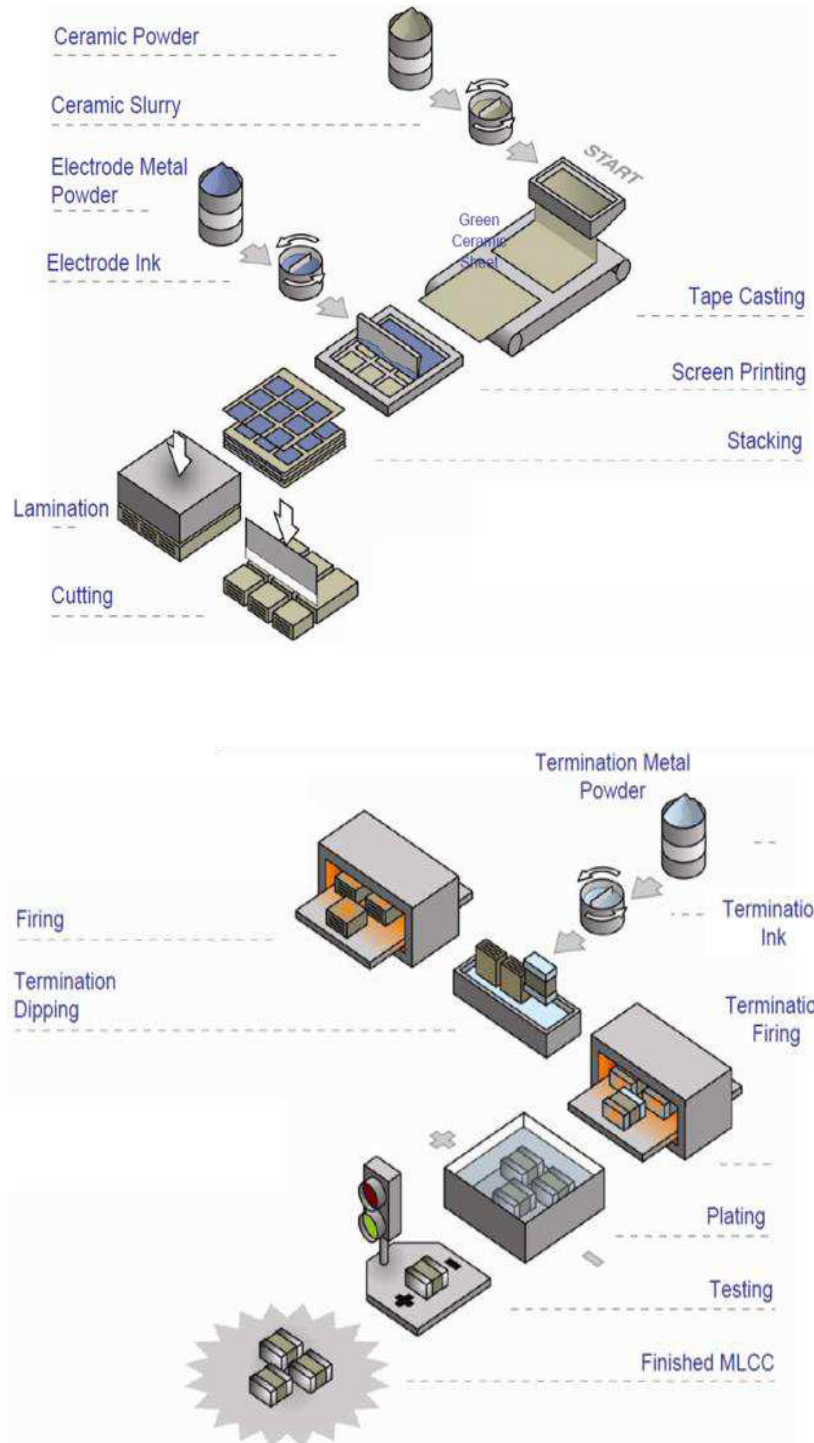
Figure 1.5. *MLCCs production process. Adapted from Basics of Ceramic Chip Capacitors by Johanson Dielectrics. 2008.*

The characteristics of each MLCC type challenge a highest quality for its production. Each step during this process must be carefully supervised, taking care of some key factors that will critically

influence the lifetime and resistance degradation of the capacitors. Some of the considerations to take into account, as it has been explained, are the characteristics of the starting BT powder and the features of the final formulation to be applied, i.e. optimization of additives and dopants. There are as well some aspects related particularly to the process, as the coating of the dielectric material and the control of atmospheric conditions during thermal processing. As long as the production steps are under control, the process will be robust ensuring a high-quality product (Ashburn & Skamser, 2008).

Nevertheless, even though research in the last decades has allowed to the industries the optimization of the production process, exhibiting a great improvement in the technology of the electronic field, some failures are still observed in some cases.

Two failure modes have been identified in Base-Metal-Electrode (BME) Multilayer Ceramic Capacitors (MLCCs): catastrophic and slow degradation. Catastrophic failures are mainly due to present processing defects (extrinsic defects), such as voids, cracks and delaminations. These are characterized by a time-accelerating increase in leakage current. On the other hand, the slow degradation failures are related with the electromigration of oxygen vacancies, which are considered intrinsic defects, and are characterized by a near-linear increase in leakage current against stress time (Liu, 2015).

These failure modes can be distinguished using a 2-parameter Weibull plot. The early (catastrophic) failures can be distinguished by a slope parameter of $\beta > 1$. This β value indicates that these are not infant mortalities (Liu & Sampson, 2012).

Early failures have been related to the decrease of the dielectric thickness, being triggered by external electrical overstress. This has represented a problem to control a high reliability with the miniaturization of MLCCs. The breakdown leakage current that characterize an early failure is an avalanche-like type (Liu & Sampson, 2012). Since, as mentioned before, these failures are related to

extrinsic defects, i.e. minor construction defects introduced during fabrication of the capacitors, the production control and quality requirements are a crucial factor to obtain a reliable final product.

It has been reported that insulation resistance (IR) degradation of BT-based BME-MLCCs might be related with three probable aspects: the dielectric layer, the BT grain boundaries, and the internal electrode interfaces between $Ni\text{-}BaTiO_3$ (Liu, 2015).

References

Acosta, M., Zang, J., Jo, W., & Rödel, J. (2012). High-temperature dielectrics in $CaZrO_3$-modified $Bi_{1/2}Na_{1/2}TiO_3$-based lead-free ceramics. *Journal of the European Ceramic Society, 32*(16), 4327-4334.

Albertsen, K., Hennings, D., & Steigelmann, O. (1998). Donor-acceptor charge complex formation in barium titanate ceramics: Role of firing atmosphere. *Journal of electroceramics, 2*(3), 193-198.

Ashburn, T., & Skamser, D. (2008, January). Highly accelerated testing of capacitors for medical applications. In *Proceedings of the 5th SMTA Medical Electronics Symposium*. California, USA.

Armstrong, T. R., & Buchanan, R. C. (1990). Influence of Core-Shell Grains on the Internal Stress State and Permittivity Response of Zirconia-Modified Barium Titanate. *Journal of the American Ceramic Society, 73*(5), 1268-1273.

Barsoum, M., & Barsoum, M. W. (2002). Fundamentals of ceramics. CRC press.

Belous, A., V'yunov, O., Kovalenko, L., & Makovec, D. (2005). Redox processes in highly yttrium-doped barium titanate. *Journal of Solid State Chemistry*, 178(5), 1367-1375.

Belous, A., V'yunov, O., Glinchuk, M., Laguta, V., & Makovez, D. (2008). Redox processes at grain boundaries in barium titanate-based polycrystalline ferroelectrics semiconductors. *Journal of materials science, 43*(9), 3320-3326.

Buscaglia, M. T., Viviani, M., Buscaglia, V., Bottino, C., & Nanni, P. (2002). Incorporation of Er^{3+} into $BaTiO_3$. *Journal of the American Ceramic Society*, 85(6), 1569-1575.

Cheng, H. F. (1989). Effect of sintering aids on the electrical properties of positive temperature coefficient of resistivity BaTiO3 ceramics. *Journal of Applied Physics*, 66(3), 1382-1387.

Fang, T. T., & Shuei, J. T. (1999). Experimental assessment of the inhibition of reduction of Ca^{2+}-doped barium titanate in a reducing atmosphere. *Journal of materials research, 14*(5), 1910-1915.

Fantozzi, G., Niepce, J. C., & Bonnefont, G. (2013). *Les céramiques industrielles: Propriétés, mise en forme et applications*. Dunod.

Felgner, K. H., Müller, T., Langhammer, H. T., & Abicht, H. P. (2001). Investigations on the liquid phase in barium titanate ceramics with silica additives. *Journal of the European Ceramic Society, 21*(10), 1657-1660.

Fu, Q. X., Mi, S. B., Wessel, E., & Tietz, F. (2008). Influence of sintering conditions on microstructure and electrical conductivity of yttrium-substituted $SrTiO_3$. *Journal of the European Ceramic Society, 28*(4), 811-820.

Grogger, W., Hofer, F., Warbichler, P., Feltz, A., & Ottlinger, M. (1998). Imaging of the core–shell structure of doped $BaTiO_3$ ceramics by energy filtering TEM. *Physica status solidi (a), 166*(1), 315-325.

Gong, H., Wang, X., Zhang, S., & Li, L. (2016). Synergistic effect of rare-earth elements on the dielectric properties and reliability of $BaTiO_3$-based ceramics for multilayer ceramic capacitors. *Materials Research Bulletin, 73*, 233-239.

Guha, J. P. and Kolar, D., Phase equilibria, sintering characteristics and dielectric properties in the BaTiO3-rich portion of the system $BaO–TiO_2–SiO_2$. In *5th Conference on Ceramics for Electronics*, Liblice, 1974, pp. 1–9.

Hagenbeck, R., & Waser, R. (1998). Influence of temperature and interface charge on the grain-boundary conductivity in acceptor-doped $SrTiO_3$ ceramics. *Journal of applied physics, 83*(4), 2083-2092.

Han, Y. H., Appleby, J. B., & Smyth, D. M. (1987). Calcium as an acceptor impurity in $BaTiO_3$. *Journal of the American Ceramic Society, 70*(2), 96-100.

He, F., Ren, W., Liang, G., Shi, P., Wu, X., & Chen, X. (2013). Structure and dielectric properties of barium titanate thin films for capacitor applications. *Ceramics International, 39*, S481-S485.

Hennings, D., & Rosenstein, G. (1984). Temperature-Stable Dielectrics Based on Chemically Inhomogeneous $BaTiO_3$. *Journal of the American Ceramic Society, 67*(4), 249-254.

Hernández Lara, J. P., Pérez Labra, M., Barrientos Hernández, F. R., Romero Serrano, J. A., Ávila Dávila, E. O., Thangarasu, P., & Hernández Ramirez, A. (2017). Structural Evolution and Electrical Properties of $BaTiO_3$ Doped with Gd^{3+}. *Materials Research, 20*(2), 538-542.

Huang, X., Liu, H., Hao, H., Zhang, S., Sun, Y., Zhang, W., ... & Cao, M. (2015). Microstructure effect on dielectric properties of MgO-doped $BaTiO_3$–$BiYO_3$ ceramics. *Ceramics International, 41*(6), 7489-7495.

Jain, T. A., Fung, K. Z., Hsiao, S., & Chan, J. (2010). Effects of BaO–SiO_2 glass particle size on the microstructures and dielectric properties of Mn-doped Ba(Ti, Zr)O_3 ceramics. *Journal of the European Ceramic Society*, 30(6), 1469-1476.

Jeong, J., Lee, E. J., & Han, Y. H. (2005). Electrical properties of holmium-doped $BaTiO_3$. *Japanese journal of applied physics*, 44(6R), 4047.

Kahn, M. (1981). Multilayer Ceramic Capacitors-Materials and Manufacture. *AVX Technical Information Series*.

Kim, C. H., Park, K. J., Yoon, Y. J., Hong, M. H., Hong, J. O., & Hur, K. H. (2008). Role of yttrium and magnesium in the formation of core-shell structure of $BaTiO_3$ grains in MLCC. *Journal of the European Ceramic Society, 28*(6), 1213-1219.

Kishi, H., Mizuno, Y., & Chazono, H. (2003). Base-metal electrode-multilayer ceramic capacitors: past, present and future perspectives. *Japanese Journal of Applied Physics, 42*(1R), 1.

Kuo, D. H., Wang, C. H., & Tsai, W. P. (2006). Donor-and acceptor-cosubstituted $BaTiO_3$ for nonreducible multilayer ceramic capacitors. *Ceramics international, 32*(1), 1-5.

Lee, W. H., Tseng, T. Y., & Hennings, D. (2001). Effects of ceramic processing parameters on the microstructure and dielectric properties of $(Ba_{1-x}Ca_x)(Ti_{0.99-y}Zr_yMn_{0.01})O_3$ sintered in a reducing atmosphere. *Journal of Materials Science: Materials in Electronics, 12*(2), 123-130.

Li, B., Zhang, S., Zhou, X., Chen, Z., & Wang, S. (2007). Microstructures and dielectric properties of Y/Zn codoped BaTiO3 ceramics. *Journal of materials science,* 42(13), 5223-5228.

Li, W., Xu, Z., Chu, R., Fu, P., & Hao, J. (2009). Structure and electrical properties of $BaTiO_3$ prepared by sol–gel process. *Journal of Alloys and Compounds, 482*(1), 137-140.

Liu, G., & Roseman, R. D. (1999). Effect of BaO and SiO_2 addition on PTCR $BaTiO_3$ ceramics. *Journal of Materials science, 34*(18), 4439-4445.

Liu, D. D., & Sampson, M. J. (2012). Some aspects of the failure mechanisms in $BaTiO_3$-Based multilayer ceramic capacitors.

Liu, D. D. (2015). Insulation resistance degradation in Ni–$BaTiO_3$ multilayer ceramic capacitors. IEEE Transactions on Components, *Packaging and Manufacturing Technology*, 5(1), 40-48.

Luo, Y., Pu, Y., Zhang, P., Zhao, J., Wu, Y., & Liu, Y. (2016). Study on Dielectric Properties of SiO_2-doped $BaTiO_3$ Ceramics. *Ferroelectrics, 492*(1), 10-16.

Makovec, D., Samardžija, Z., & Drofenik, M. (2004). Solid solubility of holmium, yttrium, and dysprosium in $BaTiO_3$. *Journal of the American Ceramic Society, 87*(7), 1324-1329.

Futureelectronics.com. (n.d.). Multilayer ceramic capacitor, high voltage ceramic capacitors - Future Electronics. [online] Retrieved from: http://www.futureelectronics.com/en/capacitors/multilayer-ceramic-capacitor.aspx [Accessed 8 Nov. 2017].

N. Nikulin, Fundamentals of electrical materials, Mir Publishers, Moscow, (1988).

Nicker, D. A. (1974). High voltage ceramic capacitors. *Active and Passive Electronic Components, 1*(2), 113-120.

Okino, Y., Shizuno, H., Kusumi, S., & Kishi, H. (1994). Dielectric properties of rare-earth-oxide-doped BaTiO$_3$ ceramics fired in reducing atmosphere. *Japanese journal of applied physics, 33*(9S), 5393.

Ösküz, K. E., Torman, M., Sen, S., & Sen, U. (2016). Effect of sintering temperature on dielectric properties of SiO$_2$ Doped BaTiO$_3$ ceramics. *Materials, Methods & Technologies, 10*, 361-366.

Pan, M. J., & Randall, C. A. (2010). A brief introduction to ceramic capacitors. *IEEE electrical insulation magazine, 26*(3).

Paredes-Olguín, M., Lira-Hernández, I. A., Gomez-Yañez, C., & Espino-Cortes, F. P. (2013). Compensation mechanisms at high temperature in Y-doped BaTiO$_3$. *Physica B: Condensed Matter, 410*, 157-161.

Park, K. J., Kim, C. H., Yoon, Y. J., Song, S. M., Kim, Y. T., & Hur, K. H. (2009). Doping behaviors of dysprosium, yttrium and holmium in BaTiO$_3$ ceramics. *Journal of the European Ceramic Society, 29*(9), 1735-1741.

Paunovic, V., Mitic, V., Marjanovic, M., & Kocic, L. (2016). Dielectric properties of La/Mn codoped barium titanate ceramics. *Facta Universitatis, Series: Electronics and Energetics, 29*(2), 285-296.

Petrović, M. V., Bobić, J. D., Ramoška, T., Banys, J., & Stojanović, B. D. (2011). Electrical properties of lanthanum doped barium titanate ceramics. *Materials characterization, 62*(10), 1000-1006.

Richerson, D. W. (2005). Modern ceramic engineering: properties, processing, and use in design. CRC press.

Shimada, Y., Utsumi, K., Yonezawa, M., & Takamizawa, H. (1981). Properties of the large-capacitance multilayer ceramic capacitor. *Japanese Journal of Applied Physics*, 20(S4), 143.

Standard, E.I.A. (2002). Ceramic dielectric capacitors classes I, II, III and IV–part I: characteristics and requirements. EIA-198-1-F, November.

Tien, T. Y., & Carlson, W. G. (1963). Influence of oxygen partial pressure on properties of semiconducting barium titanate. *Journal of the American Ceramic Society, 46*(6), 297-298.

Tsur, Y., Hitomi, A., Scrymgeour, I., & Randall, C. A. (2001a). Site occupancy of rare-earth cations in $BaTiO_3$. *Japanese Journal of Applied Physics, 40*(1R), 255.

Tsur, Y., Dunbar, T. D., & Randall, C. A. (2001b). Crystal and defect chemistry of rare earth cations in $BaTiO_3$. *Journal of Electroceramics, 7*(1), 25-34.

Urek, S., Drofenik, M., & Makovec, D. (2000). Sintering and properties of highly donor-doped barium titanate ceramics. *Journal of materials science, 35*(4), 895-901.

Valdez-Nava, Z., Tenailleau, C., Guillemet-Fritsch, S., El Horr, N., Lebey, T., Dufour, P., ... & Chane-Ching, J. Y. (2011). Structural characterization of dense reduced $BaTiO_3$ and $Ba_{0.95}La_{0.05}TiO_3$ nanoceramics showing colossal dielectric values. *Journal of Physics and Chemistry of solids, 72*(1), 17-23.

Völtzke, D., Abicht, H. P., Pippel, E., & Woltersdorf, J. (2000). Ca-containing additives in PTC-BaTiO3 ceramics: effects on the microstructural evolution. *Journal of the European Ceramic Society, 20*(11), 1663-1669.

V'yunov, O. I., Kovalenko, L. L., Belous, A. G., & Belyakov, V. N. (2005). Oxidation of reduced Y-doped semiconducting barium titanate ceramics. *Inorganic materials*, 41(1), 87-93.

Wang, J., Rong, G., Hao, L., Gao, L., Cheng, H., Li, J., & Duan, R. (2016). Dielectric properties of $Ba_{0.97}Bi_{0.02}TiO_3$–$Ba_{1-x}Mg_xSn_{0.02}Ti_{0.98}O_3$ composite ceramics. *Modern Physics Letters B, 30*(29), 1650363.

Wang, M. J., Yang, H., Zhang, Q. L., Hu, L., Yu, D., Lin, Z. S., & Zhang, Z. S. (2014). Doping behaviors of yttrium, zinc and gallium in $BaTiO_3$ ceramics for AC capacitor application. *Journal of Materials Science: Materials in Electronics, 25*(7), 2905-2912.

Wang, T., Wang, X. H., Wen, H., & Li, L. T. (2009). Effect of milling process on the core-shell structures and dielectric properties of fine-grained $BaTiO_3$-based X7R ceramic materials. *International Journal of Minerals, Metallurgy and Materials, 16*(3), 345-348.

Wang, X. H., Chen, R., Gui, Z., & Li, L. (2001). Synthesis and properties of barium titanate based X7R ceramics by chemical method. *Ferroelectrics, 262*(1), 251-256.

Wu, Y. C., Wang, S. F., McCauley, D. E., Chu, M. S., & Lu, H. Y. (2007). Dielectric Behavior and Second Phases in X7R-Formulated $BaTiO_3$ Sintered in Low-Oxygen Partial Pressures. *Journal of the American Ceramic Society, 90*(9), 2926-2934.

Yan, Y., Liu, L., Ning, C., Yang, Y., Xia, C., Zou, Y., ... & Liu, G. (2016). Improved electrical properties of SiO_2-added $BaTiO_3$ ceramics by microwave sintering. *Materials Letters, 165*, 135-138.

Yoon, S. H., Park, Y. S., Hong, J. O., & Sinn, D. S. (2007). Effect of the pyrochlore ($Y_2Ti_2O_7$) phase on the resistance degradation in yttrium-doped $BaTiO_3$ ceramic capacitors. *Journal of Materials Research*, *22*(9), 2539-2543.

Yoon, S. H., Kang, S. H., Kwon, S. H., & Hur, K. H. (2010). Resistance degradation behavior of Ca-doped $BaTiO_3$. *Journal of Materials Research*, *25*(11), 2135-2142.

Zhang, J., Hou, Y., Zheng, M., Jia, W., Zhu, M., & Yan, H. (2016). The occupation behavior of Y_2O_3 and its effect on the microstructure and electric properties in X7R dielectrics. *Journal of the American Ceramic Society*, 99(4), 1375-1382.

Zhi, J., Chen, A., Zhi, Y., Vilarinho, P. M., & Baptista, J. L. (1999). Incorporation of yttrium in barium titanate ceramics. *Journal of the American Ceramic Society*, 82(5), 1345-1348.

Zhu, X. N., Zhang, W., & Chen, X. M. (2013). Enhanced dielectric and ferroelectric characteristics in Ca-modified $BaTiO_3$ ceramics. *Aip Advances, 3*(8), 082125.

CHAPTER 2

Chapter 2

Introduction

In this chapter we present the different analytic techniques used for the characterization of samples as well as the experimental set-up performed throughout this work. To start the characterization of multilayer ceramic capacitors will be presented and then the preparation and characterization of the Y_2O_3-doped $BaTiO_3$ powders and ceramics.

2.1. Electrical characterization of multilayer ceramic capacitors

2.1.1. Multilayer ceramic capacitors (MLCCs) samples description

Multilayer ceramic capacitors (MLCCs) of the X7R type (Fig. 2.1) were provided by KEMET de México. In this work we counted with three different groups of samples, denominated: A, B, and C. The differences of these groups of MLCCs lie in the composition of the formulated barium titanate powder used as dielectric ceramic material of each one.
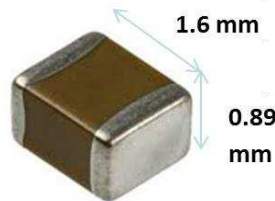
Figure 2.1. X7R MLCC

2.1.2. Electrical characterization tests

Multilayer ceramic capacitor samples were subjected to life tests to accomplish their characterization with the determination of life parameters.

2.3.2.1. High Accelerated Life Test (HALT) protocol for individual I-V measurements

To set up the right conditions to perform adequately a HALT in house, it was necessary to know the behavior of the three groups of capacitors. In this way, measurements of resistance degradation during time, under a fixed high voltage value and different temperatures to cover a broad range that could provide the information required, were performed.

The electrical measurements were performed over one sample at the time in a Signatone S-1160 probe station using a high precision (Signatone model S-1060R QuieTemp DC) hot chuck system (1 °C resolution and can operate at temperatures up to 300 °C) and a Keithley's 2410 Source Measure Unit (SMU) DC source/monitor (source voltage from 5 µV to 1100 V; measure voltage from 1 µV to 1100 V). This experimental set up is shown in Fig. 2.2.

To start, a HALT was performed under industrial standard conditions: 400 V and 140 °C for 24 h. In this work, the test was stopped when 24 h had passed without failure or at the moment the sample suffered a breakdown. Additionally, HALT were conducted under the same voltage value but using different temperatures to observe the behavior at higher and lower than 140 °C values.
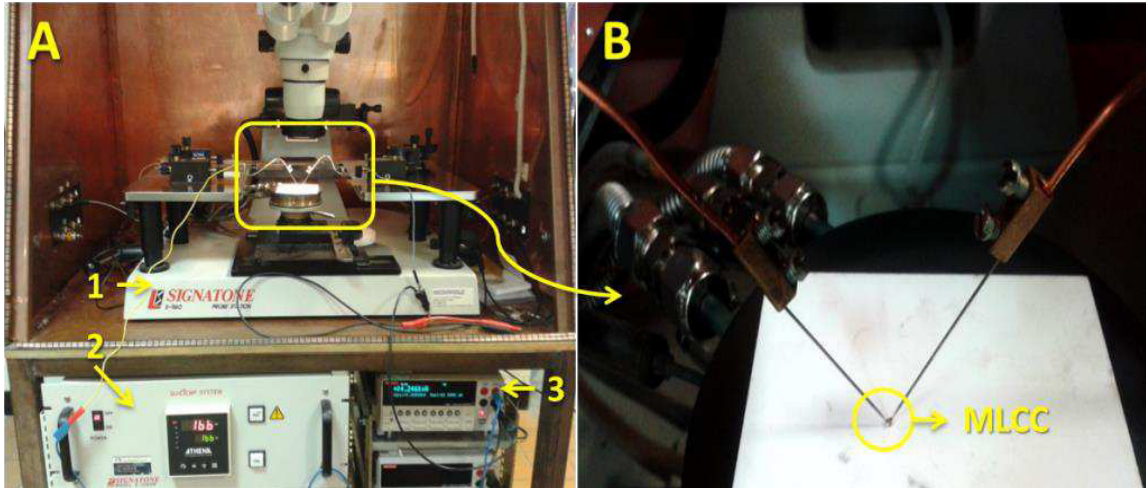
Figure 2.2. (A) *Experimental set-up: (1) S-1160 probe station, (2) Heating chuck, (3) SMU Keithley 2410.*
(B) Enlarged view of the MLCC under test.

2.3.2.2. High Accelerated Life Test (HALT) protocol

Three groups of MLCCs of the X7R type were tested under a high accelerated life test (HALT). Measurements of time-to-failure (TTF) of each group of samples were performed under a given set of stress conditions (Table 2.1). The HALT protocol combined two values of voltages and for each one a broad range of temperatures. In this way, it was possible to determine an activation energy linked to the failures for each group of stresses.

In each test, at least 12 pieces of capacitors were subjected to electrical and thermal stress; both parameters (voltage and temperature) were kept constant during the experiment. When it was observed that the ensemble or majority of samples had failed, the test was stopped and data of the evolution of the current with the time were taken to determine the time-to-failure (TTF) of the samples for each combined stress conditions.

Table 2.1. HALT parameters for the three groups of MLCCs.

MLCCs group	Voltage (V)	Range of temperature (°C)
A	400	140 – 250
	600	120 – 220
B	400	110 – 225
	600	90 – 200
C	400	20 – 90
	600	20 - 80

2.3.2.4. In-house device for HALT measurements with multiple samples

Samples were stressed by subjecting them to high values of voltage and temperature according to a HALT protocol previously described. In order to test multiple samples at the same time controlling the experimental conditions, a system was developed and built in-house. This system is shown in Fig. 2.3. It has a HV power supplier (1 kV – 10 mA) (Spellman High Voltage Electronics Corporation) (Fig. 2.3.A), which was connected in parallel with the samples (Fig. 2.3.B) that were afterwards enclosed in a metallic cell (Fig. 2.3.C) that allowed keeping uniform the temperature.
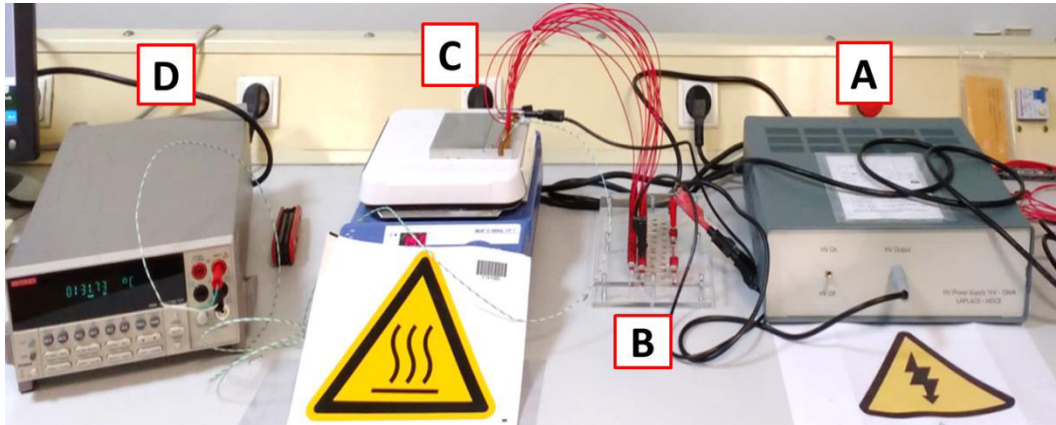
Figure 2.3. *System for perform HALT over multiple samples at once. (A) HV power supplier (1 kV – 10 mA). (B) Plate with protective resistors in parallel to connect the samples that are inside (C) a metallic cell placed over a heating plate which temperature is monitored with (D) a multimeter reading the measurements of a thermocouple (K type).*

The setting up of the samples for the tests performance included the details shown in Fig. 2.4. To preserve the system, protective resistors (MS176-5 μΩ, Caddock Electronics Inc.) were joined (Fig. 2.4.a) and having into account the resistance that they could offer, the system has a testing capacity of 20 samples; in the performed tests 12 samples were used each time. To protect samples (Fig. 2.4.b-1) from direct contact with the metallic cell, they were manually put inside a capillary glass (Fig. 2.4.b-2) together with a spring test probe (RS Pro 1.27mm Pitch Spring Test Probe with Point Tip) (Fig. 2.4.b-3) that contributed with the conduction of the current as well to keep the MLCC fixed for the sake of the measure. The cell with the samples in its interior (Fig. 2.4.c) was closed and then put over a heating plate; a closer view of the samples in the inside is shown in Fig. 2.4.d. The heating plate temperature was fixed and measured with a thermocouple (K type) that went inside a cell in the same way samples did. The used temperature was always kept below 280 °C, considering the fusion temperature (296 – 300 °C) of the solder material used to assemble the springs with the connecting cables. When the whole set-up was ready (Fig. 2.5) and the desired temperature reached, the electrical stress was applied.
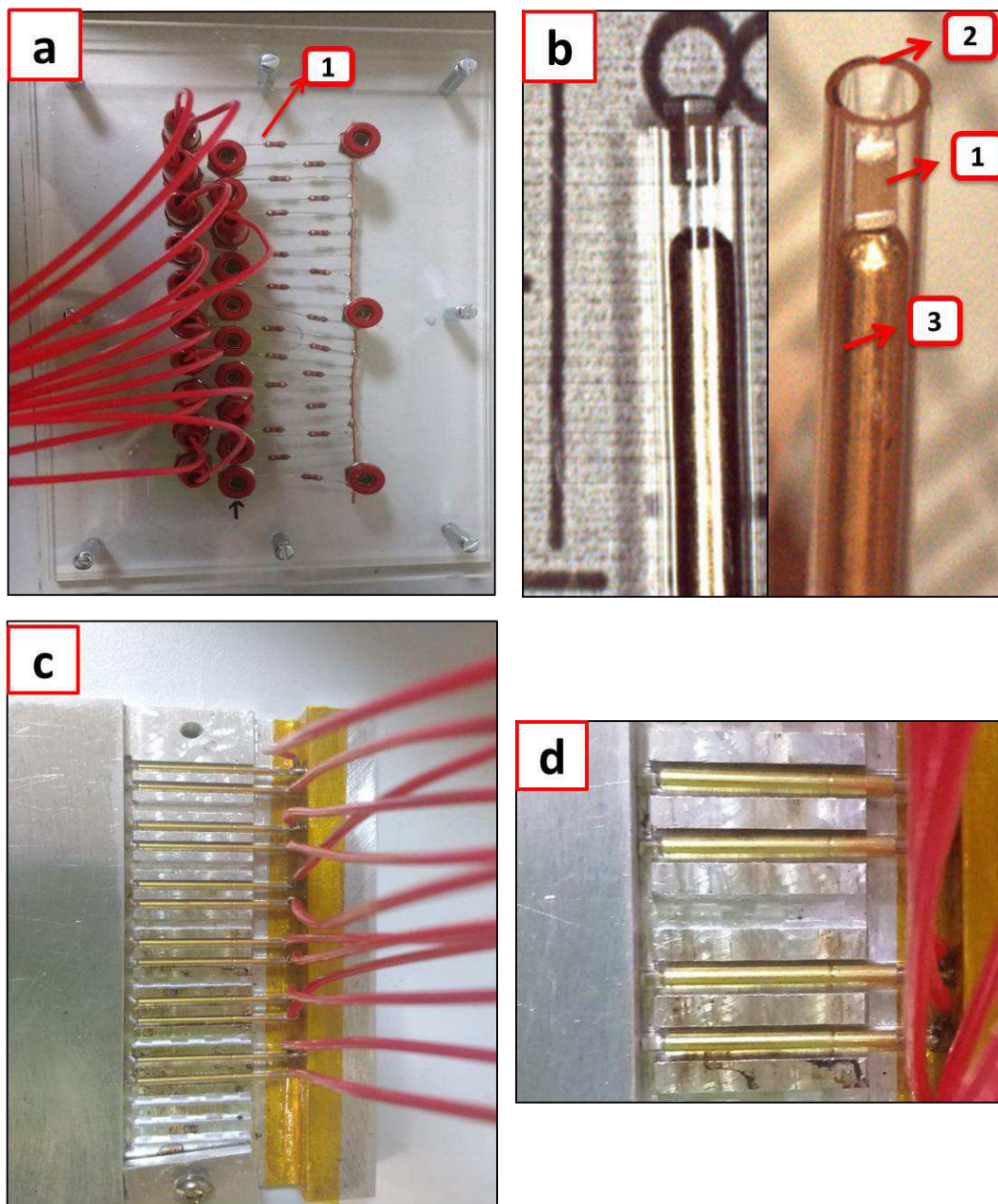
Figure 2.4. a. Plate with the protective resistors (1) connected in parallel. b. View of a MLCC (1) inside the glass capillary (2) together with a spring (3). c. View of the assembled connections (cables + springs) together with the MLCCs in the metallic plate interior canals. d. Enlarged view of the interior of the cell, in some canals are put the samples inside of a glass capillary.
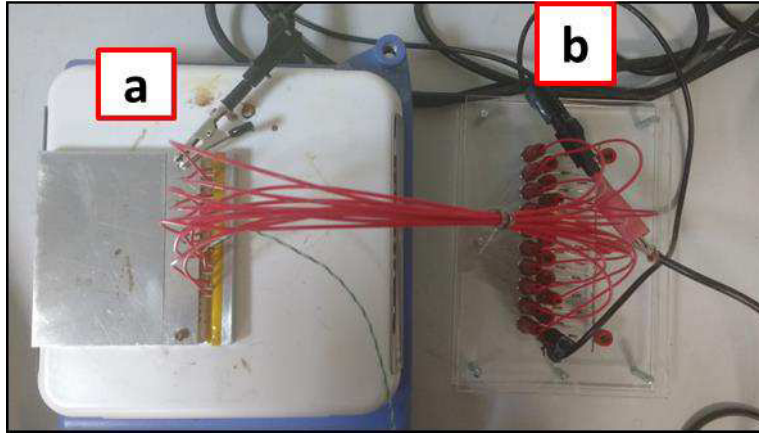
Figure 2.5. *Upper view of the set-up. **a.** Metallic cell closed over the heating plate. **b.** Plate with protective resistors.*

The capacitors are connected in parallel to a voltage source. If they are working right, the current will not pass through them; otherwise they will become conductive leading to a decrease of the resistance, reflected in a current rising. The data acquired from each HALT experiment was followed in real time with the software, being possible to know the current value in function of the time. Thus, it was possible to know when one or more samples simultaneously, had suffered a breakdown each time the current value increased. This can be seen in the Fig. 2.6, where each step is a rise of the current corresponding to an electrical broken sample. The value of that increment depends on the imposed voltage as well as the resistance value of the protective resistors. This value is constant per failed sample. In the example taken for the Fig. 2.6, under the experimental conditions shown for Fig. 2.6.A, it is 0.6 mA because the applied voltage was 600 V; while in the second case shown in Fig. 2.6.B it is 0.4 mA because the applied voltage was 400 V. When more than one sample fail at the same time, the step will correspond to the mentioned rising of current value multiplied by the number of failed samples. An example of this case is shown enclosed in a green box in the Fig. 2.6.A, the failures 6 and 7 occurred simultaneously, so that step is equivalent to 1.2 mA and the time to failure was considered two times at the moment to analyze the data. In the plots presented in Fig. 2.6, each failure is signaled with the F letter and a number, also the initial and final current values are presented. These values, as explained, are determined based on the

51

failed samples. To assure the circuit was correctly functioning, a short circuit connection was always incorporated to the system, so it was observable that the current was flowing through it and this is why the initial value of the current is not zero.
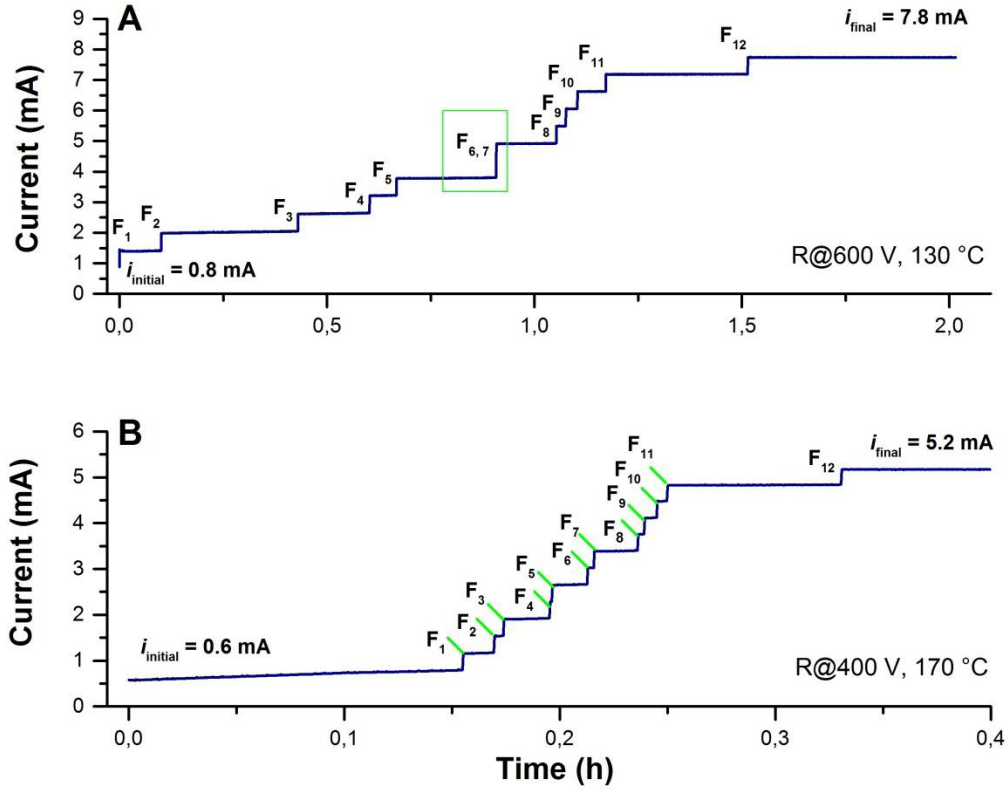
Figure 2.6. *Representation of the data acquired in a HALT experiment. (**A**) Insulation resistance measurements at 600 V and 130 °C. (**B**) Insulation resistance measurements at 400 V and 170 °C.*

2.1. Powders characterization

The barium titanate powders used as the dielectric in the production of the Group B and C MLCCs are the same that were utilized in this work for the fabrication of the ceramics described subsequently in this chapter. These ceramics will be denominated as BT-B and BT-C, respectively.

It is important to remark that BT-A powder was not used in any case to fabricate MLCCs, as well as that the base-powder of the MLCCs – Group A, was not used for this part of the work.

2.1.1. X-Ray Diffraction

The determination of the crystalline structure and phase were achieved using non-destructive analytical X-ray diffraction (XRD) analyses. This method is based on constructive interference of monochromatic X-rays and a crystalline sample. The X-rays are generated by a cathode ray tube; then they are passed through three basic steps: filtered to produce a monochromatic radiation, concentrated by collimation, and directed toward the sample. The interaction given between the sample and the incident rays produces constructive interference (and a diffractive ray) when conditions satisfy Bragg´s Law (H. Bragg, & L. Bragg, 1913):

$$n\lambda = 2d \sin \theta \qquad (5)$$

Where λ is the wavelength of the electromagnetic radiation to the diffraction angle and the lattice spacing in a crystalline sample, d is the distance between different plane of atoms in the crystal lattice, and θ is the angle of diffraction. The X-rays are then detected, processed and counted, generating a diffraction pattern that can be considered as a "fingerprint" of the material. It provides information about the crystalline phase(s) present in the sample.

In this work, X-ray analyses were performed using a Bruker D4 Endeavor diffractometer shown in Fig. 2.7. Powders and ceramics were deposited on a circular sample holder in poly-(methyl methacrylate) (PMMA). The diffraction patterns were recorded in 2θ mode from 10 to 100º with a 0.02º (2θ) step scan, the acquisition time of 21.7 s in steps and an opening angle fixed slot equal to 1º. Copper anode was used as an X-ray source emitter by using a generator (40 kV, 40 mA) with the corresponding Kα radiations ($\lambda_{K\alpha1}$ = 0.15406 nm and $\lambda_{K\alpha2}$ = 0.15444 nm). The analysis of the

obtained diffraction patterns was executed using EVA software, and the JCPDS crystallographic database to identify the phases present in the sample.

Figure 2.7. X-ray Diffractometer Bruker D4 Endeavor.

2.1.2. Induced coupled plasma atomic emission spectroscopy

This analytical technique was used for the determination of the chemical elements composition of the different starting powders. The inductively coupled plasma atomic emission spectroscopy (ICP-AES) is a technique that exploits the fact that excited electrons emit energy at a given wavelength as they return to ground state. The fundamental characteristic of this process is that each element emits energy at specific wavelengths peculiar to its chemical character. Although each element emits energy at multiple wavelengths, in the ICP-AES technique it is most common to select a single wavelength (or a very few) for a given element. The intensity of the energy emitted at the chosen wavelength is proportional to the amount (concentration) of that element in the analyzed sample (Thomson, 2012). With the determined wavelengths that are emitted by the sample and by determining their intensities, the analyst can quantify the elemental composition of the given sample

relative to a reference standard. The ICP-AES analyses for this work were executed by Marion Technologies.

2.1.3. Scanning electron microscopy

The SEM analyses were performed using a scanning electron microscope JEOL JSM-6510LV. The electron bombardment was carried out to an acceleration voltage from 0.5 kV to 30 kV. The images were obtained at 20 kV.

The samples, either powders or ceramics, were fixed over the sample holder using a graphene adhesive, and then covered with a thin layer of silver. The surface and grain morphologies were observed by this technique. Frequency counts of particles and grain sizes were performed by the analysis of several SEM micrographies with the Image J software. Gaussian distribution was applied to determine the mean size and standard deviation of the samples.

2.2. Manufacture and characterization of ceramics

2.2.1. Raw materials description

Two types of barium titanate (BT) powders were used for doping them with Y_2O_3. In the first place a reagent-grade BT (Ferro Electronic Materials INC) without additives. Then, two BT powders commercially formulated for its application as the dielectric ceramic material of X7R MLCCs. The composition of the three BT powders is shown in Table 2.2, it was determined by an inductively coupled plasma atomic emission spectroscopy (ICP-AES) analysis (performed at Marion Technologies). From these analyses it is worth to highlight the fact that the formulated powders already contain 1.05 wt% of Y_2O_3, which is one of the most common additives for BT dielectric ceramic powder and the one chosen in this work for the doping experiments.

55

Table 2.2. *Chemical composition of BaTiO₃ powders.*

	Ba	Ti	Y	Ca	Sr	Si	Mn	Mg	Co
BT_A* **Ba/Ti = 2.88**	57.55	19.96	<0.01	0.006	0.04	<0.01	<0.001	0.001	<0.01
BT_B** **Ba/Ti = 2.85**	54.67	19.17	1.05	1.34	0.09	0.30	0.05	0.29	0.012
BT_C** **Ba/Ti = 2.86**	53.86	18.85	1.05	0.57	0.09	0.17	0.05	0.006	0.017

Values are given in wt%. *: BT reagent grade (pure). **: BT commercially formulated.

The powders were also analyzed by X-ray diffraction obtaining the diffraction patterns shown in Fig. 2.8. Even though the three powders have a tetragonal structure (JCPDS: 89-1428), the definition of the peaks is better for the BT-B and BT-C powders, that correspond to the commercially formulated for its industrial application. This is due to the presence of the additives, whose interaction with the BT matrix enhances the intensity between the peaks, as seen for the (002) and (200) planes (Kim et al., 2008).
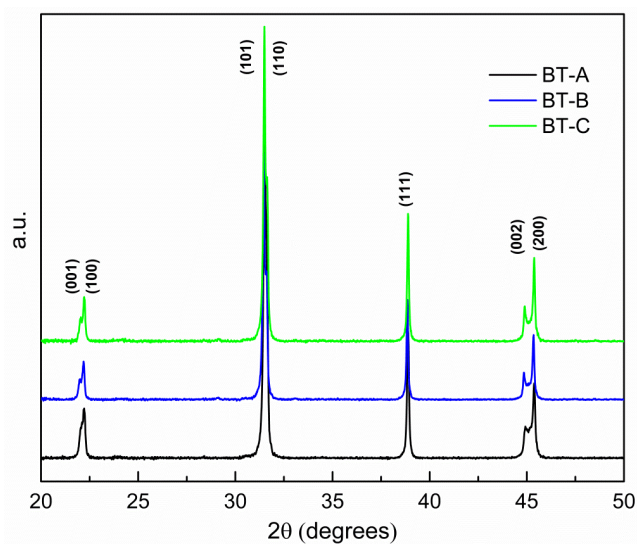
Figure 2.8. XRD patterns of BaTiO₃ starting powders. JCPDS: 89-1428.

SEM images from BT-A and BT-B were obtained and can be observed in Fig. 2.9. Both powders present similar particles morphology and their sizes are in a close range.
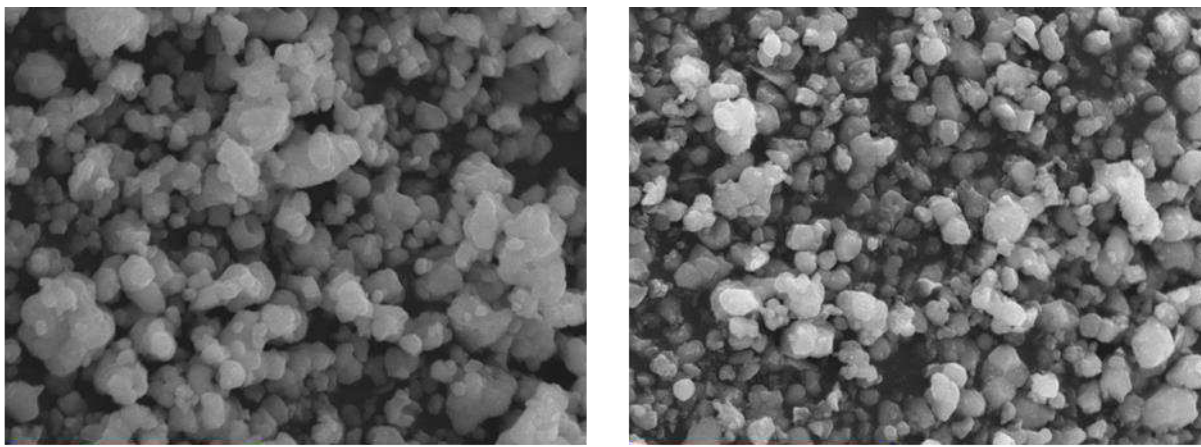
Figure 2.9. SEM images of (a) BT-A and (b) BT-B powders. Particles size: BT-A: 0.48 – 1.25 μm; BT-B: 0.46 – 0.81 μm. Scale bar: 5 μm.

2.2.2. Powders doping procedure

Barium titanate (BT) powders (composition shown in Table 2.1) were mixed with the appropriate amount of Y_2O_3 to achieve the corresponding doping concentrations presented in Table 2.2. The raw materials were mixed by traditional solid-state reaction. Powders were ball-milled in a polyurethane mill bottle with yttrium-stabilized zirconia balls, using ethanol as the grinding media for 4 h. Doped powders were dried and 1 wt% of polyvinyl butyral (PVB) was added as binder. Finally, this mixture was grinded and sieved obtaining the desired powder.

Table 2.3. *Sample identification of prepared powders doped with Y_2O_3.*

Composition (wt% Y_2O_3)→ Type of powder↓	0	1.0	1.5	2.0	2.5	5.0	20.0
BT-A*	BT-A_0	BT-A_1	BT-A_1.5	BT-A_2	BT-A_2.5	BT-A_5	BT-A_20
BT-B**	------	BT-B_1	BT-B_1.5	BT-B_2	BT-B_2.5	BT-B_5	BT-B_20
BT-C**	------	BT-C_1	BT-C_1.5	BT-C_2	------	------	------

*: BT reagent grade (pure). **: BT commercially formulated.

2.2.3. Green ceramics manufacturing

Ceramics were obtained from the powders previously prepared. The powders were compacted with a manual hydraulic press (Specac) using uniaxial pressure to compact the powders in a pressing die as shown in Fig. 2.10. Cylindrical pellets (diameter: 8 mm, thickness: 1.7 mm) were produced applying a uniaxial pressure of 300 MPa for 30 s. The mass and dimensions of each compact disk were measured before and after the sintering to determine the density value. The density values of the ceramics are reported based on the theoretical density of 6.02 g/cm^3, reported of the barium titanate.

Figure 2.10. Manual hydraulic press and pressing die during the making of green ceramics.

2.2.4. Ceramics sintering

The term sintering refers to the thermal treatment that allows the bonding of particles into a more consistent solid structure. The two principal phenomena included in sintering process are the reduction of the porosity (densification) and the grain growth. This happens by mechanisms of mass transport that often occurs on the atomic scale. From the thermodynamic point of view the sintering is driven by a reduction of the surface energy (Coble, 1961; German, 2014).

In this work, different sintering programs were used for the conducted experiments. One sintering program was performed using a laboratory chamber furnace with fiber insulation (model LF, Nabertherm). Pellets were placed over a platinum cover inside an alumina container. The thermal cycle was a two-steps program: samples were first heated to a higher temperature aiming to promote an intermediate densification, then the temperature was reduced, and a lower temperature value was held to complete the densification. This strategy has been reported to present advantages such as a uniform pore microstructure while controlling grain growth and enhancing densification (Chen & Wang, 2000; Polotai, Breece, Dickey, Randall, & Ragulya, 2005; X. Wang et al., 2006). The thermal program followed for the production of undoped and doped BT ceramics under air is

shown in the Fig. 2.11. The thermal cycle was carried out from room temperature until 1350 °C (no holding time) with a heating rate of 10 °C/min, then a cooling rate of 30 °C/min was applied till reach a sintering temperature of 1150 °C that was held for 15 h; finally, a cooling rate of 150 °C/h was used in the final stage. This two-step sintering program was used to obtain undoped and 2.5 and 5 wt % Y_2O_3-doped ceramics issued from BT-A and BT-B powders.
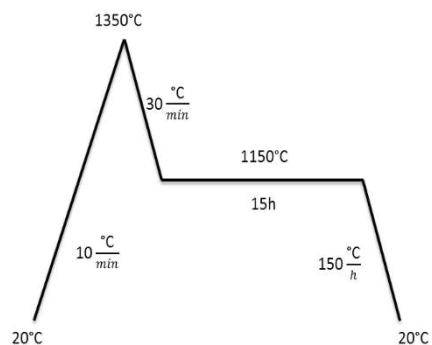
Figure 2.11. *Sintering program A: Two-steps sintering program in air. (BT-A and BT-B ceramics undoped and with 2.5 and 5 wt% of Y_2O_3).*

On the other hand, it was also performed a sintering process carried out at a company (KEMET de México). This sintering process was used aiming to mimic the industrial production conditions for the X7R-MLCCs. The thermal program and conditions are shown in Fig. 2.12; samples are fired in a kiln with reducing atmosphere and a temperature of 1310 °C hold for 3 h, then samples are taken out and passed to a kiln for a post-sintering treatment with an oxidizing atmosphere (used to restore the characteristics of the dielectric). In this case, due to the nature of the process, two set of samples were derived from each lot of processed ceramics. Each group was divided taking the half of the ceramics just after the firing under reducing atmosphere and the rest of them were passed through the re-oxidizing step.
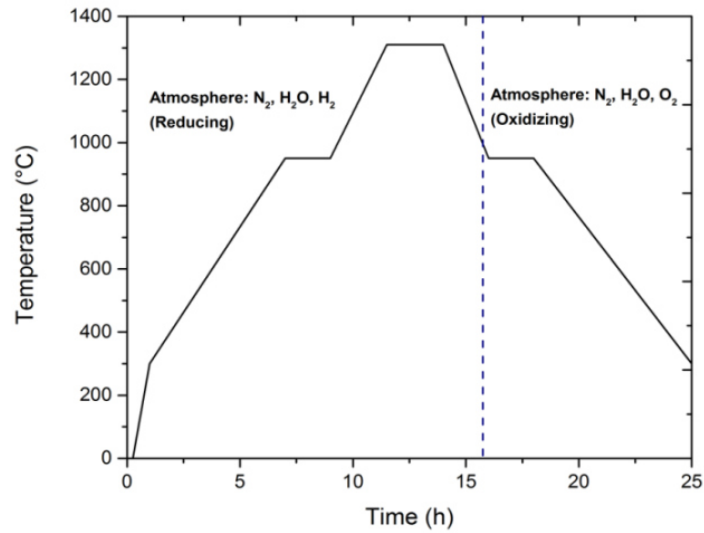
Figure 2.12. Representation of the sintering program at industrial level.

2.2.5. Thermal treatment of powders

Aiming to observe the behavior of the samples as powders, the doped ones with the higher Y_2O_3 content were subjected to a thermal program in air. BT-A and BT-B powders undoped and Y_2O_3-doped with 2.5, 5 and 20 wt%, were thermally treated in air under 1310 °C for 3h. This process was performed in a laboratory chamber furnace using the program observed in Fig 2.13.
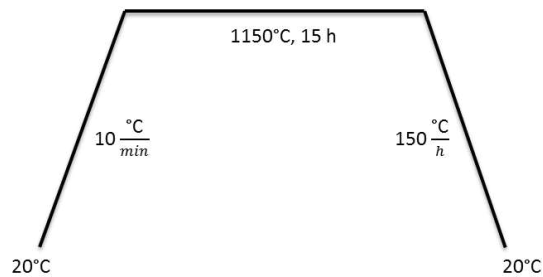
Figure 2.13. Thermal program for powders treated in air.

References

Bragg, W. H., & Bragg, W. L. (1913). The reflection of X-rays by crystals. *Proceedings of the Royal Society of London. Series A, Containing Papers of a Mathematical and Physical Character, 88*(605), 428-438.

Chen, I. W., & Wang, X. H. (2000). Sintering dense nanocrystalline ceramics without final-stage grain growth. *Nature, 404*(6774), 168-171.

Coble, R. L. (1961). Sintering crystalline solids. I. Intermediate and final state diffusion models. *Journal of applied physics, 32*(5), 787-792.

German, R. (2014). *Sintering: from empirical observations to scientific principles*. Butterworth-Heinemann.

Kim, C. H., Park, K. J., Yoon, Y. J., Hong, M. H., Hong, J. O., & Hur, K. H. (2008). Role of yttrium and magnesium in the formation of core-shell structure of $BaTiO_3$ grains in MLCC. *Journal of the European Ceramic Society, 28*(6), 1213-1219.

Polotai, A., Breece, K., Dickey, E., Randall, C., & Ragulya, A. (2005). A novel approach to sintering nanocrystalline barium titanate ceramics. *Journal of the American Ceramic Society, 88*(11), 3008-3012.

Thompson, M. (2012). *Handbook of inductively coupled plasma spectrometry*. Springer Science & Business Media.

Wang, X. H., Deng, X. Y., Bai, H. L., Zhou, H., Qu, W. G., Li, L. T., & Chen, I. W. (2006). Two-Step Sintering of Ceramics with Constant Grain-Size, II: BaTiO3 and Ni–Cu–Zn Ferrite. *Journal of the American Ceramic Society, 89*(2), 438-443.

Chapter 3

Chapter 3: Electrical characterization of MLCCs

Introduction

Multilayer ceramic capacitors (MLCCs) are one of the most important electric components used in most of the electronics areas. MLCCs present an economical volumetric efficiency for capacitance and high reliability (Wang et al., 2012). They are characterized by a high dielectric constant and thinner dielectric layers (Jain, Fung, Hsiao, & Chan, 2010). The global production of these pieces has abruptly increased with the growing of the electronic market. They are mainly demanded for its use in consumer products (notebook computers, mobile phones, digital cameras), as well as in military products (aerospace, aviation, ships, weapons) and industrial products (equipment of communication, medical electronics, automotive electronics, oil exploration) (Fantozzi, Niepce, & Bonnefont, 2013; J. Yoon, K. Lee, & S. Lee, 2009). The global production accounts for about 3 trillion units per year (Foeller, Dean, Reaney, & Sinclair, 2016), and its costs are relatively low being few USD cents per unit. During the design of consumer electronics, it is considered as a reliable component when used within the specifications. MLCCs can be fabricated with a base metal electrode technology (BME), where successive layers of dielectric and electrodes are stacked and sintered to obtain an interdigitated electrode structure. The main dielectric material is based on a ferroelectric barium titanate.

Although $BaTiO_3$ presents electromagnetic properties that make it suitable as base material for the formulation of the dielectric material for MLCCs (Tsur, Dunbar, & Randall, 2001; Wang et al., 2014), it is not by itself adapted for applications since it must follow an industrial process (shaping

and sintering) along with intrinsic properties that show a large variation with temperature. (D. Yoon, & Lee, 2004; J. Yoon et al., 2009).

Capacitors must maintain their properties within a certain tolerance in a wide range of temperatures during its lifetime. Doping remains the strategy to adapt the dielectric properties of the dielectric layer to the target application, especially for broad temperature use under high electric fields. (Ashburn, & Skamser, 2008; Paunović, Živković, Vračar, Mitić, & Miljković, 2004).

Since reliability is a critical parameter in design of electronics, components manufacturers keep track of it through different parameters. Assessment of the reliability can be very accurate trough periodic analysis of products on service and by accounting for failed products, but it is not predictive and takes a long time. Therefore, other methods need to be used to reduce the evaluation time to have an indication of the reliability prior the commercial release of the components. Accelerated test conditions have to be designed to get the most accurate prediction possible of the lifetime of capacitors in service conditions. The most common tests for reliability of MLCCs are the insulation resistance and combined stress measurements, also known as highly accelerated lifetime test (HALT). (Paulsen & Reed, 2001; Vassilious & Mettas, 2001).

Electrical systems such as capacitors may be tested using two types of tests; either constant stress test or progressive stress test can be performed. In the first type, a number of specimens are taken to their breakdown under defined stress conditions, and then the times to failure are measured; in the second type, breakdown voltages may be measured. At the moment of performing the electrical test, whatever the type, for the given conditions each tested sample will produce a different result, so the total of obtained data can be analyzed by a statistical distribution. (Chauvet & Laurent, 1992 June).

Different statistical distribution models could be applied in the data analysis from these tests, including the Weibull, Gumbel and lognormal. The Weibull distribution is widely used in this field,

and is the one used in this work, in which a two-parameter Weibull analysis is performed. (Chauvet & Laurent, 1992 June; Diaham et al., 2010).

When tailoring the properties of MLCCs, besides the initial electrical parameters, it is of great interest to analyze and seek the correlations between basic structural and chemical formulation to the reliability (time-to-failure) of capacitors. Very few studies in the literature address this, understandably because producing MLCC for reliability testing requires at least pilot size facilities to produce many samples with a reproducible process to minimize the influence of other parameters than the one being tested.

Moreover, the aim of the test is over a fixed kind of capacitors since dielectric is formulated to the best possible performance. Hence, conclusions regarding the effect of the doping over the reliability of the MLCC are rather speculative.

Given the numerous and complex interactions between the additives and dopants during and after the sintering process, a simpler approach needs to be undertaken. In this work we determine the time-to-failure of $BaTiO_3$-based X7R MLCC capacitors containing 1 %wt yttrium in their formulation.

3.1. High Accelerated Life Tests

The traditional way to evaluate the reliability of MLCCs is performing an accelerated test under a representative number of samples subjected to determined conditions of temperature and voltage with the aim to determine the time to failure using a statistical model. Also, it is possible to determine the failure modes (Liu, 2011). At industrial level this kind of tests are performed under fixed values of temperature and voltage, however they can be carried out using different values covering a broad range of stresses, with the aim to know if the failure mechanism changes depending on the value of those. (Scarpulla, 2016).

High Accelerated Life Tests (HALT) have been widely used to evaluate the reliability of electronic devices such as multilayer ceramic capacitors. The principal result of these kinds of tests is the determination of the time-to-failure (TTF) of the MLCCs when they are subjected to life stress conditions much higher than the normal using-level conditions (ambient temperature and rated voltage). The expected or average TTF is known as the mean time to failure (MTTF) which can be taken as a reliability indicator. The high-raised stress conditions are normally high voltages and temperatures that cause an electrical and thermal stress which would be not caused at normal conditions since these devices have a very long expected life (Liu, 2013 March). To evidence the moment when a breakdown occurs, the HALT follows the leakage current or insulation resistance of the MLCCs under the defined stress parameters (J. Yoon et al., 2009). The collection of TTF data from HALTs allows using it for the estimation of an activation energy associated to the electrical degradation mechanism(s) that causes the breakdown (Paulsen & Reed, 2001).

The HALT methodology normally begins by causing the failure of the electronic components, MLCCs in this case, under different combinations of electric and thermal stress. Then a failure distribution can be fitted, and the quantification of the time-to-failure is done. Having this data is then possible to determine the value of the activation energy (E_a) and get an insight of the information about the failure mechanism of the tested samples. As previously mentioned, the objective of preforming a HALT is to obtain the TTF, this value can also be used to predict median life under normal conditions of use. However, it must be used carefully and considering there are different factors beside the stress conditions that can highly influence the median life of an electronic component like ceramic capacitors.

In this study, failure data are fit to a Weibull distribution and the statistic $t_{63.2}$ is chosen as the characteristic time life of the samples. The Weibull parameters are determined and then used in conjunction with an Arrhenius model to find the activation energy related with the failure under determined conditions of the tested groups of MLCCs.

3.1.1. High Accelerated Life Test (HALT) – standard conditions

High accelerated life tests are widely used in the industries that produce ceramic capacitors in order to assure the reliability of its products. The conditions of the HALT are mostly determined by the protocols that have been developed for the different applications capacitors can have. In this way, capacitors can be tested for long periods under different combinations of temperatures and voltages. The testing voltage is given by n times the rated voltage (nVr), which is basically a voltage beyond which the capacitor will be operating under unusual conditions. Thus, it was intended to perform a HALT using industrial testing parameters in-house. The main objective of this first experiment was to examine if it is possible to take the results as a criterion to discriminate among the MLCCs groups. The HALT conditions that we will denominate as standard will be a testing period of 24 h applying 140 °C and 8*Vr = 400 V. Thus, resistance evolution was observed during the time lapse of 24 h or until a breakdown was evidenced by a conspicuous decrease of the resistance (Paulsen & Reed, 2001). Samples from three groups (A, B, and C) of MLCCs X7R-type were subjected to the HALT standard conditions (400 V and 140 °C) while following the current evolution under these conditions.

As to the groups A and B, the behaviors of their samples under the standard HALT conditions (400 V and 140 °C) are shown in the Fig. 3.1. In this figure is possible to observe the current evolution of these groups of MLCCs, each one of the "steps" correspond to an increase in the current given by the breakdown of a capacitor, i.e. each step is a failure.

As seen in this figure, the first remarkable observation is the clear shorter time in which the samples from Group B fail. The Group A showed to be affected to a lesser extent by the high voltage and temperature compared to the Group B. While the Group A did not show evidence of breakdown before 24 h, the samples from the Group B failed before this period.

Testing the samples in this way allowed us to observe the clear differences among the three groups with respect to their response when submitted to these stress conditions. The first group that showed a clearly different behavior when standard HALT conditions where applied was the Group C. It was not possible to perform the HALT at standard conditions for Group C samples since they suffered a breakdown immediately when tested at this voltage (400 V) and a temperature above 90 °C, so there is no gathering data for this group under the HALT standard parameters. However, HALT tests for this group were performed using the same electrical stress conditions but lower temperature ranges. They are certainly affected in a higher or less extension by the voltage and temperature imposed. Under these conditions, the MLCC pieces from the Group A are considered a more reliable material, bearing in mind that they did not fail at extreme conditions before 24 h. The Group B is more affected by these stress conditions, presenting higher resistance degradation over the time. Finally, the Group C is the most damaged when subjected to this test since its breakdown was instantaneous under these conditions.
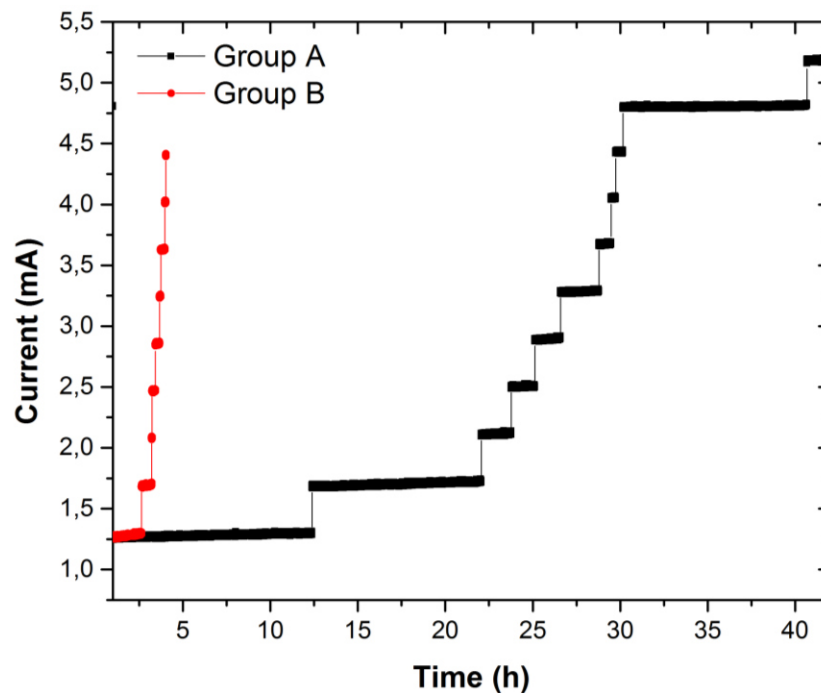
Figure 3.1. *Current evolution of Groups A and B during HALT experiment at standard conditions (400 V, 140 °C).*

From this starting point it was possible to expect that the different behavior among the groups was observed as well at different HALT combination of conditions. To confirm this, the next step was to broad the range of thermal stress.

3.1.2. Impact of temperature on breakdown of MLCCs

For a first attempt, the experiment was carried out testing one sample at time in a Signatone S-1160 probe station. The thermal stress was provided by a hot chuck system and the electrical parameters were controlled and followed by a Keithley's 2410 Source Measure Unit (SMU).

Performing high accelerated life tests in the probe station (one sample per test) allowed to follow the current and resistance evolution of the three groups of samples, when tested at 400 V and different temperatures.

A general overview of the resistance behavior of the three groups, when HALT was performed at 400 V and different temperatures, is shown in the Fig. 3.2. For the three cases, the resistance was rather stable during the beginning of the test and then it started to decrease until a rapid step down that was the signal for a breakdown of the sample.

As is possible to observe in Fig. 3.2, there is a distinct difference in the range of time that the failures of the MLCCs are produced. Even for groups A and B that were tested under the same temperatures, the longer times to failure were seen for Group A (Fig. 3.2.a). Despite the TTF for MLCCs from Group B (Fig. 3.2.b) are in the middle of the ones from Groups A and C, the values are closer to the first. In fact, Group A and B show more similitudes with regard to its behavior under higher stress values; i.e. these groups are possible to test under temperatures above of 100 °C while Group C is not. Regarding the Group C (Fig. 3.2.c) this set of samples was the most affected by the high temperature. The first evidence is that as previously said, the range of testing

temperatures had to be set to a maximum of 80 °C so the failure was not immediate and then the data showed that Group C presents the shorter times to failure of the three groups.

Since the voltage was the same in all the cases (400 V), the effect of the temperature over the resistance degradation is clear; when the thermal stress is higher the time-to-failure is shorter. This is a common effect for the three groups; however, we remind that each group of MLCCs is affected to a greater or lesser extent by the thermal stress.

a.

b.

c.
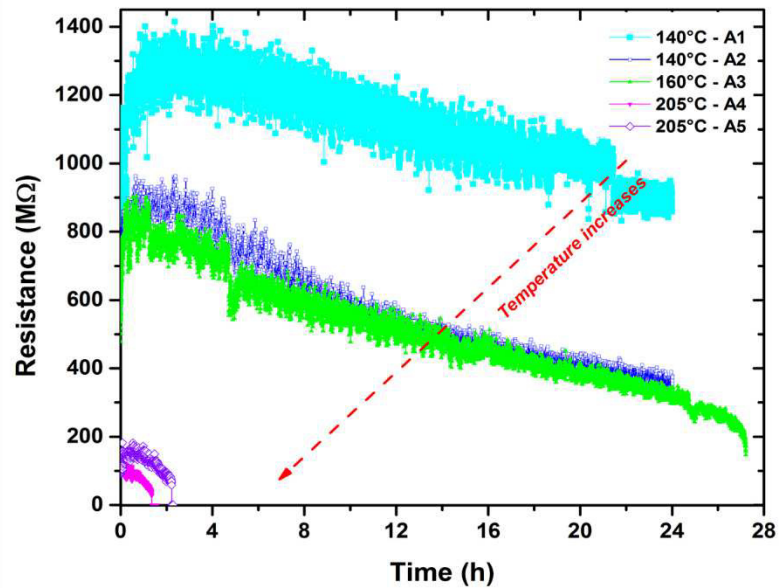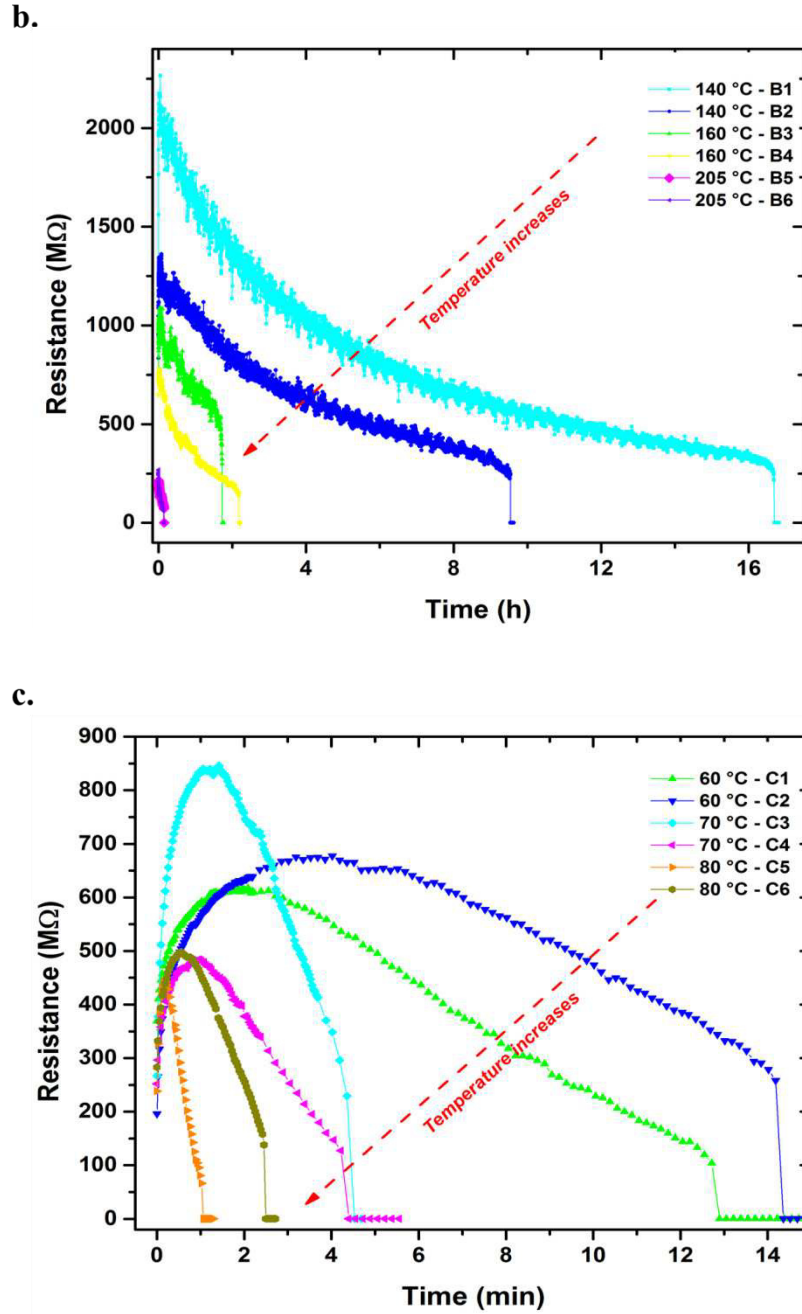
Figure 3.2. *Resistance evolution of individual MLCCs from (**a**) Group A, (**b**) Group B, and (**c**) Group C during HALT performed with 400 V and different temperatures.*

Thus, these experiments allow not only differentiate and even classify the MLCCs groups by their time-to-failure (TTF) but also provide a clear clue of how the thermal stress causes an important effect over the resistance degradation of the samples. Knowing this and considering the tests

72

reproducibility and time to perform them, the next step was to perform the HALT testing multiple samples at once under the same stress conditions. In this way, the performance of a statistical analysis of the TTF will be achieved and a characteristic life time will for each group will be obtained, which will also lead us to obtain an activation energy related with the failure of each sample.

3.1.3. Determination of Time to Failure (TTF) and Mean Time to Failure (MTTF)

The Mean Time to Failure (MTTF) is a value that provides the average life time expected for non-repairable items such as the MLCCs.

To continue with the characterization of the three groups of MLCCs, high accelerated life tests were from then performed in an in-house device that allows testing multiple samples at the same time while controlling the voltage and temperature (Section 2.3.2.4). Aiming to gather enough data to the subsequently statistical analyses, 12 samples of each group were tested under HALT.

Breakdown was assumed to have occurred when an abrupt increase in the current of about 0.4 mA (when testing at 400 V) was detected. The failure times were determined by these increments in current indicating a short circuit. This increase in current is well described in the literature, and often related to the breakdown of the layer of dielectric (Teverovsky, 2012).

The MLCCs groups have very distinct behaviors according the HALT conditions, with the breakdown times ranging from seconds (Group C) to tenths of hours (Group A). The times to failure of samples from Groups A and B when tested under standard HALT conditions are shown in the Fig. 3.3. Samples Group A last longer than the ones from Group B, having a range of TTF from approximately 22 to 30 hours, while the Group B has a TTF range from about 3 to 4 hours. Despite the early failures, both groups of samples fail with a low dispersion that allows performing HALTs with multiple samples tested at the same time, obtaining accurate data. However, as observed in the

parallel plot of the TTF for each detected failure, is possible to say that the Group A under these conditions presented less dispersion, being the majority of the failures around the same value of time.
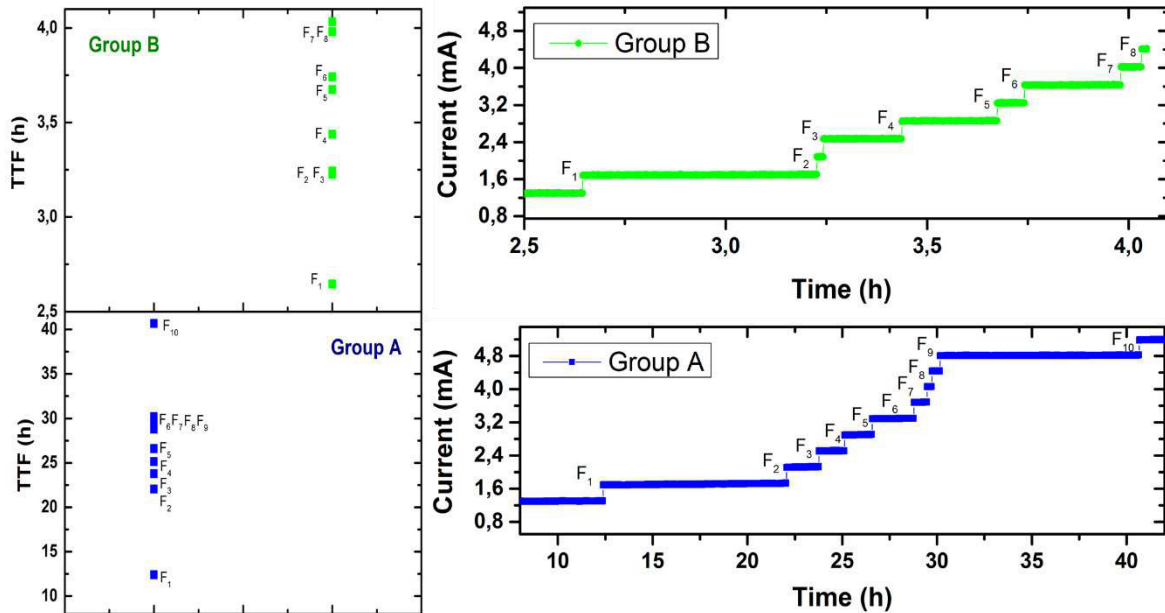
Figure 3.3. *Comparison of the TTF and current evolution for MLCCs from Groups **A** and **B** when tested under HALT standard conditions (400 V, 140 °C).*

In the Fig. 3.4 are shown the comparative plots of the obtained times-to-failure for the three groups when tested under a HALT with 400 V and different temperatures. These plots show that under these different conditions, in most of the cases (temperatures) for the three groups, the TTF data have low dispersion. The samples tend to be grouped in a lapse of time, i.e. fail at close times, although there are some samples that are early or late failures. Also, it is obvious that for the three groups the TTF decreases as the temperature increases. A closer insight of dispersion of the TTF in function of the failure sequence for each applied temperature can be seen in the Fig. 3.5.

74
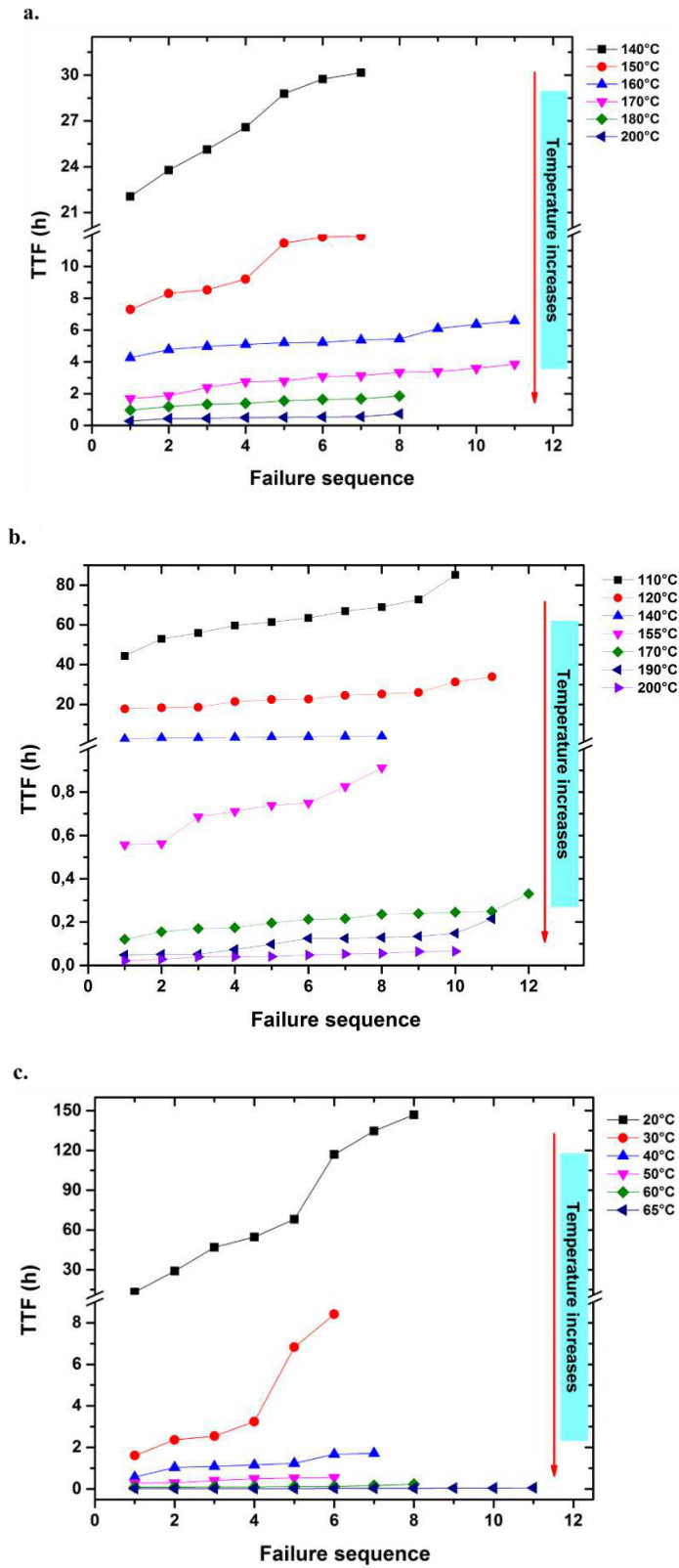
Figure 3.4. *Correlation of the time-to-failure for the failures of each group of MLCCs. HALT conditions: 400 V and temperature indicated on the plots. (**a**) Group A, (**b**) Group B and (**c**) Group C.*
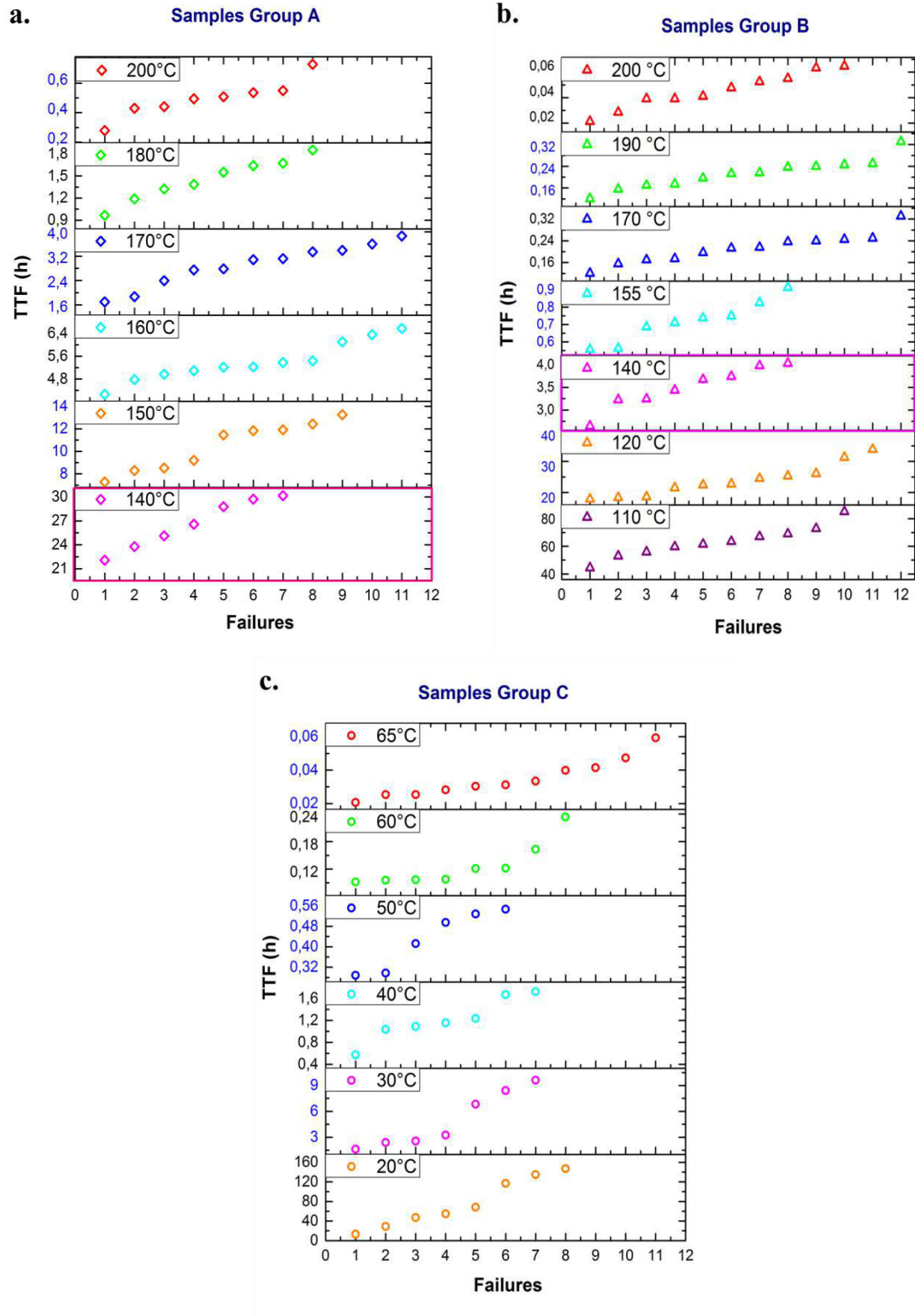
Figure 3.5. *Comparison of the TTF for MLCCs from (**a**) Group A, (**b**) Group B, and (**c**) Group C. HALT conditions: 400 V, temperature indicated on the plots.*

From these figures (Fig. 3.4.) is also observed that the dispersion of TTF decrease at higher values of temperature. This could be related with the failure mechanism and the way it is thermally activated. At low temperatures it is more difficult to overpass the activation energy necessary to start the breakdown phenomenon.

However, these results only provided an insight about the way that thermal stress affects the samples reliability. Considering this, another voltage value was applied while using a thermal stress of about the same range of temperatures, so the effect of electrical stress could also be analyzed.

In this way, HALTs were performed with an electric stress of 600 V and the results of the times-to-failure can be seen in the Fig. 3.6. Again, it can be seen the effect of the thermal stress over the TTF as it decreases while the temperature increases. However, now is possible to compare the Fig. 3.6 and Fig. 3.4 and see that there is also an effect over the TTF exerted by the electrical stress.

Comparing the TTF observed in Fig. 3.6 and Fig. 3.7 against the ones presented in Fig. 3.4 and Fig. 3.5, at the same temperatures but higher voltage, the breakdown of the samples was achieved in shorter times. Taking by example the HALT at 140 °C at both voltages, for samples of Group A and Group B and HALT performed at 60 °C at both voltages for Group C, the TTF is decreased when the higher voltage is applied as shown in Table 3.1.

Table 3.1. TTF when HALT is performed using different voltages and the same temperature.

MLCC Group and HALT temperature conditions	Range of TTF when tested at 400 V	Range of TTF when tested at 600 V
Group A – 140 °C	21 – 30 h	3 – 5 h
Group B – 140 °C	3 – 4 h	0.2 – 0.4 h

| Group C – 60 °C | 5 – 13 min | 2 – 4 min |

As seen, the drop in the TTF values can be considered as significant, decreasing in several hours for the case of Group A and Group B and some minutes for the Group C. About the dispersion of the TTF results it is as well low, as seen in the time ranges in Fig. 3.7.
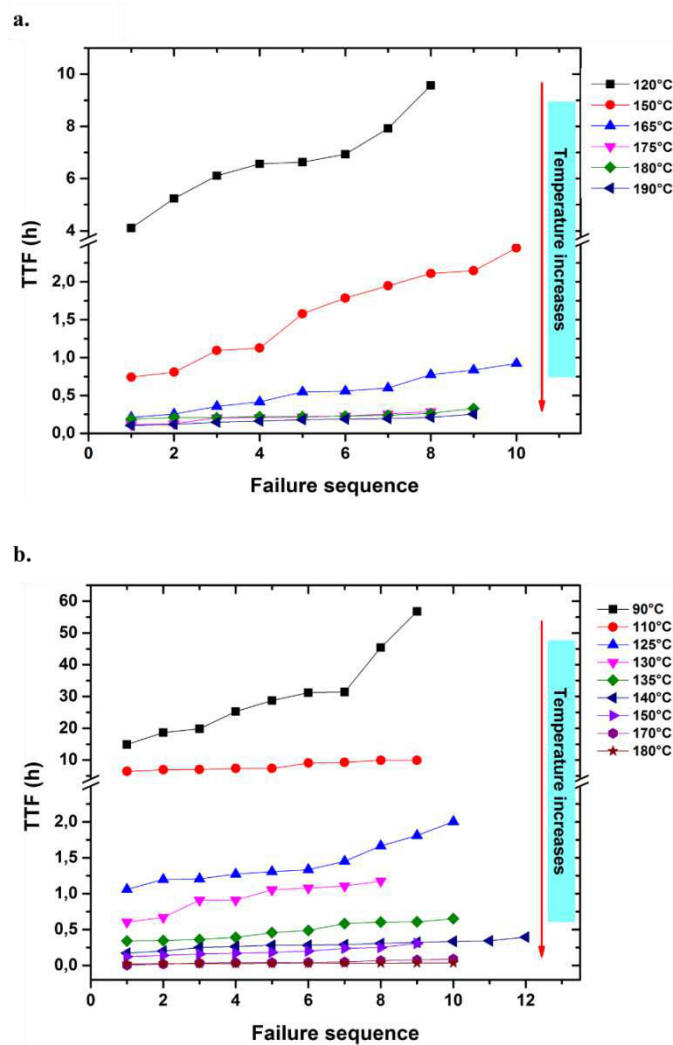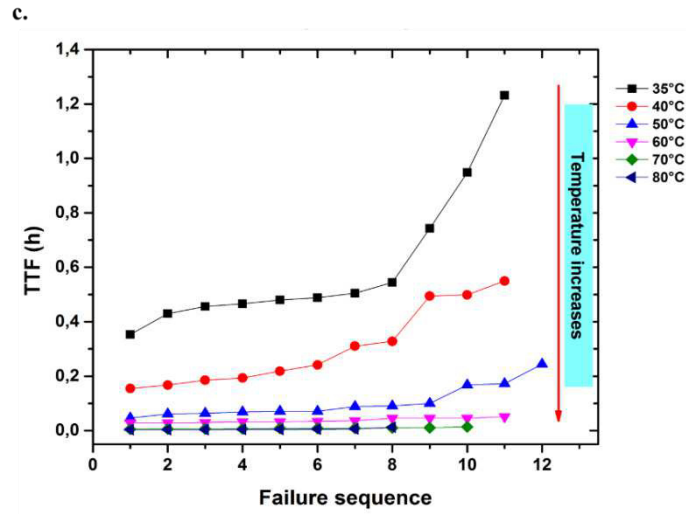
Figure 3.6. *Correlation of the time-to-failure for the failures of each group of MLCCs. HALT conditions: 600 V and temperature indicated on the plots. (**a**) Group A, (**b**) Group B and (**c**) Group C.*
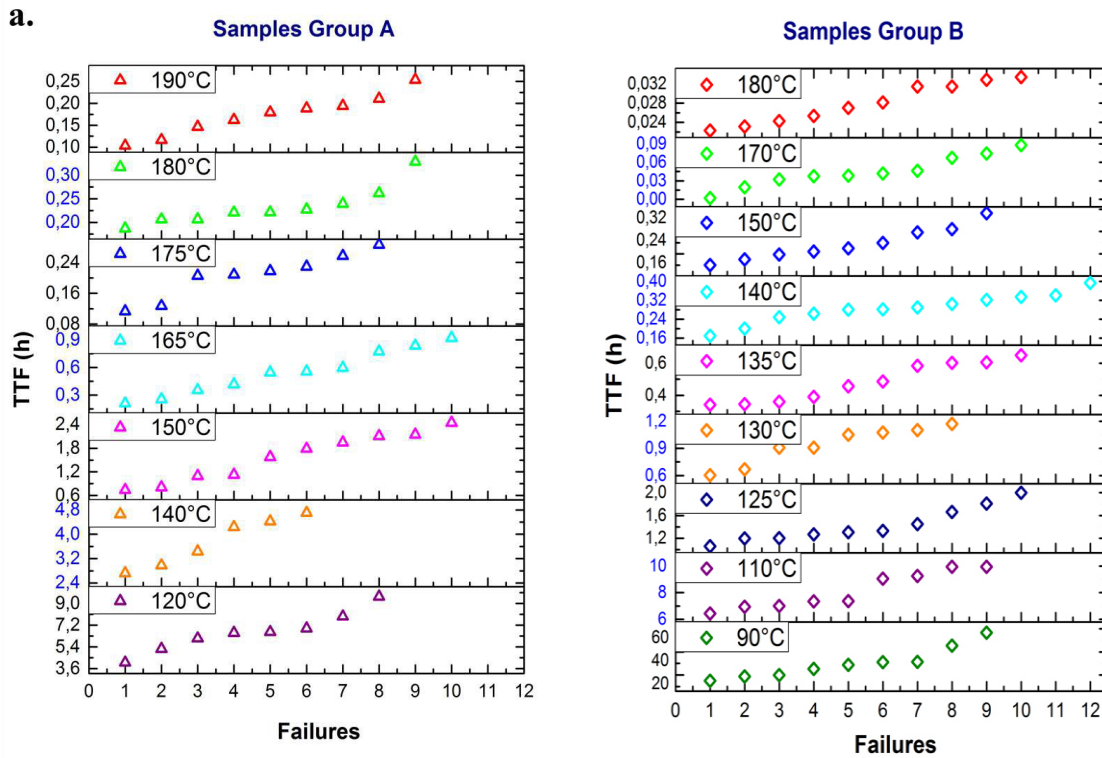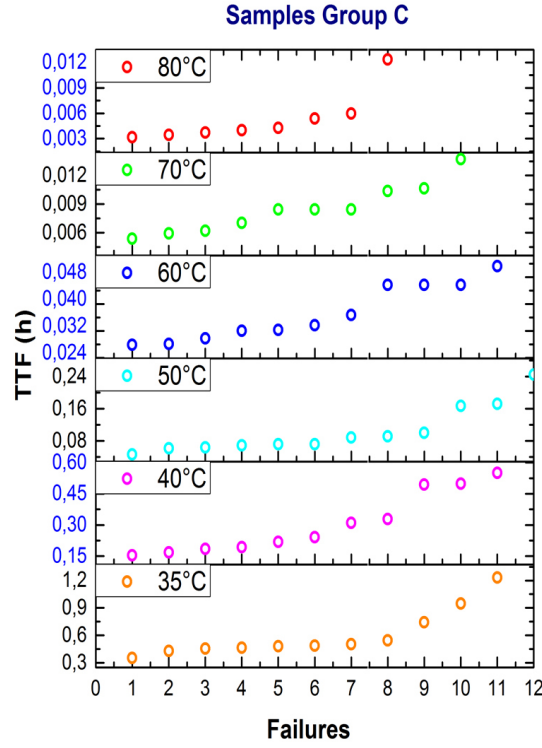
Figure 3.7. Comparison of the TTF for MLCCs from (a) Group A, (b) Group B, and (c) Group C. HALT conditions: 600 V, temperature indicated on the plots.

Until this point, it can be suspected that there is an interaction among the two stress variables. In further sections it will be analyzed considering the statistical analyses performed to the obtained results from HALT experiments.

3.2. The Weibull distribution

In this study, times to failure are fit to a Weibull distribution and the statistic $t_{63.2}$ has been chosen as the characteristic life of the samples.

The cumulative density function for the two-parameter Weibull distribution is represented by the following expression:

$$F(x) = 1 - e^{-(\frac{x-\gamma}{\alpha})^{\beta}} \qquad (1)$$

Where F(x) is the cumulative probability of failure, α is the scale parameter that represents the time or voltage for which the failure probability is 63.2%. The units of α are the same of the measured times or voltages. The shape parameter β is a measure of the range of the failure times or voltages, and, the larger its value, the smaller is the range of measured data. The location (or threshold) parameter is frequently set as zero (it implies a threshold voltage in a progressive test or a threshold time to breakdown in a constant stress one) (Abernethy, 2006; Chauvet & Laurent, 1992 June; Diaham et al., 2010).

Data sets can be complete or censored; the second group corresponds to those sample sets in which not all of them present breakdown. Both the first or second type of data sets, they must be ranked, and a good approximation can be given by the median rank equation known as Bernard's approximation (Ross, 1999):

$$F(i,n) = \frac{i-0.44}{n+0.25} \qquad (2)$$

Where i represents the rank of a failed sample and n the total number of tested samples.

For plotting the Weibull distribution law, the cumulative density function (cdf) (1) must be transformed as follows:

$$ln\left(1 - F(x)\right) = ln\left(e^{-(\frac{x}{\alpha})^{\beta}}\right) \qquad (3)$$

$$ln\left(1 - F(x)\right) = -\left(\frac{x}{\alpha}\right)^{\beta} \qquad (4)$$

$$ln\left[-ln\left(1 - F(x)\right)\right] = \beta \, ln\left(\frac{x}{\alpha}\right) \qquad (5)$$

$$ln\left[ln\left(\frac{1}{1-F(x)}\right)\right] = \beta \, ln(x) - \beta \, ln(\alpha) \qquad (6)$$

The equation 6 represents the linear way to plot the Weibull *cdf*, having as the terms:

$$y = ln\left[ln\left(\frac{1}{1-F(x)}\right)\right]; \ x = ln(x); \ b = -\beta \ ln(\alpha); \ m = \beta$$

From where is possible to obtain the values of α and β.

With the aim to know the α value, is possible to manipulate the Weibull cdf equation so this value can be read from the x-axis time scale, it can be expressed mathematically as $\alpha = x$, substituting this into the Weibull function, we get:

$$F(x) = 1 - e^{\frac{\alpha^{\beta}}{\alpha}}$$

$$= 1 - e^{-1}$$

$$= 0.632$$

The characteristic life has as unique feature that it occurs at the F(x) = 63.2% regardless of the Weibull distribution, i.e. the β value.

In the present work, the Weibull parameters have been determined applying a graphical and an analytical procedure, the median rank (MR) and the least squares method (LSM), which in fact is related with the first one and is also known as the rank regression method (RRM) because the estimation of the parameters by using it is dependent upon regressing some form of logarithm and rank transformations of the data according to the rank position (Nwobi & Ugomma, 2014; Ross, 1999).

The reliability of different samples of multilayer ceramic capacitors (MLCCs) was studied by the performing of highly accelerated life tests (HALT). Regarding fit the results to a statistical model, a number of mean time to failure (MTTF) data under various levels of electric (V) and thermal (T) stress were collected (Liu, 2013).

As previously described, data was collected from HALT at different values of temperature and two voltage values, 400 V and 600 V. It is worth to emphasize that choosing to perform the HALT using distinct voltages and thermal values that covered really low and high temperatures had the goal to observe the behavior of the insulation resistance in a wide window of imposed stresses. This was thought on the basis that it has been reported that the failure modes are related with the slope of the Weibull fitting (Abernethy, 2006; Liu & Sampson, 2012), but this parameter can be quite different depending on the range of stress levels in which the HALT is being carried out (Härtler, 1986). This could lead to an inaccurate prediction of the life-time from the TTF obtained data. In fact, there are other factors that can influence the prediction of the life time, such as the fact that to induce the dielectric breakdown under the nature of the HALT, is necessary to apply stress values that might introduce different failure mechanisms, different to the ones that could be present under normal conditions of use. Also, since more than one failure mode could be present, the statistical model used for the data analyses, must be capable to show those mechanisms (Liu, 2013).

3.2.1. Weibull analysis – Group A

The Fig. 3.8.a and Fig. 3.8.b show the life data points of MLCCs of the Group A, at 400 V and 600 V, respectively. Data was statistically analyzed and fitted according a Weibull distribution.

As seen in figures 3.18.a and 3.18.b the data fit properly with a Weibull distribution, showing an analogous behavior between the different temperatures; i.e. straight lines are obtained at different temperatures and are approximately parallel between them. Nevertheless, a different behavior of the distribution is observed for temperatures higher than 200 °C.

Thus, it could be said not only that life distribution under different thermal stress values obey the Weibull distribution but also, the failure mechanism(s) of the MLCCs – Group A appear to be the same up to a 200 °C (Wang, Gong, & Grzybowski, 2011). A change in the behavior of the failures when thermal stress is higher than 200 °C is related with a new failure mechanism. Also, the

observation of this behavior supports the choice of studying a wide range of temperatures while keeping the electrical stress constant. Our results until now show that when HALT is performed at low thermal stresses the dispersion and the distribution of the failures is not the same that at high temperatures.

From the linear equation of each plot shown in Fig. 3.8 were determined the parameters α and β, that are associated to the characteristic life and may provide a clue of physics of failure, respectively. The values of the scale parameter α and the shape parameter β for each temperature and voltage are presented in the Table 3.2. For both electrical stress values, the characteristic life decreases as the temperature increases, this behavior was also observed when testing the samples in the probe station. In the case of the α value, it is constantly reduced until the temperature is 200 °C, from there it does not present a clear pattern. The changes of α according the testing temperatures are shown in Fig. 3.9.a. In the figure is possible to see that not all the points could be fitted under a same distribution as the selected ones are in Fig. 3.9.b. With respect to the observed influence of the electrical effect, it is noticeable that it decreases the median life of the capacitors as well, so it confirms that both stresses affect significantly the resistance insulation of the samples.
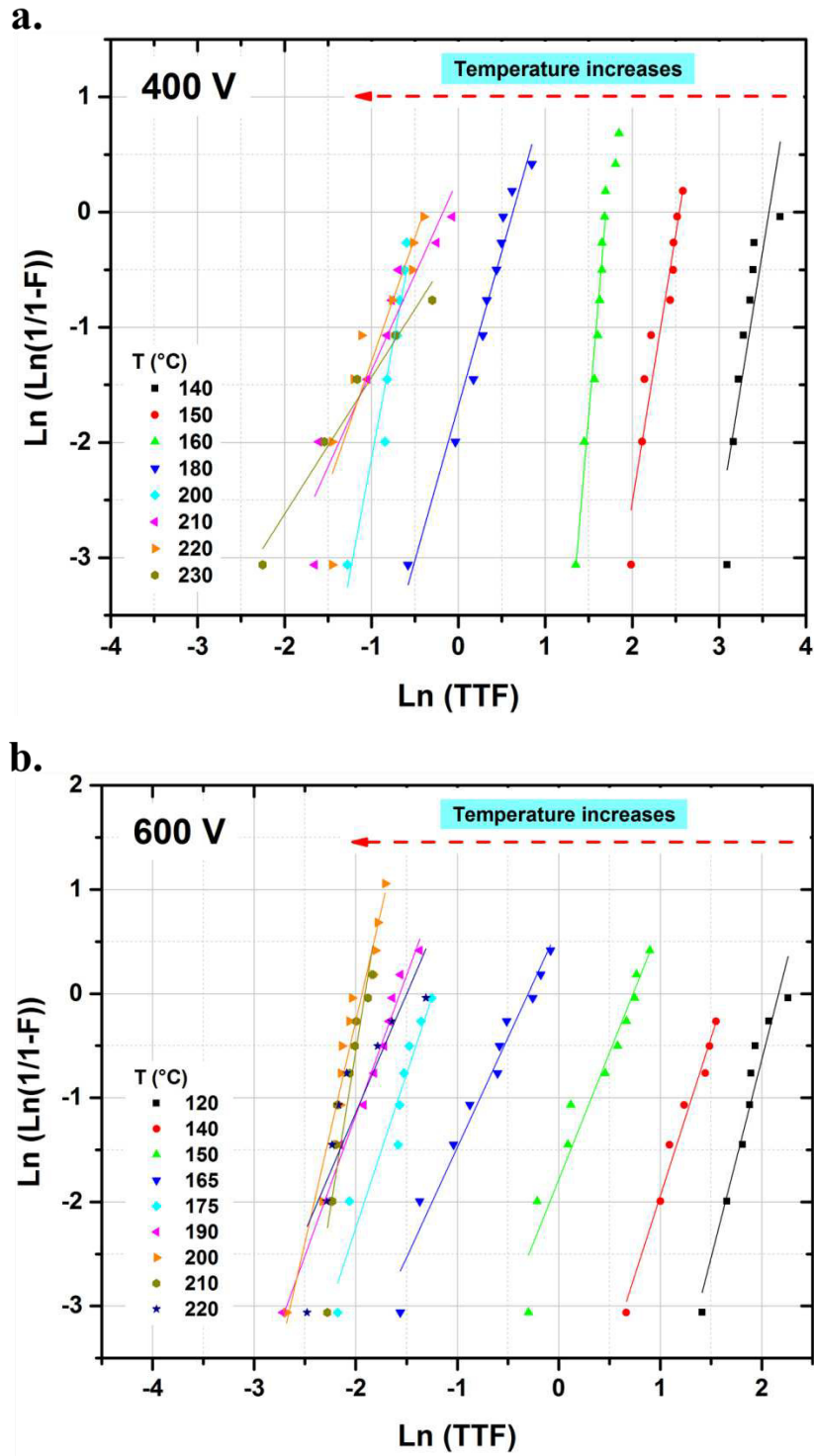
Figure 3.8. *Weibull plot for Group A. HALT conditions: (**a**) 400 V, 140 – 230 °C and (**b**) 600 V, 140 – 220 °C.*

Taking into account that the values obtained for T > 200 °C are not congruent with the expected response to the imposed thermal stress, only values below this limit were considered for further determination of the activation energy for the failure, considering that another mode of failure could be involved up to this limit.

On the other hand, the values of the shape parameter (β) determined for the data gathered using 400 V and temperatures below 200 °C are all higher than 2 and beyond that temperature they tend to be lower than 2. For the 600 V case, the β values are above 2 for all the temperatures. However, this parameter does not present a tendency in function of the temperature as can be seen in Table 3.1. It has been reported that when $1.0 < \beta < 4.0$ it implies failure due an early wear out, while if $\beta > 4.0$ it implies a rapid wear out (Liu & Sampson, 2012; Abernethy, 2006).

Table 3.2. *Weibull parameters for MLCCs - Group A.*

Voltage (V)	Temperature (°)	α (h)	β
	140	35.67	4.66
	150	12.72	4,65
	160	5.62	8.89
	180	1.87	2.68
400	200	0.63	4.02
	210	0.84	1.67
	220	0.67	2.16
	230	1.23	1.19
	250	1.01	0.85
	120	8.71	3.81
600	140	5.15	3.04
	150	2.08	2.44

165	0.74	2.12
175	0.29	2.96
190	0.21	2.69
200	0.14	4.25
210	0.15	6.05
220	0.22	2.28
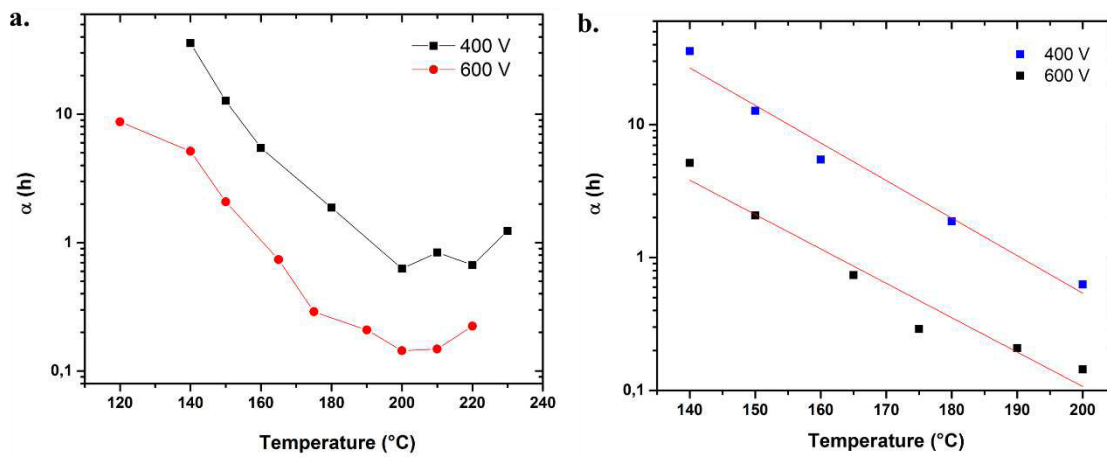
Figure 3.9. *Changes in the scale parameter of Group A in function of the HALT temperature. (a) Behavior of α over all temperatures range. (b) Linear fit of α over a selected range of temperatures.*

3.2.2. Weibull analysis – Group B

The times-to-failure of MLCCs from the Group B stressed at 400 and 600 V were determined and analyzed using the Weibull distribution. The results are shown in Fig. 3.10, in both cases of electrical stress it was found a similar behavior of data in the tested temperatures in terms of the applied fit. This leads to say that these samples fail under the same failure mode. Also, in Fig. 3.10.a is seen that when the HALT is performed at 400V and over 200 °C, the data obtained at 210 °C and 225 °C is almost overlapped with the data at 200 °C. In fact, as seen in Table 3.3, the α values for these three test temperatures (200 °, 210 ° and 225 °C) are the same.

The changes of the scale parameter are shown in Table 3.3 and more clearly in the Fig. 3.11, from there is possible to observe that it decreases as the temperature increases. Regarding the shape parameter, in this case the values are all higher than 2 and they do not present a tendency according the temperature.

The observed in the Fig.3.10 as well as the data shown in Table 3.3, show that the life of MLCCs - Group B is affected both, by higher values of thermal and electrical stress. The characteristic life decreases when either stress is applied at higher values. However, it can be considered that the failure mechanism does not change in the used range of HALT conditions.
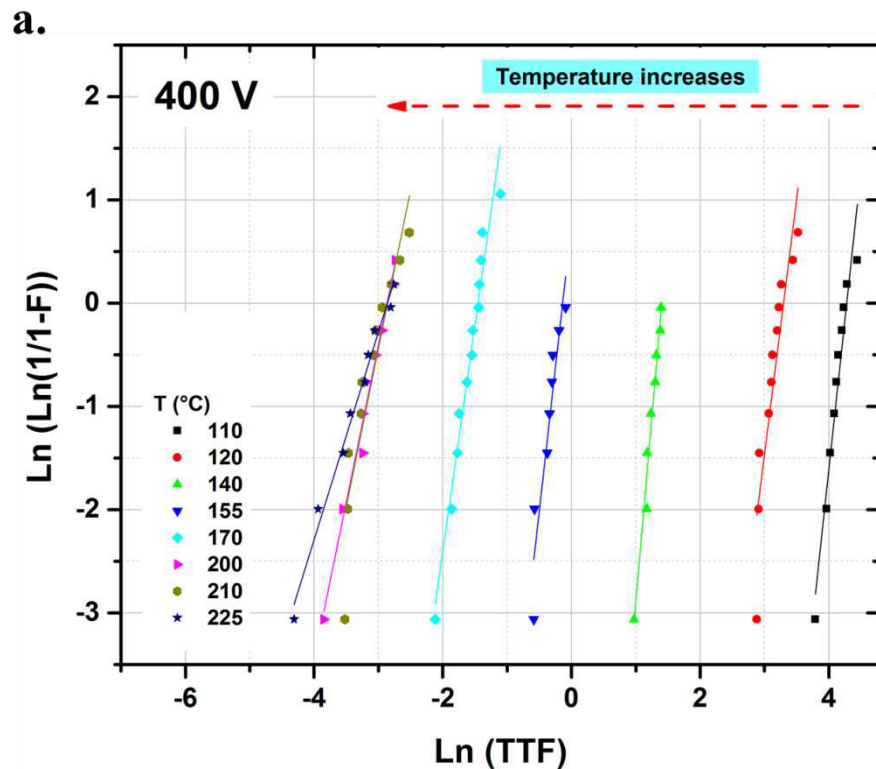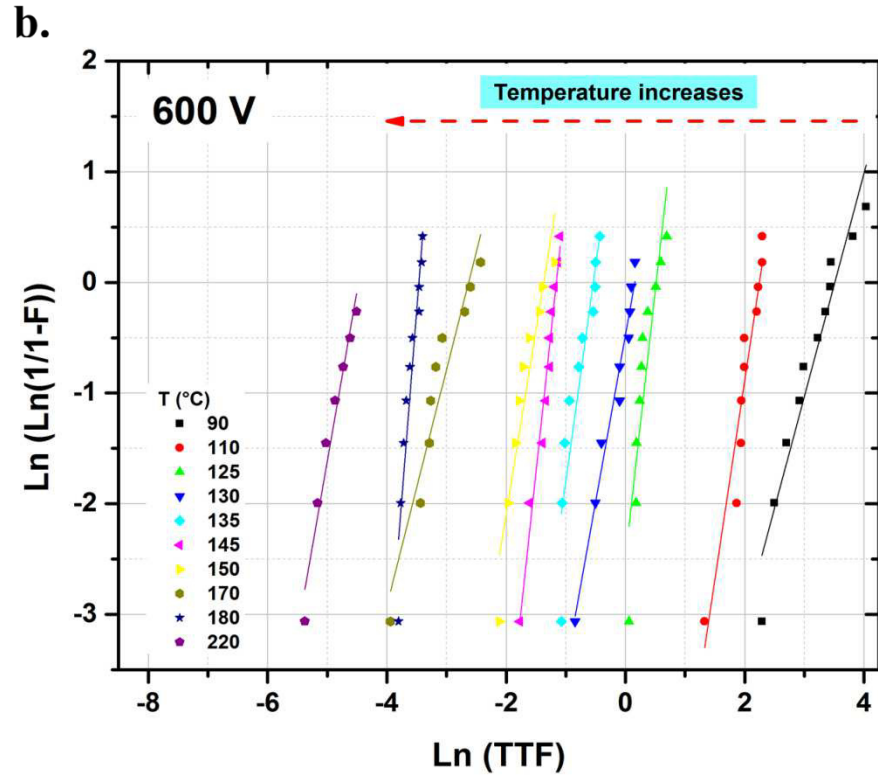
Figure 3.10. *Weibull plot for Group B. HALT conditions: (**a**) 400 V, 110 – 225 °C and (**b**) 600 V, 90 – 220 °C.*

Table 3.3. *Weibull parameters for MLCCs - Group B.*

Voltage (V)	Temperature (°)	α (h)	β
	110	72.2	5.8
	120	27.0	4.95
	140	4.07	7.16
	155	0.87	5.54
400	170	0.23	4.59
	190	0.14	2.1
	200	0.06	3.11
	210	0.06	3.06
	225	0.06	2.01
600	90	33.5	2.02

110	9.46	3.59
125	1.68	4.81
130	1.17	3.01
135	0.58	3.9
145	0.31	5.01
150	0.25	3.32
170	0.07	2.13
180	0.03	6.81
220	0.01	3.08
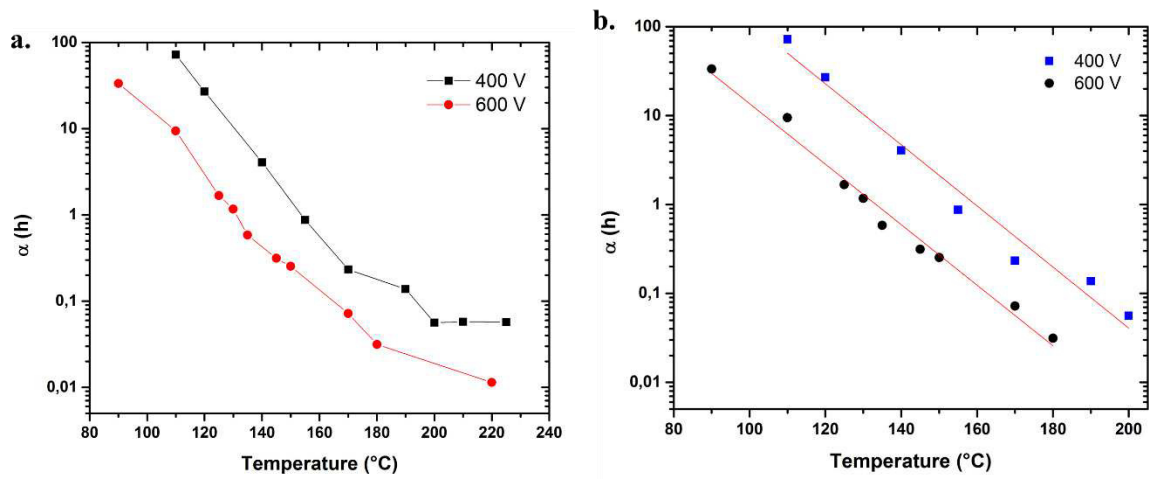
*Figure 3.11. Changes in the scale parameter of Group B in function of the HALT temperature. (**a**) Behavior of α over all temperatures range. (**b**) Linear fit of α over a selected range of temperatures.*

3.2.3. Weibull analyses – Group C

MLCCs from Group C have shown to behave different from those of groups A and B, being impossible to test them under exactly same experimental parameters. The temperature range used to test this group of samples was considerably lower than the one utilized for Groups A and B. This

fact can lead to the consideration that the dielectric material of the Group C MLCCs is less resistant to the high stress values than the one of A and B samples; i.e., it has a lower resistant insulation.

Despite this fact and also with the aim to confirm these differences, HALT experiments were conducted and TTF at different temperatures using 400 V and 600 V were determined. The Weibull analysis was performed obtaining the plots observed in Fig. 3.12 and the parameters presented in Table 3.4 and Fig. 3.13.

TTF was as well affected, decreasing when either temperature or voltage values were augmented. Also, the behavior is fitted with a Weibull model and lines are parallel-like, indicating the failure of the samples occurs under the same mechanism(s). Some deviations from this behavior are observed in the cases of 80 °C and 90 °C (Fig. 3.12.a) and 80 °C when 600V are applied (Fig. 3.12.b), which could mean that similar to the cases of Group A and B, there is a limit of temperature under the one the failure mechanisms are the same and then a change occurs. This is as well reflected in the data shown in Table 3.4 and Fig. 3.13, from where is possible to see that the characteristic life decreases at higher temperatures with some exceptions after the 70 °C in both electrical stress cases. Also, at higher voltage the mean life is lower.
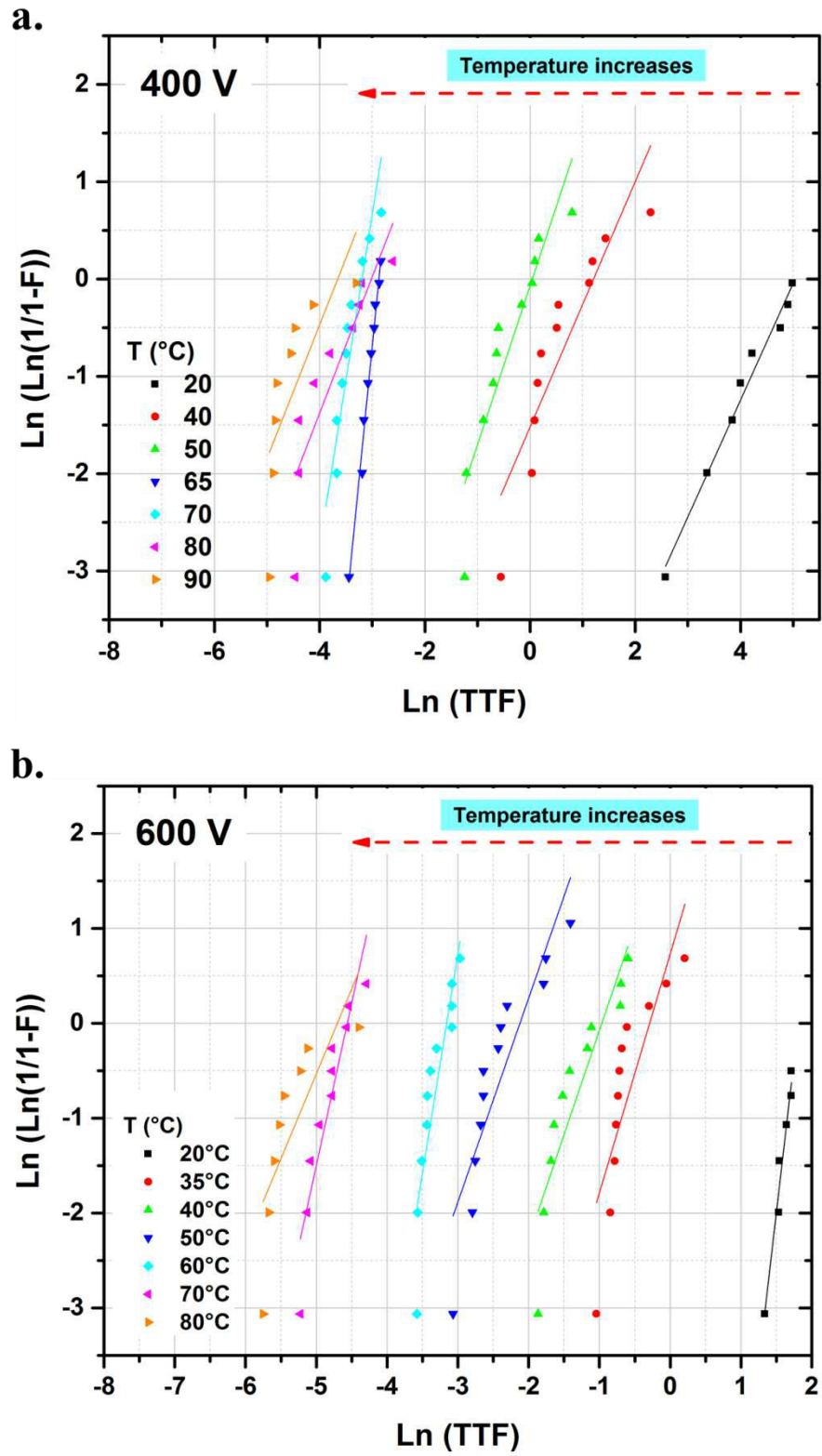
Figure 3.12. *Weibull plot for Group C. HALT conditions: (**a**) 400 V, 20 – 90 °C and (**b**) 600 V, 20 – 80 °C.*

Table 3.4. *Weibull parameters for MLCCs - Group C.*

Voltage (V)	Temperature (°)	α (h)	β
	20	154.2	1.20
	30	3.34	1.26
	40	1.04	1.63
400	65	0.06	5.45
	70	0.04	3.40
	80	0.05	1.40
	90	0.03	1.37
	20	6.11	6.44
	35	0.75	2.52
	40	0.38	2.20
600	50	0.12	2.15
	60	0.04	4.61
	70	0.01	3.42
	80	0.01	1.80
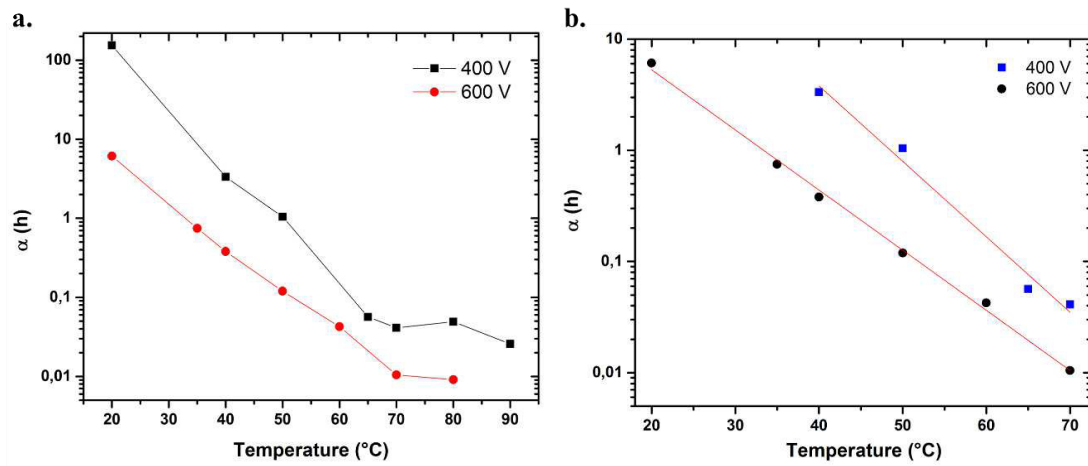
Figure 3.13. *Changes in the scale parameter of Group C in function of the HALT temperature. (**a**) Behavior of α over all temperatures range. (**b**) Linear fit of α over a selected range of temperatures.*

With the performance of high accelerated life tests at different temperatures and voltages it was possible to differentiate the groups according to its resistance insulation. According to the statistical analyses of the obtained data, the Group A has the higher mean life time, then the Group B and in the last place the Group C.

The three groups of MLCCs samples were designed based on a typical X7R composition with 1 % of Y_2O_3. However, the composition of their dielectric material, i.e. the amount of dopants in each one, is not exactly the same. This might be reflected in the behavior of the samples when they are tested under a HALT, as the results analyzed by the Weibull distribution have shown.

The following step to continue with the characterization of the samples through its characteristic life is to determine the activation energy (E_a) related to the failures. The estimation of the E_a will be based on the collected accelerated-tests data and applying the Arrhenius-Weibull model. Once the parameters of the life-stress have been determined using the Weibull distribution as the life distribution as in our case, it is possible to utilize the Arrhenius model to find the E_a value.

It is worth to remind that the activation energy that will be determined for each group of MLCCs does not represent a single particular failure mode since a combination of failure modes can be given according the tests conditions and other parameters inherent to the nature of the dielectric material such as its composition or even the production process of the ceramic capacitors (Groebel, Mettas, & Sun, 2001).

3.3. Arrhenius model applied to the analysis of combined stress (V, T) effect over MLCCs life.

The Arrhenius model was developed originally to define the rates of chemical reaction according to the temperature it is carried out. However, it has also been applied in accelerated life testing because it helps to stablish a relationship between the reliability and the thermal (i.e. temperature)

stress imposed during these tests. Commonly in the industry this model is applied with the assumption of fixed parameters that are related to defined values of failure mechanisms such as electromigration of corrosion. In the literature activation energy values can be found related to a precise type of material, electronic component or failure mode, and this is precisely what can represent an issue when using them to determine the characteristic life of a different system. The activation energy can provide clues about how the life of a product is affected by the conditions it is used under. This means that the activation energy can vary even from one product batch to another. Also, it can be different according to the present failure modes and which one can be prevalent. (Groebel et al., 2001; Hartler, 1986) In this work we chose to estimate the E_a based on the results of performed tests to get more accurate information regarding the effect of the imposed stresses by us in this study and the correlation of the same.

In this case, the level of reliability is defined by the mean time to failure (MTTF), and it is inversely proportional to a rate coefficient K. Based on the Arrhenius equation (1) we can derive the MTTF of the MLCCs as a linear function of e $^{-E_a/kT}$ (2).

$$K = A\, e^{-\frac{E_a}{kT}} \quad \textbf{(1)}$$

$$MTTF = \frac{1}{A\, e^{\frac{E_a}{kT}}} \quad \textbf{(2)}$$

$$\ln(MTTF) = -\frac{E_a}{kT} + \ln(A) \quad \textbf{(3)}$$

$$MTTF = \frac{1}{TTF} \quad \textbf{(4)}$$

In these equations k corresponds to the Boltzman's constant (8.61 x 10^{-5} eV/K), T is the absolute temperature in K, A is the pre-exponential factor, and E_a the activation energy.

In this way, using equations 1 - 4 is possible to obtain a value of activation energy as the measure of the effect that the stress imposed over the capacitor has on its life. A large activation energy value will imply a large effect of the imposed stress on product's life.

Applying the Arrhenius model, the plots shown in Fig. 3.14 were obtained. Then a linear fitting according equation (3) was adapted and the values of the activation energy were determined and are presented in Table 3.5.
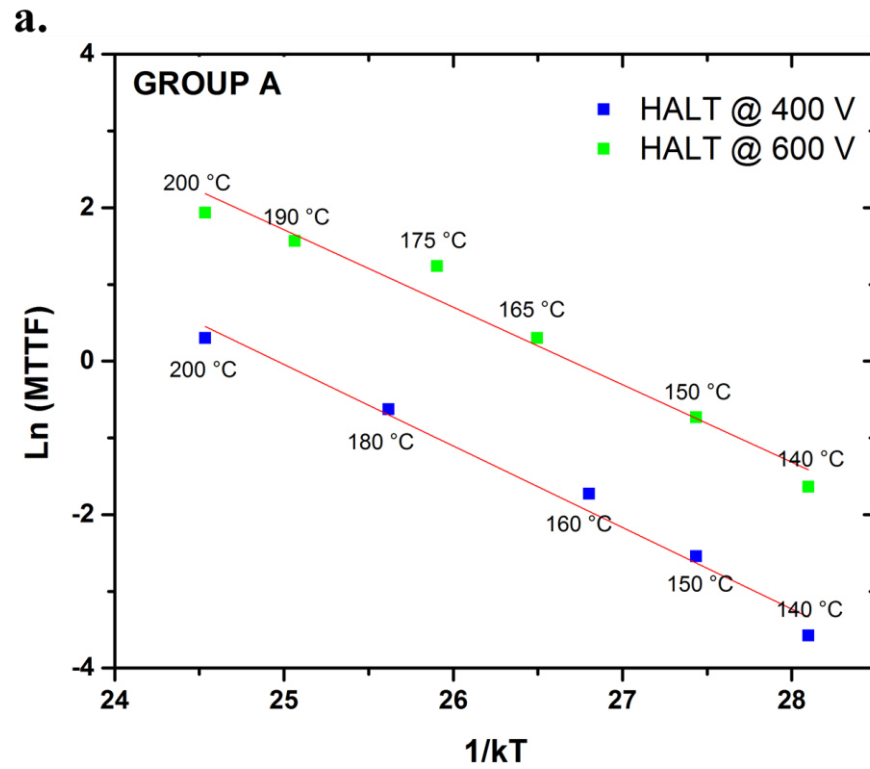
b.
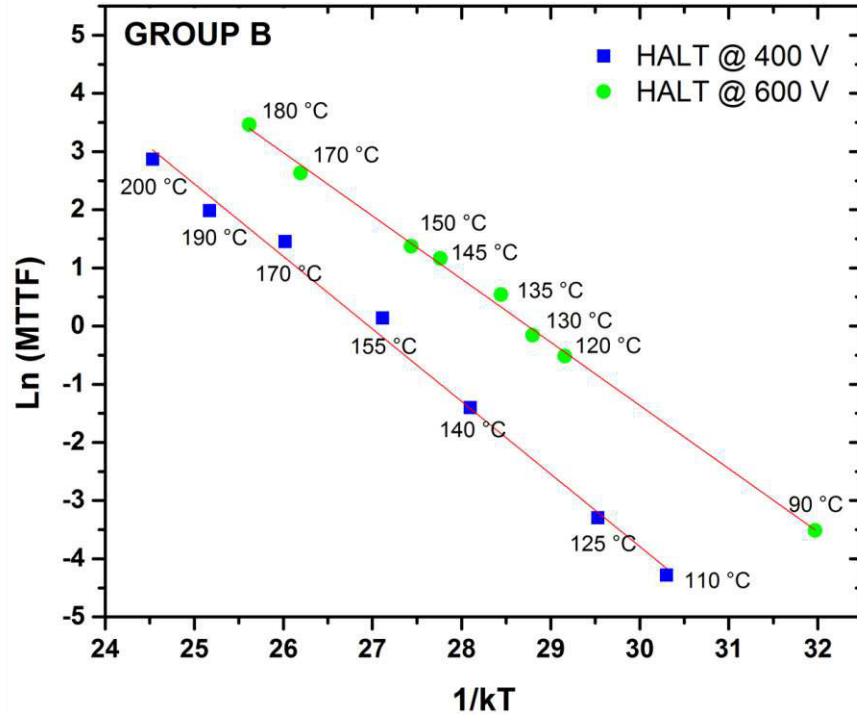
c.
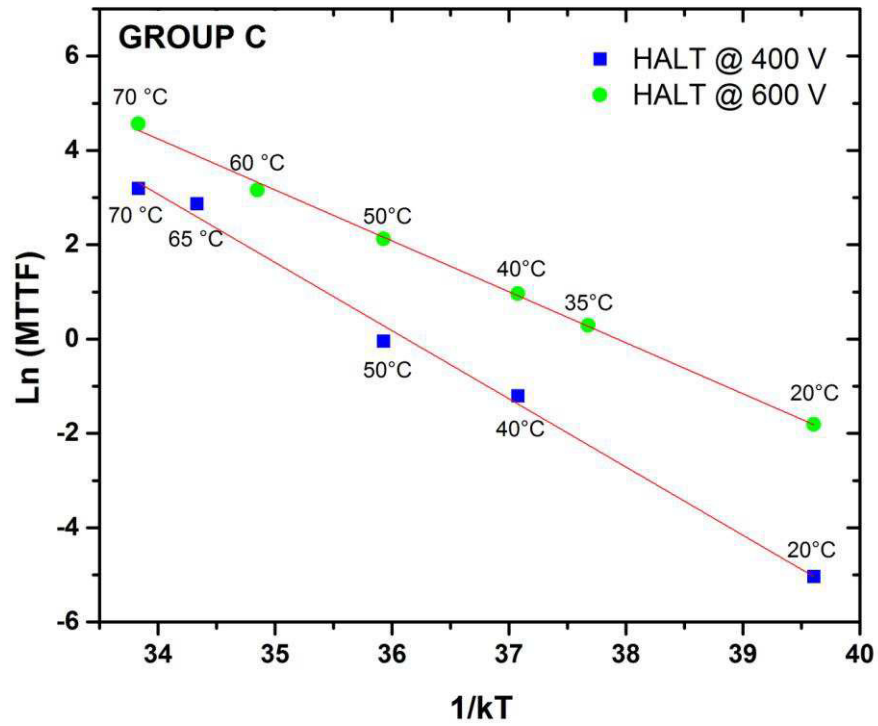
Figure 3.14. *Characteristic life according the Arrhenius model for MLCCs from (**a**) Group A, (**b**) Group B, and (**c**) Group C according the electrical and thermal stress. Solid lines represent the best fits given by equation (3).*

The activation energy values found when HALT was performed using 400 V show that the thermal effect is higher for the MLCCs from Group C, then for Group B and last the Group A. This confirms what we have previously stated, the life of MLCCs - Group A will change slowly as the temperature changes, i.e., it has better resistance insulation than the other samples. Regarding the E_a found when 600 V were applied, is possible to say that the values are different compared to the ones at 400 V for Groups B and C, while the E_a of the Group A is not significantly different when electric stress is higher. This can indicate that lives of Groups B and C are more affected when voltage is higher than life of Group A, so their failure mechanism(s) can be activated faster when the electrical stress is as well increased. Also, the E_a values for the three groups at 600 V are rather similar. These results can indicate that the electrical stress affects in a lesser extension the life of the tested capacitors than the thermal stress does it.

Table 3.5. *Activation energy values determined from Arrhenius-Weibull model.*

MLCCs Group	E_a (eV) at 400 V	E_a (eV) at 600 V
A	1.06 ± 0.07	1.01 ± 0.09
B	1.25 ± 0.05	1.09 ± 0.02
C	1.45 ± 0.06	1.08 ± 0.02

Values of activation energy that normally correspond to a certain type of failure mode can be found in the literature. Activation energy values of 1.9 eV have been associated to an avalanche breakdown mode; while for a thermal activated failure it can be in a range of 1.25 – 1.42 eV (Nomura, Miura, Arashi, Nakano, & Sato, 1996; Rawal, & Chan, 1984). In fact, for the thermal accelerated failure mode an average value of 1 eV $< E_a <$ 2 eV is considered (Liu & Sampson, 2012). On the other hand, values in a range from 1.3 – 1.5 eV have been related to a dielectric wear out in $BaTiO_3$-based dielectric capacitors (Yoon, Lee, & Lee, 2009).

Considering this and the results described in this work, such as the E_a values presented in Table 3.5, it could be confirmed that the failures were highly influenced by a thermal activated breakdown

process. It is worth to remind that electronic components may have multiple failure modes and one of them tends to prevail over the others, and the found results in this kind of works can be pointing out to it; i.e., to the one with the lower activation energy. For this reason, we consider it is better not to take the reported E_a values since it should be determined for the conditions of the experimental life test instead of simply associate one by default. Nevertheless, it is possible to use the value of the activation energy to know and describe how large it is the effect that the imposed stress is causing over the time-life of capacitors. In this work it could be seen that the capacitors (when HALT is conducted at 400V) have different E_a, giving us a clue about which one is most affected by the thermal stress.

Regarding the parameters determined by the Weibull analyses, all the shape (slope) parameters were higher than 1. This indicates that the failures cannot be reversed by a regular thermal process (burn-in) as if they were infant mortalities.

Is important to mention that with the results find in this work we cannot specifically talk about the reliability of the tested MLCCs, however we could consider them as reliable under certain use conditions. At an industrial level is rather the same way, since they are defined reliable within the determined use conditions by the producer. Also, the performance of this type of electronic components is highly related to its base-material composition itself. Considering this, we think that the differences found about the behavior of the capacitors that lead us to say that some groups are more affected by the high stress levels can be analyzed as well from a chemical compositional point of view of its dielectric material. Since it has been reported that the decrease in the insulation resistance of ceramic capacitors can be due to the formation of secondary phases such as the $Y_2Ti_2O_7$ in the $BaTiO_3$ dielectric layers (Zhang et al, 2016), we continued this work with the systematic analyses of two of the base-powders use for the fabrication of the MLCCs from Group B and Group C, considering the fact that they seem to be the less reliable. In the next part of this Chapter we are going to develop a study based on the doping of $BaTiO_3$ powders with Y_2O_3. The

aim of this study will be to drive the system in an isolated way (not in the form of capacitors but prepared as ceramics) to the formation of secondary phases and by the performance of structural and microstructural analyses determine if the $BaTiO_3$ structure can be affected by its presence, and maybe understand how this can change its electrical properties.

References

Abernethy, R. B. (2006). The new Weibull handbook fifth edition, reliability and statistical analysis for predicting life, safety, supportability, risk, cost and warranty claims. *Published and distributed by Robert B. Abernethy.*

Ashburn, T., & Skamser, D. (2008, January). Highly accelerated testing of capacitors for medical applications. In *Proceedings of the 5th SMTA Medical Electronics Symposium.*

Chauvet, C., & Laurent, C. (1992, June). Breakdown statistics as a tool to investigate electrical aging. *Conduction and Breakdown in Solid Dielectrics, 1992. Proceedings of the 4th International Conference on* (pp. 483-487). IEEE.

Diaham, S., Zelmat, S., Locatelli, M. L., Dinculescu, S., Decup, M., & Lebey, T. (2010). Dielectric breakdown of polyimide films: Area, thickness and temperature dependence. *IEEE Transactions on Dielectrics and Electrical Insulation*, *17*(1).

Ellerman, P. (2012). Calculating Reliability using FIT & MTTF: Arrhenius HTOL Model. *microsemi, Tech. Rep*.

Fantozzi, G., Niepce, J. C., & Bonnefont, G. (2013). *Les céramiques industrielles: Propriétés, mise en forme et applications*. Paris FR: Dunod.

Foeller, P. Y., Dean, J. S., Reaney, I. M., & Sinclair, D. C. (2016). Design of a bilayer ceramic capacitor with low temperature coefficient of capacitance. *Applied Physics Letters, 109*(8), 082904.

Groebel, D. J., Mettas, A., & Sun, F. B. (2001). Determination and interpretation of activation energy using accelerated-test data. In *Reliability and Maintainability Symposium, 2001. Proceedings. Annual* (pp. 58-63). IEEE.

Hartler, G. (1986). Parameter estimation for the Arrhenius model. *IEEE transactions on reliability, 35*(4), 414-418.

IEC/IEEE Guide for the Statistical Analysis of Electrical Insulation Breakdown Data (Adoption of IEEE Std 930-2004), IEC 62539 First Edition 2007-07 IEEE 930, vol., no., pp.1-53, 2007 doi: 10.1109/IEEESTD.2007.4288250.

Liu, D., & Sampson, M. (2011). Reliability evaluation of base-metal-electrode multilayer ceramic capacitors for potential space applications. *CARTS proceed*, 45-63.

Liu, D. D., & Sampson, M. J. (2012). Some aspects of the failure mechanisms in BaTiO$_3$-Based multilayer ceramic capacitors.

Liu, D. (2013, March). Highly accelerated life stress testing (HALST) of base-metal electrode multilayer ceramic capacitors. In *Proc. CARTS* (pp. 235-248).

Liu, D. D. (2015). Insulation resistance degradation in Ni–BaTiO$_3$ multilayer ceramic capacitors. *IEEE Transactions on Components, Packaging and Manufacturing Technology, 5*(1), 40-48.

Nomura, T., Miura, J., Arashi, T., Nakano, Y., & Sato, A. (1996, August). Multilayer ceramic capacitors-recent trends. In *Applications of Ferroelectrics, 1996. ISAF'96., Proceedings of the Tenth IEEE International Symposium on* (Vol. 1, pp. 135-141). IEEE.

Nwobi, F. N., & Ugomma, C. A. (2014). A comparison of methods for the estimation of Weibull distribution parameters. *Metodoloski zvezki*, *11*(1), 65.

Paulsen, J., & Reed, E. (2001). Highly accelerated lifetesting (HALT) of kemet Base-Metal-Electrode (BME) ceramic chip capacitors. In *CARTS-CONFERENCE-* (pp. 265-270).

Paunović, V. V., Živković, L. M., Vračar, L., Mitić, V., & Miljković, M. M. (2004). The effects of additive on microstructure and electrical properties of BaTiO$_3$ ceramics. *Serbian Journal of Electrical Engineering, 1*(3), 89-98.

Rawal, B. S., & Chan, N. H. (1984, May). Conduction and failure mechanisms in barium titanate based ceramics under highly accelerated conditions. In *Proceedings of the 34th Electronic Components Conference, New Orleans* (pp. 184-188).

Ross, R. (1999). Comparing linear regression and maximum likelihood methods to estimate Weibull distributions on limited data sets: systematic and random errors. In *Electrical Insulation and Dielectric Phenomena, 1999 Annual Report Conference on* (pp. 170-173). IEEE.

Scarpulla, J., Ayvazian, T., Buell, W., Campbell, M., Dubitsky, A., Lin, R., ... & Young, J. (2016, September). Thin MLCC (multi-layer ceramic capacitor) reliability evaluation using an accelerated ramp voltage test. In *Accelerated Stress Testing & Reliability Conference (ASTR), 2016 IEEE* (pp. 1-12). IEEE.

Tsur, Y., Dunbar, T. D., & Randall, C. A. (2001). Crystal and defect chemistry of rare earth cations in BaTiO$_3$. *Journal of electroceramics, 7*(1), 25-34.

Teverovsky, A. (2012). Breakdown voltages in ceramic capacitors with cracks. *IEEE Transactions on Dielectrics and Electrical Insulation, 19*(4).

Vassilious, A., & Mettas, A. (2001). Understanding accelerated life-testing analysis. In *Annual Reliability and Maintainability symposium, Tutorial Notes* (pp. 1-21).

Wang, J., Jiang, S., Jiang, D., Tian, J., Li, Y., & Wang, Y. (2012). Microstructural design of $BaTiO_3$-based ceramics for temperature-stable multilayer ceramic capacitors. *Ceramics International*, 38(7), 5853-5857.

Wang, M. J., Yang, H., Zhang, Q. L., Lin, Z. S., Zhang, Z. S., Yu, D., & Hu, L. (2014). Microstructure and dielectric properties of $BaTiO_3$ ceramic doped with yttrium, magnesium, gallium and silicon for AC capacitor application. *Materials Research Bulletin, 60*, 485-491.

Wang, Y., Gong, S., & Grzybowski, S. (2011). Reliability evaluation method for oil–paper insulation in power transformers. *Energies, 4*(9), 1362-1375.

Yoon, J. R., Lee, K. M., & Lee, S. W. (2009). Analysis the reliability of multilayer ceramic capacitor with inner Ni electrode under highly accelerated life test conditions. *Transactions on electrical and electronic materials, 10*(1), 5-8.

Yoon, D. H., & Lee, B. I. (2004). Processing of barium titanate tapes with different binders for MLCC applications—Part I: Optimization using design of experiments. *Journal of the European ceramic society, 24*(5), 739-752.

Zhang, J., Hou, Y., Zheng, M., Jia, W., Zhu, M., & Yan, H. (2016). The occupation behavior of Y_2O_3 and its effect on the microstructure and electric properties in X7R dielectrics. *Journal of the American Ceramic Society, 99*(4), 1375-1382.

Chapter 4

Chapter 4: Y_2O_3-Doping of $BaTiO_3$

Introduction

In the tailoring of $BaTiO_3$ as the base dielectric material for MLCCs fabrication, it is important to define the relations between the structure, microstructure and electrical properties. There are reports of secondary phases due to the presence of other elements, such as the dopants, which addition is intended to improve the electrical properties of the material. Among the reported phases are the pyrochlores, $Y_2Ti_2O_7$ related to Y_2O_3, that as side effect are supposed to be the cause of long term failure mechanisms of MLCCs under nominal operation (Zhang et al., 2016).

This research is aimed to find the secondary phases in this material and to perform an evaluation of the reliability of MLCCs that use $BaTiO_3$ based material that might contain those phases. All the conditions to which the ceramic is exposed during its preparation, from the raw material to the last thermal treatment, must be well known as well as the output from those steps. For that reason, it is necessary to perform powders and ceramic characterization by techniques such as Induced Coupled Plasma (ICP) spectroscopy, X-Ray Diffraction analyses and SEM, to know the chemical composition, structure and phase composition, porosity and grain size, respectively.

The formulation used in this application must be designed to control the electromagnetic properties of the layer, especially at high temperature and under high electric field (Ashburn & Skamser, 2008; Yoon, Park, Hong, & Sinn, 2007) so that several additives and dopants are added to $BaTiO_3$. They include cations such as Mn^{2+}, Mg^{2+} and Ca^{2+}, which can partially compensate the electrons and holes in the system due to the presence of oxygen vacancies (Yoon et al., 2007; Yoon, Kang, Kwon, & Hur, 2010). They also include sintering aids, such as SiO_2, which reduce the sintering

temperature. Indeed, it has been reported that SiO_2 leads to the formation of a liquid phase from the ternary system BaO-TiO_2-SiO_2, diminishing the eutectic point from 1320 °C to near 1260 °C (Liu & Roseman, 1999; Koschek & Kubalek, 1987; Ösküs, Torman, S. Sen, & U. Sen, 2016). Rare-earth elements (Dy^{3+}, Ho^{3+}, Sm^{3+}, La^{3+}, Yb^{3+} or Y^{3+}) have been used as well; they substitute Ba and Ti sites in the $BaTiO_3$ structure (Zhang et al., 2016; Wang et al., 2014a). However, in particular Dy^{3+}, Ho^{3+} and Y^{3+}, have shown an amphoteric behavior (occupying A- or B-site) which claims to be helpful for the lifetime of the MLCCs (Tsur, Dunbar, & Randall, 2001). Y_2O_3 is commonly employed as dopant in the commercial formulation of powder for industrial fabrication of MLCCs because it results in similar properties than adding Ho_2O_3, Er_2O_3 or Dy_2O_3, and it is less expensive (Zhang et al., 2016). Dopants also take part in the formation of a so-called "core-shell" structure that is claimed to contribute to the temperature stability of the dielectric properties (Kim et al., 2008; Park et al., 2009; Wang et al. 2014; Zhang et al., 2016). Y^{3+} ionic radius (0.107 nm) is intermediate between that of the Ba^{2+} ion (0.161 nm) and the Ti^{4+} ion (0.06 nm). Therefore Y^{3+} can occupy either Ba^{2+} or Ti^{4+} cation site in the $BaTiO_3$ lattice (Tsur et al., 2001; Wang et al., 2014) and can behave as acceptor or donor according to the position in the lattice. The energy required to form a Ti^{4+} vacancy in the $BaTiO_3$ lattice is 7.56 eV whereas it is only 5.94 eV to form a Ba^{2+} vacancy (Belous, V'yunov, Kovalenko, & Makovec, 2005; Makovec, Samardžija, & Drofenik, 2004; Paredes-Olguín, Lira-Hernández, Gómez-Yañez & Espino-Cortes, 2013). The partial pressure of oxygen and sintering temperature will also induce the formation of Ba^{2+} or Ti^{4+} vacancies, leading Y^{3+} to occupy either one or both (Belous et al., 2005; Paredes-Olguín et al., 2013). This will be influenced also by the Ba/Ti ratio, the dopant concentration and its solubility, which varies according to Y^{3+} occupying either the Ba- or the Ti-site. Zhi et al. (1999) indicated a solubility of Y^{3+} at the Ba-site of about 1.5 at% when sintering in air at 1440 – 1470 °C, while it reaches 4 at% when sintering under reducing conditions (V'yunov, Kovalenko, Belous, & Belyakov, 2005). For the Ti-sites instead, the solubility is higher, i.e. around 12.2 at% at 1515°C when sintering in air. Wang et al. (2014a) reported that the introduction of Y^{3+} in the $BaTiO_3$ lattice can lead to structural

changes going from tetragonal to a so-called pseudocubic phase transformation. Also, it has been observed that the solid solubility of the dopant in the $BaTiO_3$ is surpassed, when secondary phases are formed as precipitates. In the case of Y^{3+}, Belous et al. (2008) reported the formation of the $Ba_6Ti_{17}O_{40}$ and $Y_2Ti_2O_7$ as secondary phases. The pyrochlore phase $Y_2Ti_2O_7$ was evidenced by Yoon et al. (2007) and Zhang et al. (2016) and they suspected that these phases are detrimental to the reliability of $BaTiO_3$-based MLCCs.

In this work, the role of Y_2O_3 was evaluated on two kinds of raw materials. The first one is pure $BaTiO_3$ while the second material is a commercial formulation designed for MLCCs of X7R type (-55 °C and 125 °C, 15% tolerance) which among other elements, already contains 1.05 wt% of Y_2O_3.

Powders and ceramics with different Y^{3+} doping concentrations (1 up to 20 wt%), as Y_2O_3, were prepared and subsequently thermally treated or sintered, respectively. The aim was to investigate the structural changes of $BaTiO_3$ induced by the doping with Y_2O_3 and to promote the formation of secondary phases.

4.1. BaTiO₃ raw powders

The chemical composition of the $BaTiO_3$ powders used as raw materials was determined by ICP analyses and is shown in Table 4.1. As previously mentioned, the powders that are formulated for an industrial application contain dopants and additives. In Table 4.2 is presented a brief summary of the function that these components should exert in the formulation of the $BaTiO_3$ powders as dielectric base of ceramic capacitors.

Table 4.1. *Ba/Ti ratio and chemical composition of BaTiO₃ powders.*

	Ba	Ti	Y	Ca	Sr	Si	Mn	Mg	Co
BT_A* **Ba/Ti = 2.88**	57.55	19.96	<0.01	0.006	0.04	<0.01	<0.001	0.001	<0.01
BT_B** **Ba/Ti = 2.85**	54.67	19.17	1.05	1.34	0.09	0.30	0.05	0.29	0.012
BT_C** **Ba/Ti = 2.86**	53.86	18.85	1.05	0.57	0.09	0.17	0.05	0.006	0.017

Values are given in wt%. *: BT reagent grade (pure). **: BT commercially formulated.

Table 4.2. *Additives and dopants on BaTiO₃ dielectric formulation.*

Compound	Function
SiO_2	Sintering aid that contributes to a better densification. Can contribute to the creation of a liquid phase reducing the sintering temperature.
Mg^{2+}	Involved in the core-shell creation. Can replace Ti^{4+}-sites inhibiting the grain growth.
Ca^{2+}	Can substitute A- or B-sites causing beneficial changes at a structural and electrical level. Contributes to enhance the reliability.
Mn^{2+}	Added to keep high insulation resistance. It can also inhibit the grain growth.
Rare Earth Element (REE)	Particularly the amphoteric such as Dy^{3+}, Ho^{3+} and Y^{3+} (the one used in this case) have demonstrated to improve the MLCCs insulation resistance. Also involved in the core-shell creation.

The denomination of the different samples according to the starting powder and the final concentration of Y_2O_3 is shown in the Table 4.3.

Table 4.3. *Sample identification of prepared powders doped with Y_2O_3.*

Composition (wt% Y_2O_3)→ Type of powder↓	0	1.0	1.5	2.0	2.5	5.0	20.0
BT-A*	BT-A_0	BT-A_1	BT-A_1.5	BT-A_2	BT-A_2.5	BT-A_5	BT-A_20
BT-B**	------	BT-B_1	BT-B_1.5	BT-B_2	BT-B_2.5	BT-B_5	BT-B_20
BT-C**	------	BT-C_1	BT-C_1.5	BT-C_2	------	------	------

*: BT reagent grade (pure). **: BT commercially formulated.

4.2. BaTiO₃ powders thermal treatment and characterization

With the aim to observe any structural change induced by high level of doping, the powders BT-A_2.5, BT-A_5, BT-A_20, BT-B_2.5, BT-B_5, and BT-B_20 were thermally treated (TT) at 1310°C in air for 3 h. This thermal treatment replicates the sintering temperature conditions in which multilayer ceramic capacitors are produced at industry level. In this case the powders are denominated BT-X_YTT, where "X" indicates the raw $BaTiO_3$ powder, "Y" the Y_2O_3 wt%, and "TT" thermally treated.

- **Particles morphology and size**

SEM images of the undoped $BaTiO_3$ powders, BT-A_0 and BT-B_1, are shown in Fig. 4.1.a and Fig. 4.1.c respectively. Both powders present particles with a coarse-faceted morphology. Two particle sizes are observed, a range of 0.48 μm and 1.25 μm for the BT-A_0, and of 0.46 μm and 0.81 μm for the BT-B_1. The mean size value of the particles from BT-B_1 is roughly lower than the one of the BT-A_0 particles. This slight difference is probably related to the treatment given to the formulated powder to fulfill the particle size required for its use in the MLCCs production process.

After thermal treatment at high temperature, the SEM images of Y_2O_3-doped powders BT-A_5TT and BT-B_5TT (Fig. 4.1.b and Fig. 4.1.d), show more rounded and defined particles, compared to the non-thermally treated, non-doped powders (Fig. 4.1.a and Fig. 4.1.c, respectively). The mean grain size is similar for the two powders, respectively 0.58 μm and 0.53 μm. Some aggregates are observed, probably due to a beginning of sintering.
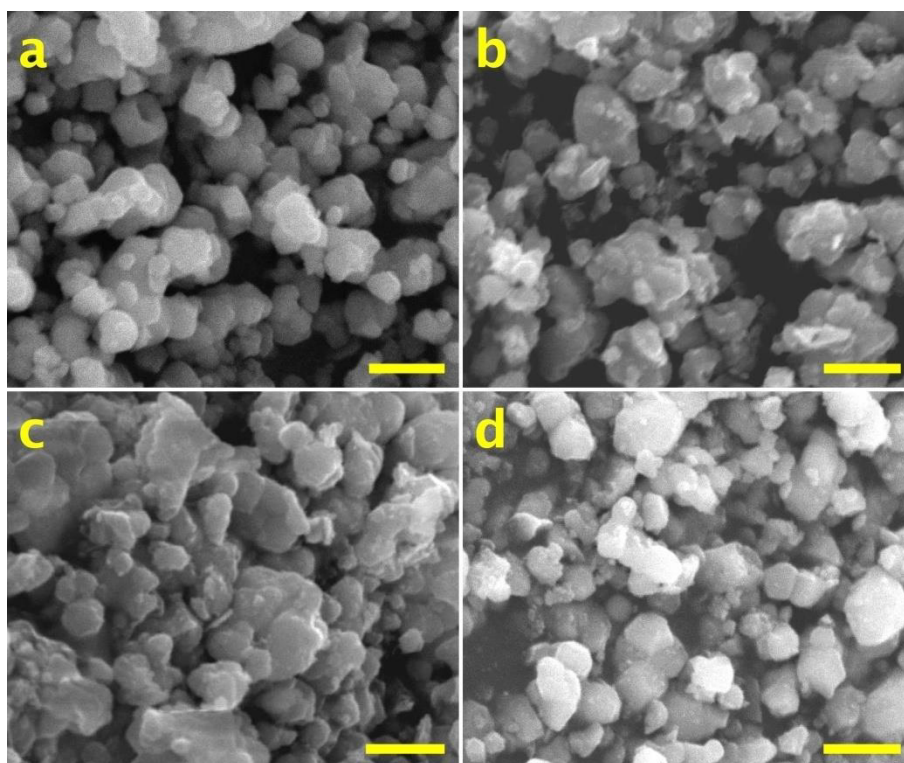
Figure 4.1. SEM images of BaTiO₃ undoped raw powders and the respectively 5 wt% Y₂O₃-doped and thermally treated powders. (a) BT-A_0, (b) BT-A_5TT, (c) BT-B_1 (d) BT-B_5TT powders. Scale bar: 1μm

- **Structure and phase composition**

The way that the $BaTiO_3$ structure can be affected by an added dopant can be reflected in the c/a ratio, which changes from cubic structure (c/a = 1) to higher values when the crystal lattice is modified for reasons like the presence of other ions. This change in the c/a ratio is reflected directly in the diffraction pattern. For $BaTiO_3$ with a cubic crystalline phase, sharp peaks in a 2θ value

110

around 31.6° and 45.3° corresponding to the (110) and (200) planes respectively, are observed. When the symmetry of the system is not cubic anymore, it causes that certain planes can appear on the diffraction pattern. Thus, in some zones where just one peak was observed, are now spotted two or more depending on the crystalline arraignment. In the case of a tetragonal phase, the planes (101) and (110) will be seen, as well as the (002) and (200) around the same 2θ values previously mentioned. We calculated a theoretical change of the 2-theta value for the (002) plane as a function of the possible c/a ratio is shown in the Fig. 4.2. A change in the c/a ratio is more notorious for (002) and (200) planes since the distance between their peaks is higher than the one of (101) (110) peaks. In fact, as long as c/a value increases, the distance among their peaks is intensified; i.e. at higher values of c/a the tetragonality is more evident. Also, the intensity ratio among (002) and (200) peaks, when the $BaTiO_3$ is in a tetragonal phase, is 1:2. However if there is a gradient in the composition of the matrix, it is possible to have the presence of various c/a ratios, which leads to a different appearance of the peaks. They can look less intense, broaden and even like if they were joining.
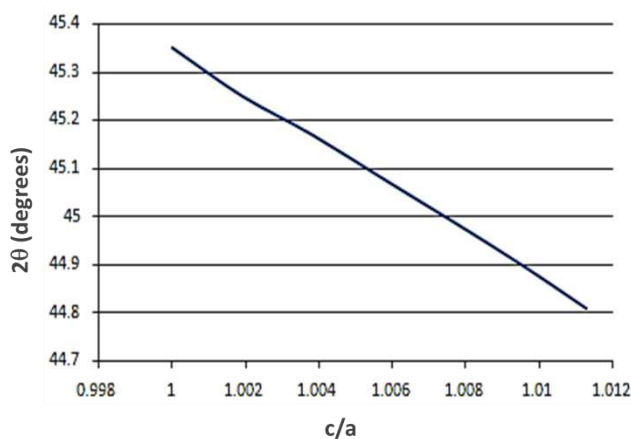
Figure 4.2. *Variation of 2θ according the c/a ratio value, based on the cubic lattice 3.996 Å, for the planes (002).*

For these reasons, in this work we will discuss how the structural phase of the $BaTiO_3$ is affected by the presence of the added Y_2O_3, following principally the observable changes in the peaks around 45°.

To remind the structural phase of the $BaTiO_3$ starting powders, the corresponding diffractograms are shown in Fig. 4.3. The three powders present a distinct splitting of (002) and (200) planes around 45°, related to a tetragonal phase identified by the JCPDS: 89-1428. These results are going to be the base over which the structural analysis of the samples is going to be developed.
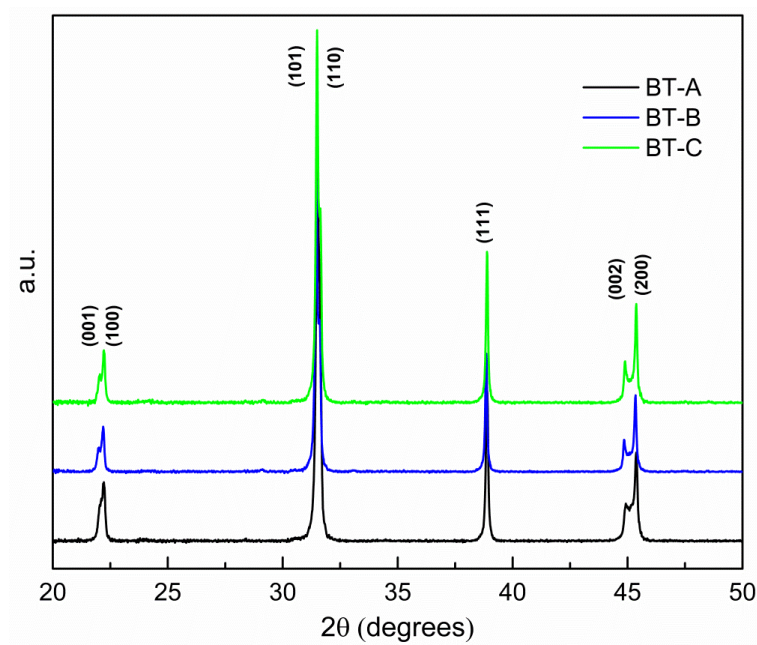
Figure 4.3. X-ray diffraction patterns of raw BaTiO₃ powders. JCPDS: 89-1428.

X-ray diffraction patterns corresponding to the thermally treated powders are presented in Fig. 4.4. The BT-A powders (Fig. 4.4.a) with Y_2O_3 content ranging from 0 to 20 wt% have a tetragonal crystalline structure, characterized by the two peaks around 45° which belong to the (002) and (200) planes. These two peaks are clearer seen in the enlargement made to this zone and shown in the Fig. 4.5.a. Thus, structurally the doped TT powders have no differences with respect to the undoped one. However, in the diffraction patterns of the thermally treated BT-A_5 and BT-A_20 (Fig. 4.4.a), is

possible to observe peaks corresponding to Y_2O_3 phase (JCPDS 89-5591) indicating that the solubility limit was surpassed.

On the other hand, the XRD patterns corresponding to the BT-B powders (Fig. 4.4.b) show more changes when Y_2O_3 concentration increases. In this case, we remind that the raw material already contains about 1.05 wt% of Y_2O_3. The pattern of powder BT-B_1 indicates a pure tetragonal phase, whereas those of powders containing more Y_2O_3 (2.5 wt% to 20 wt%) evidence a decrease of the tetragonality. In the Fig. 4.5.b can be observed with more detail the way in which the peaks around 45° look different with respect to the BT-B_1, being like joined. This might be related to a inhomogeneous distribution of the dopant in the BT matrix, which will lead to the presence of different c/a ratios in the samples; i.e. a mixture of tetragonal structures. Contrary to the BT-A samples, the Y_2O_3 phase is detected only for the BT-B_20 powder. Moreover, in the diffraction pattern of this sample, three additional peaks are detected between $2\theta \approx 29.5 - 30°$. They correspond to a secondary phase identified as $Ba_6Ti_{17}O_{40}$ (JCPDS 35-0817). This orthotitanate has been reported previously in different works such as the ones by Lu et al. (1990), Belous et al. (2008), and Paredes-Olguín et al. (2013). Since the BT-B matrix contains additives and dopants, it can be expected that they interact not only with the $BaTiO_3$ but also among them, and if an excess of ions is produced as a consequence, then some precipitates can get formed. In this case, it can be said that the incorporation of Y^{3+} atoms in the $BaTiO_3$ lattice leaded to a segregation of Ti^{4+}, being possible a a reaction between $BaTiO_3$ and TiO_2 producing the Ti-rich phase (Yuan, Zhang, & Li, 2004). Thus, the interaction between the doped matrix and the additives, under our experimental conditions, leaded to the precipitation of $Ba_6Ti_{17}O_{40}$.
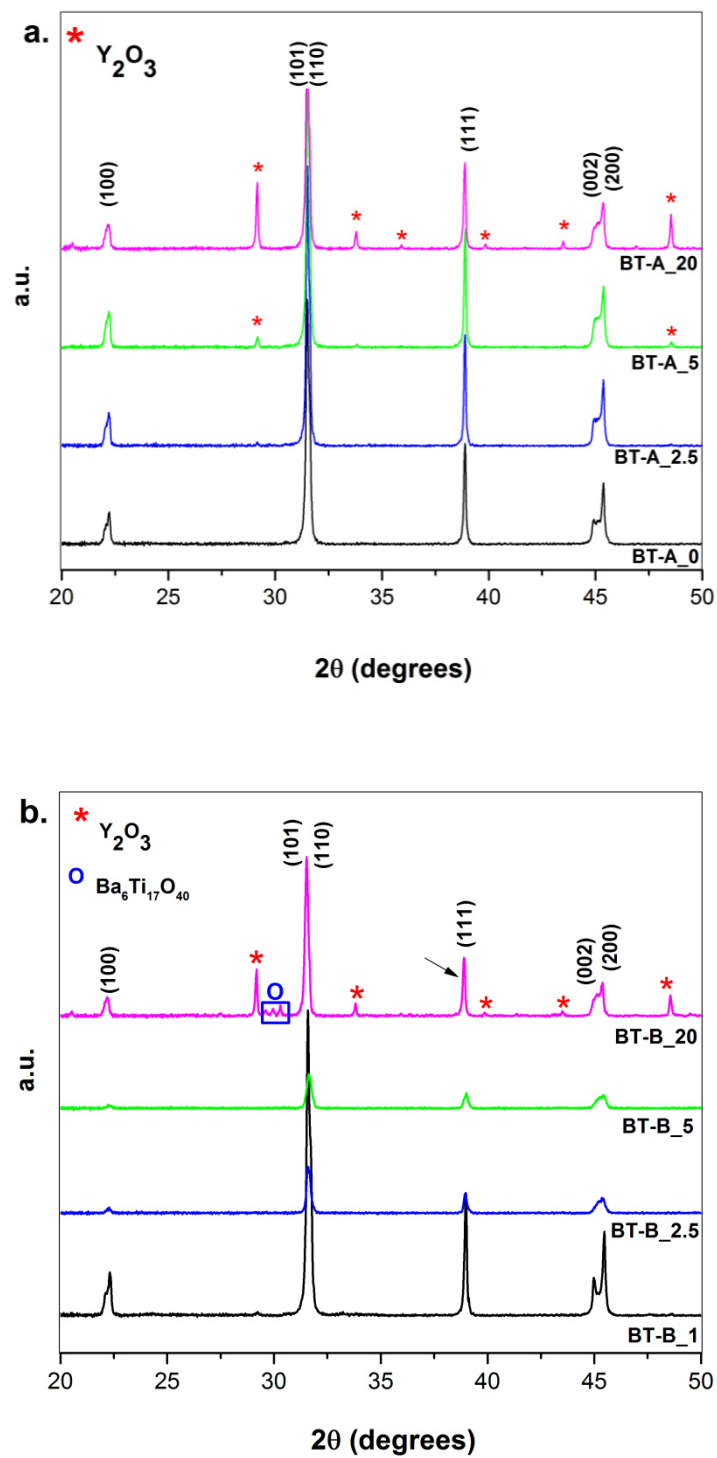
Figure 4.4. *X-ray diffraction patterns of thermally treated (1350 °C) undoped BaTiO$_3$ and Y$_2$O$_3$-doped BaTiO$_3$ (2.5, 5.0 and 20.0 wt%) powders. Powders issued from (**a**) BT-A and (**b**) BT-B.*
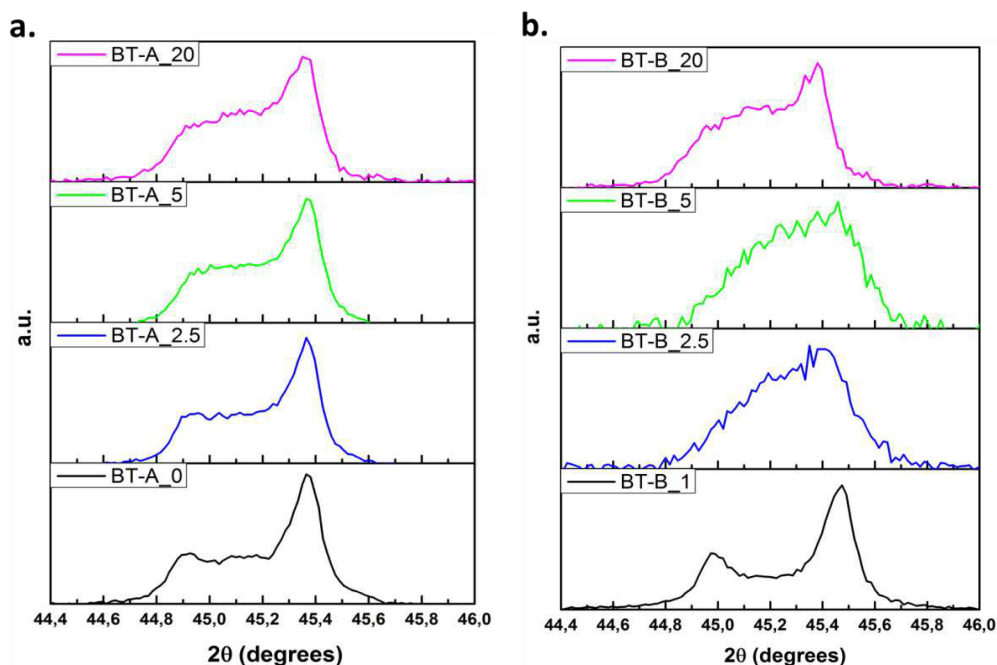
Figure 4.5. *Enlargement in the zone around 45° for X-ray diffraction patterns of thermally treated (1350 °C) undoped BaTiO₃ and Y₂O₃-doped BaTiO₃ (2.5, 5.0 and 20.0 wt%) powders.*

4.3. BaTiO₃ ceramics characterization

The sintering of ceramics (powder compacted at 300 MPa) was carried out both, in air and reducing atmosphere following two different thermal cycles:

1) In air, two temperature steps: 1310 °C then 1150 °C for 15 h. The ceramics sintered using this program are BT-A (A_0, A_2.5, A_5) and BT-B (B_1, B_2.5, B_5).

2) In reducing atmosphere ($pO_2 \approx 10^{-8} – 10^{-11}$ atm, N_2, H_2O, H_2): 1310 °C for 3 h (this sintering process was carried out in industrial conditions (KEMET de México), simulating the production conditions of the MLCCs). The ceramics sintered using this program are BT-A (A_0, A_1.5, A_2, A_2.5, A_5, A_20), BT-B (B_1, B_1.5, B_2, B_2.5, B_5, B_20), and BT-C (C_1, C_1.5, C_2).

4.3.1. BaTiO₃ ceramics sintered in air

- **Density**

The density values of the BT-A and BT-B ceramics obtained under these sintering conditions are summarized in Table 4.4. It is possible to see that the high-level of Y_2O_3 affected the densification decreasing it with respect to the undoped samples. Nevertheless, as observed in Fig. 4.6, the density for BT-A undoped ceramic is higher than the one of the ceramics doped with 2.5 and 5 wt% Y_2O_3, although for these was quite equal. For the BT-B ceramics, the density values are different among them, being as well lower when the content of Y_2O_3 increases. Even when the densification for both cases (BT-A and BT-B) is lower according to the Y_2O_3 content, the ceramics formed from the BT-B powder present higher density values. This difference can be due to the additives present in the BT-B powder formulation, since one of the purposes for include them into the formulation is to improve the densification of the ceramic material.

Table 4.4. *Density of the ceramics sintered in air, two temperature steps: 1310 °C then 1150 °C for 15 h.*

BaTiO₃ raw material	[Y_2O_3] (wt%)	Sample ID	Density (g/cm³)
BT-A (reagent-grade)	0	BT-A_0	5.62 ± 0.19
	2.5	BT-A_2.5	3.66 ± 0.03
	5	BT-A_5	3.67 ± 0.02
BT-B (commercially formulated)	1	BT-B_1	5.79 ± 0.07
	2.5	BT-B_2.5	4.82 ± 0.03
	5	BT-B_5	4.37 ± 0.02
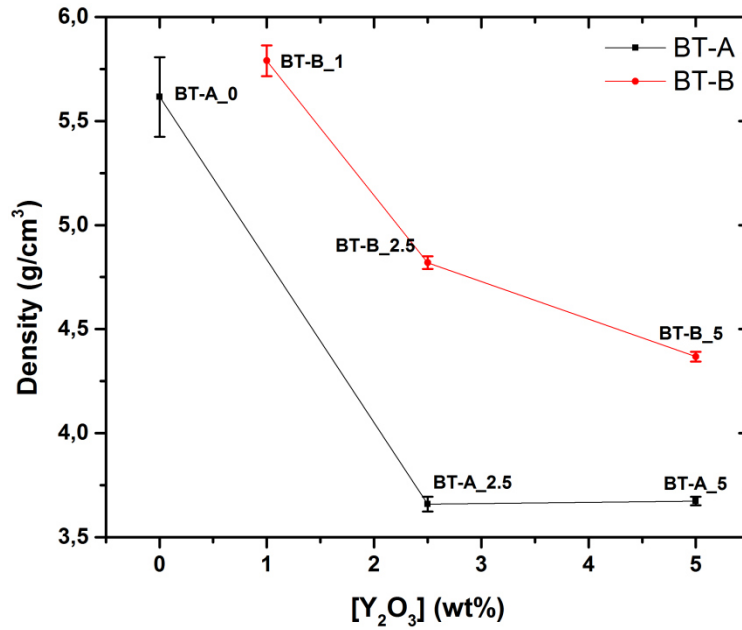
Figure 4.6. *Density of the ceramics sintered in air as a function of Y_2O_3 concentration.*

- **Grain morphology and grain size**

The SEM images of the BT-A_2.5 and BT-A_5 ceramics sintered in air are shown in Fig. 4.7. The mean grain sizes of this ceramics are 0.42 μm (Fig. 4.7.a) and 0.45 μm (Fig. 4.7.b), respectively as seen in Fig. 4.8 where the mean size distribution of both samples is shown. In both micrographs (Fig. 4.7), is possible to see grains with rounded morphology. Although some of them show signs of sintering, they are not really joined as in a dense ceramic. Indeed, the densification of the ceramics was not completed as reflected in the density values (Table 4.4), which could be caused by the high amount of Y_2O_3. Despite this fact, the grains present a homogeneous appearance. About the grain size, the difference among both ceramics is minimum, thus the doping level did not affect it.
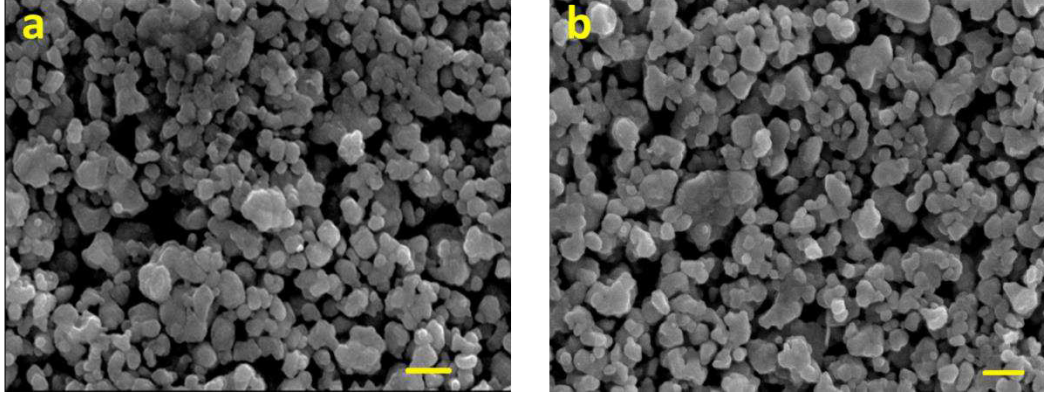
Figure 4.7. *SEM images from (a) BT-A_2.5 and (b) BT-A_5 ceramics sintered in air. Scale bar: 1μm.*

$$\bar{x} = 0.42 \pm 0.16 \, \mu m \qquad \bar{x} = 0.45 \pm 0.20 \, \mu m$$
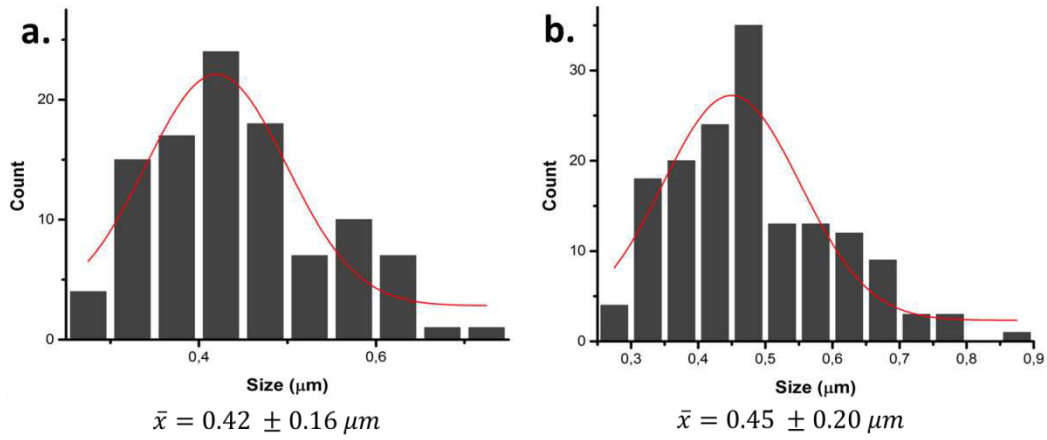
Figure 4.8. *Size distribution of (**a**) BT-A_2.5 and (**b**) BT-A_5 ceramics sintered in air.*

The Fig. 4.9.a and Fig. 4.9.b show the SEM images obtained from the BT-B_1 and BT-B_2.5 ceramics sintered in air. The mean grain sizes are 0.44 μm (Fig. 4.10.a) and 0.45 μm (Fig. 4.10.b). The grains have rounded appearance and they are homogeneously distributed. Comparing these ceramics with the ones from BT-A showed in Fig. 4.7, is recognizable that the space among the grains of these BT-B ceramics is lower than the observed in the BT-A micrographs. This is in agreement with higher densification.
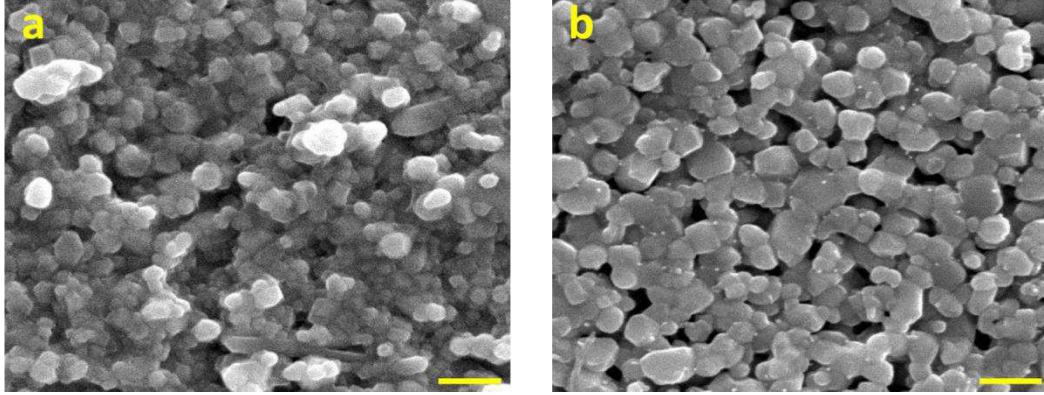
Figure 4.9. *SEM images from (**a**) BT-B_1 and (**b**) BT-B_5 ceramics sintered in air. Scale bar: 1μm.*

$$\bar{x} = 0.45 \pm 0.21 \; \mu m \qquad\qquad \bar{x} = 0.45 \pm 0.20 \; \mu m$$
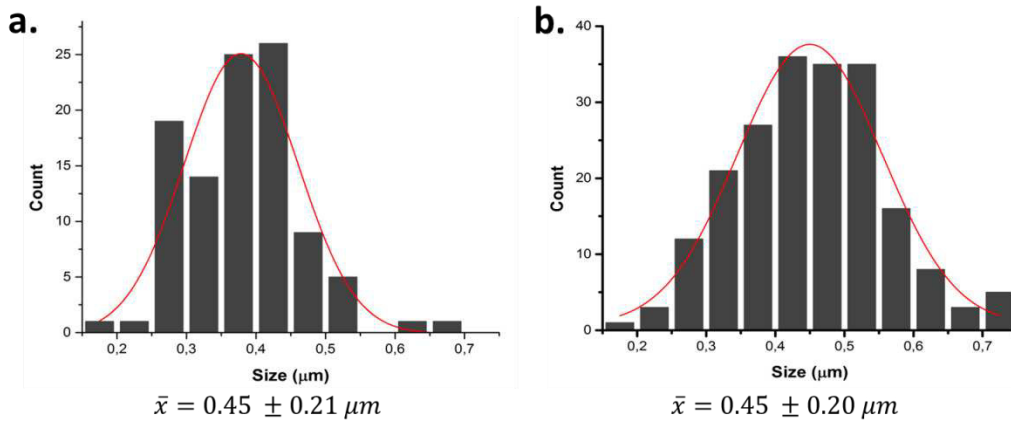
Figure 4.10. *Mean size distribution of (**a**) BT-B_1 and (**b**) BT-B_5 ceramics sintered in air.*

- **Structure and phase composition**

Fig. 4.11 shows the X-ray diffraction patterns of the air-sintered ceramics. The patterns from the ceramics formed from BT-A powders are shown in Fig. 4.11.a.

The BT-A ceramics crystallize in a tetragonal phase, as observed in the Fig. 4.11.a. The BT-A_2.5 and BT-A_5 ceramics however present a decrease of its tetragonality. Y_2O_3 phase is present in BT-A_5 ceramic, this phase was also observed on the BT-A_5 thermally treated powder (Fig. 4.4.a).

The diffraction patterns of ceramics formed from BT-B powder are shown in Fig. 4.11.b. These patterns are in agreeing with a $BaTiO_3$ perovskite and do not show secondary phases. However, it

can be seen the peaks corresponding to the (002) and (200) planes have changed according the dopant level. This can be a reflection of a chemically inhomogeneous composition of the ceramics. This results in the presence of various c/a ratios, which in turn affects the intensity and form of the peaks as well as the splitting of them.

Comparing the XRD patterns of doped ceramics (BT-A_2.5, BT-A_5, BT-B_2.5, and BT-B_5) it is possible to see that the influence of the Y^{3+} over the $BaTiO_3$ structure is greater in the case of the BT-B ceramics. If the peak splitting at 45° - which evidences a tetragonal phase – of both groups of ceramics is compared then it is possible to see that the ones from the BT-B doped ceramics look more joined, being almost like if there was just one broaden peak. It can be considered that the dopant effect on these samples lattices is stronger. This behavior points out the strong interaction between additives and dopants present in the BT-B, which was also reflected in the density values as well as on the microstructure of these ceramics.
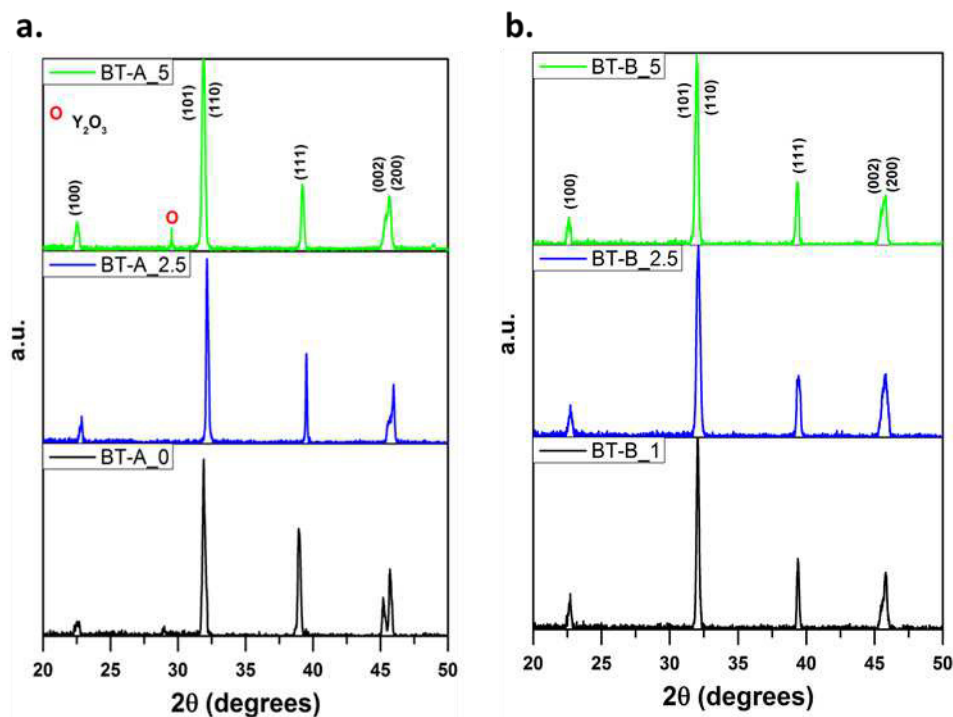
Figure 4.11. *X-ray diffraction patterns of undoped $BaTiO_3$ and 2.5 and 5.0 wt% Y_2O_3-doped $BaTiO_3$ ceramics. Ceramics formed from (**a**) BT-A and (**b**) BT-B, sintered in air.*

A summary of the observations for the thermally treated powders and sintered ceramics in air is shown in Table 4.5.

Table 4.5. Secondary phases detected in the different powders and ceramics thermally treated and sintered in air, two temperature steps: 1310 °C then 1150 °C 15 h.

BaTiO₃ raw material	Y₂O₃ wt%	Sample ID	Secondary phase	
			Powder (TT)	Ceramic
BT-A (reagent-grade)	0	BT-A_0	x	x
	2.5	BT-A_2.5	x	x
	5	BT-A_5	Y_2O_3	Y_2O_3
	20	BT-A_20	Y_2O_3	x
BT-B (commercially formulated)	1	BT-B_1	x	x
	2.5	BT-B_2.5	x	x
	5	BT-B_5	x	x
	20	BT-B_20	$Ba_6Ti_{17}O_{40}$ and Y_2O_3	x

x: no secondary phases were detected. BT-A_20 and BT-B_20 ceramics were not sintered under these conditions.

4.3.2. BaTiO₃ ceramics sintered in reducing atmosphere

Ceramics from BT-A, BT-B and BT-C powders were sintered at 1310 °C during 3h, in a reducing atmosphere, and then underwent a re-oxidizing process. The ceramics sintered under this protocol were BT-A (A_0, A_1.5, A_2, A_2.5, A_5, A_20), BT-B (B_1, B_1.5, B_2, B_2.5, B_5, B_20), and BT-C (C_1, C_1.5, C_2).

With the purpose to detect differences among sintering steps (sintering in reducing atmosphere and re-oxidizing under a weekly oxidizing atmosphere), ceramics from each group were separated to perform analyses to both conditions, denominating them as "sint" and "reox" respectively. SEM analyses of some of the ceramics were also performed. In order to follow the dopant behavior into

the BT-lattice, and detect any structural change during the different treatments, the main tool used in this work is the X-Ray Diffraction analysis.

4.3.2.1. BaTiO₃ ceramics issued from BT-A powders with Y₂O₃ content from 0 to 20 wt%.

- **Density**

The effect of the dopant level was also observed under these sintering conditions. In the Table 4.6 are given the density values of BT-A ceramics, as well as in the Fig. 4.12. The densification for doped ceramics is lower and the values do not change significantly among the doped ceramics. With these ceramics, the effect of the Y_2O_3 content over their densification is noticeable, finding values between 60 – 75 % for the doped ceramics.

Table 4.6. Density of BT-A ceramics sintered under reducing atmosphere and 1310 °C.

BaTiO₃ raw material	[Y₂O₃] (wt%)	Sample ID	Density (g/cm³)
BT-A (reagent grade)	0	BT-A_0	5.70 ± 0.05
	1	BT-A_1	4.51 ± 0.17
	1.5	BT-A_1.5	3.74 ± 0.04
	2	BT-A_2	3.74 ± 0.06
	2.5	BT-A_2.5	4.09 ± 0.09
	5	BT-A_5	4.29 ± 0.05
	20	BT-A_20	4.19 ± 0.06
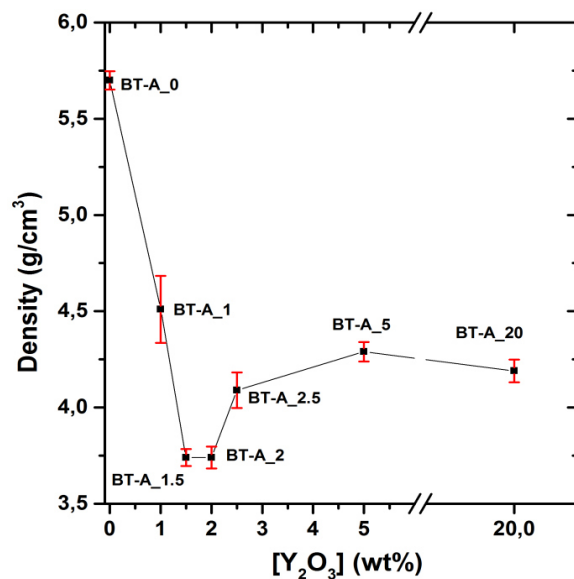
Figure 4.12. *Density of BT-A ceramics sintered in a reducing atmosphere as a function of Y_2O_3 content.*

Regarding the possible differences between the density of the ceramics with same dopant level sintered in air and the ones sintered in a reducing atmosphere, in Fig. 4.13 is shown a comparison of the values. For the ceramics BT-A_0, BT-A_2.5, and BT-A_5 sintered under reducing atmosphere the density is higher than the one obtained when sintered in air. The density of the undoped ceramics is about the same under both sintering processes. Meanwhile, the BT-A_2.5 and BT-A_2.5 ceramics sintered in reducing conditions are 7% and 10% denser than the ones sintered in air.
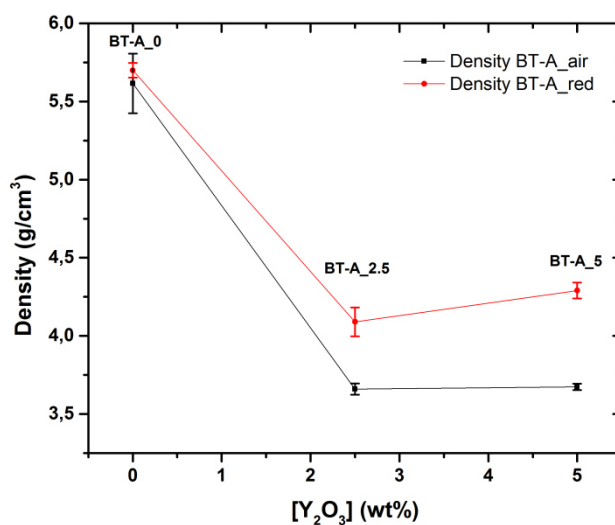
Figure 4.13. *Comparison of the BT-A ceramics density sintered using air or reducing atmosphere as a function of Y_2O_3 content.*

- **Grain morphology and grain size**

In the Fig. 4.14 the SEM analyses performed to BT-A ceramics doped with 5 and 20 wt% Y_2O_3 are shown. In this case, the Fig. 4.14.a correspond to the BT-A_5 ceramic that was taken out before the re-oxidizing step (BT-A_5_sint) and the Fig. 4.14.b to the one that passed through it (BT-A_5_reox). The mean grain size distribution of these ceramics is 0.43 μm and 0.41 μm, respectively. It means that apparently the size is not affected by the re-oxidizing step. Neither is the morphology, since their outward appearance is similar, the grains have angular borders and a smooth surface. The BT-A_20_sint ceramic, shown in Fig. 4.14.c has a mean grain size of 0.44 μm, which is pretty close to the BT-A_5 ceramics. About the morphology of this sample, the image (Fig. 4.14.c) allows seeing more angular-bordered grains.
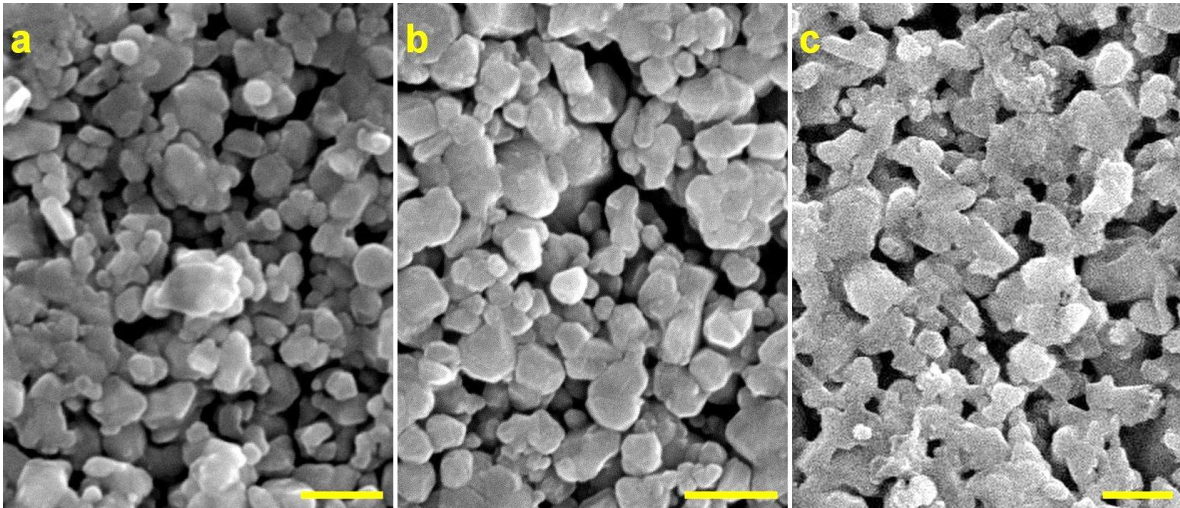
Figure 4.14. SEM images from BT-A ceramics sintered in reducing atmosphere. (a) BT-A_5_sint, (b) BT-A_5_reox, and (c) BT-A_20_sint. Scale bar: 1μm.

$$\bar{x} = 0.41 \pm 0.21 \, \mu m \qquad\qquad \bar{x} = 0.43 \pm 0.16 \, \mu m$$

$$\bar{x} = 0.44 \pm 0.29 \, \mu m$$
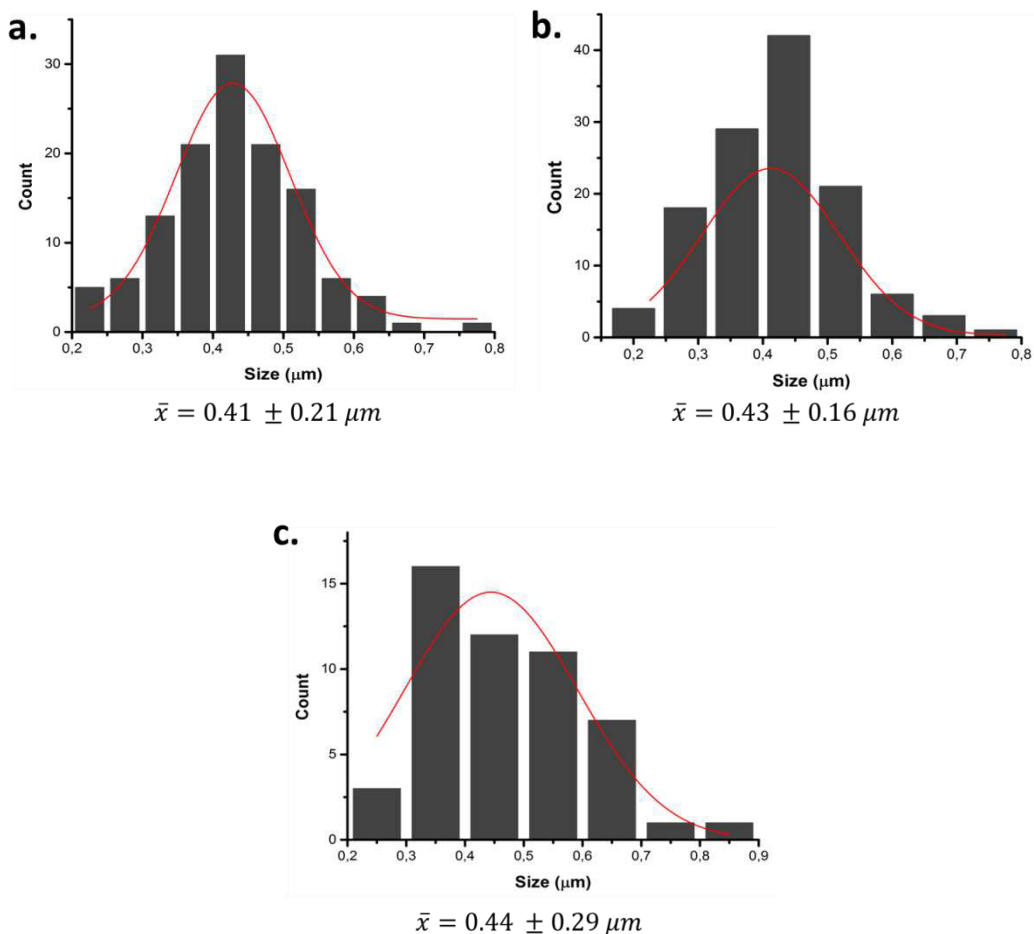
*Figure 4.15. Size distribution of BT-A ceramics sintered in reducing atmosphere. (**a**) BT-A_5_sint, (**b**) BT-A_5_reox, and (**c**) BT-A_20_sint.*

- **Structure and phase composition**

The XRD patterns of undoped and doped ceramics, sintered and re-oxidized, formed from the BT-A powders are shown in Fig. 4.16. Diffractograms from BT-A undoped ceramics are shown in Fig. 4.16.a, and from 1 wt% Y_2O_3-doped BT-A ceramics in Fig. 4.16.b. In both figures, a tetragonal perovskite structure (JCPDS: 89-1428) is observed in all cases. No traces of secondary phases can be detected, either in Fig. 4.16.a or Fig. 4.16.b. There is no structural evolution from the powder to the final dense ceramics or differences among the sintered and re-oxidized ceramics.

In the case of the 1.5 and 2 wt% Y_2O_3-doped BT-A ceramics (Fig. 4.16.c and Fig. 4.16.d), it is possible to say that the main phase remains tetragonal. The peaks corresponding to the planes (002) and (200) get closer to each other when Y_2O_3 concentration is 1.5 wt%, as seen in Fig. 4.16.c. It indicates a decrease in the tetragonality of the BT lattice. For samples with Y_2O_3 concentration higher than 1.5 wt% (Fig. 4.16.d to 4.16.g) those peaks get even more joined, i.e. when the dopant concentration increases, the tetragonality of the samples is decreased. For the 5 and 20 wt% Y_2O_3-doped BT-A ceramics (Fig. 4.16.f and Fig. 4.16.g), it could be even said that they seem merged, because the decrease of intensity and apparent lack of split. The change in the crystalline phase results from the Y^{3+} ions incorporation into the BT lattice (Kim et al., 2008; Wang et al., 2014a; Wang et al., 2014b). However, the incorporation of dopants results in a non-homogeneous distribution of these in the BT matrix during the sintering process. With the obtained patterns it is not possible to discriminate the c/a ratios corresponding to the range of 2θ that lead to the broadening of the peaks. Despite the changes in the lattice, the position of the BT planes was not shifted.

Moreover, in Fig. 4.16.d an additional peak at 2θ = 30.6° is noticed both, sintered and reoxidized ceramics, which corresponds to the cubic pyrochlore compound $Y_2Ti_2O_7$ (JCPDS: 42-0413). This compound has also been evidenced before by other authors like Belous et al. (2008), Yoon et al. (2007), and Zhang et al. (2016). The diffractograms of the 2.5 wt% Y_2O_3-doped BT-A ceramics (Fig 4.16.e.) also reveal the presence of a secondary phase. A peak of weak intensity at 29.5° is detected and identified as the yttrium titanate Y_2TiO_5 (JCPDS: 40-0795) phase. The BT-A_5 ceramics (Fig 4.16.f.) present peaks that correspond to the phases Y_2O_3 and $Y_2Ti_2O_7$.

Finally, the XRD analyses of the BT-A_20 ceramics (Fig. 4.16.g) revealed the presence of secondary phases as well. Nonetheless, there are some differences among the BT-A_20_sint and BT-A_20_reox patterns. In the BT-A_20_sint diffraction pattern, peaks corresponding to Y_2TiO_5 and $Y_2Ti_2O_7$ are observed. On the other hand, the BT-A_20_reox presents the $Y_2Ti_2O_7$ along with

Y_2O_3. The differences found between the reduced and re-oxidized ceramics with respect to their secondary phases can be due to the formation of some Ti^{4+} to Ti^{3+} during the sintering and with the post-sintering annealing process it is reverted, leaving less available to form secondary phases. Also, the lattice distortion and the formation of additional phases are related with the incorporation of Y^{3+} ions into the BT-lattice. Since the Y^{3+} ion has an intermediate size between Ba^{2+} and Ti^{4+} ions, it can occupy either A- or B-site in the BT crystal structure. In principle, Y^{3+} will replace first Ba^{2+} sites, but then if the activity increases on this site, it also replaces Ti^{4+} ions, which could have contributed to the formation of Ti-rich precipitates. Another factor that could lead to the formation of these secondary phases is that the solubility limit of Y_2O_3 in BT has been reached.

127
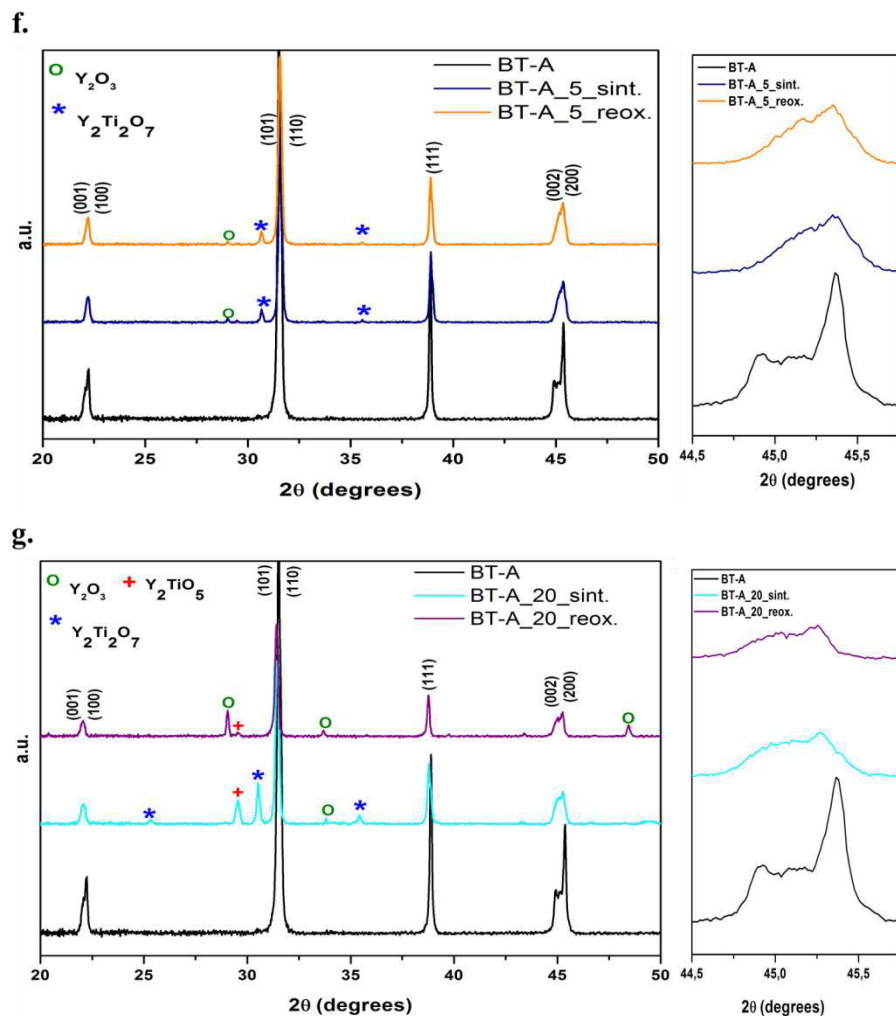
c.

d.

e.

128
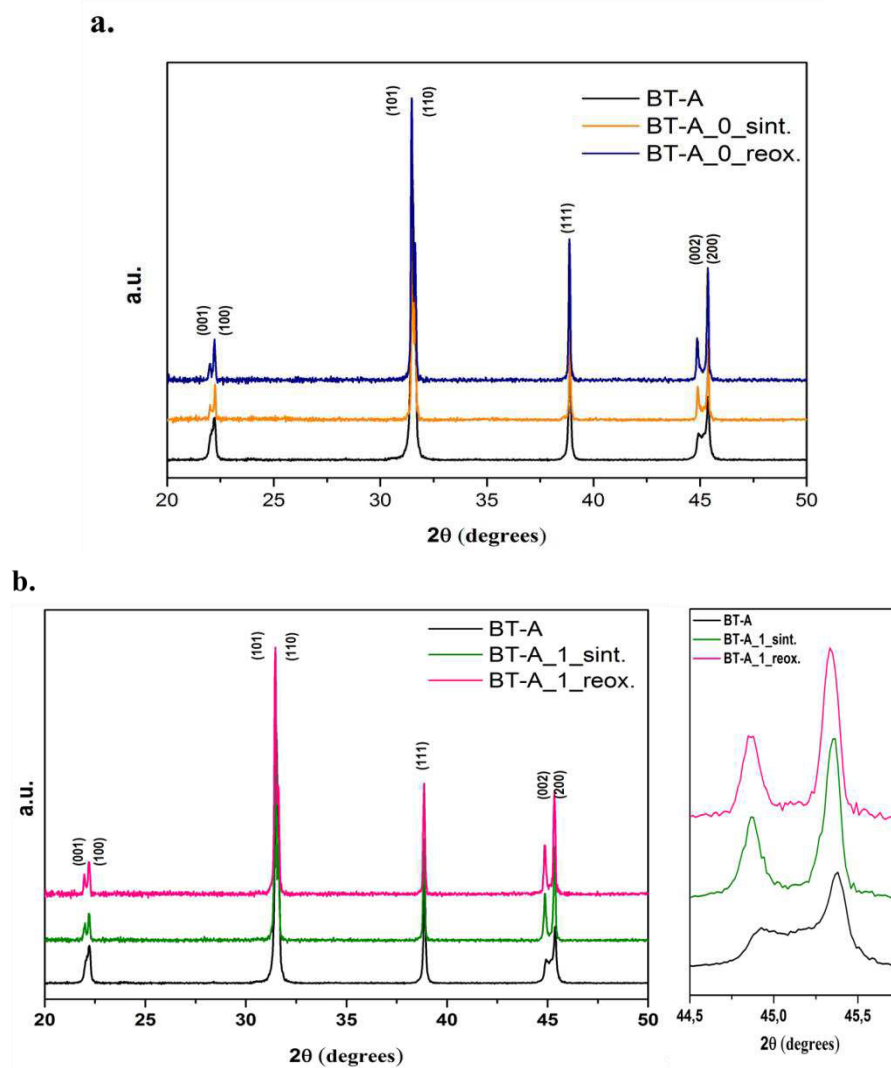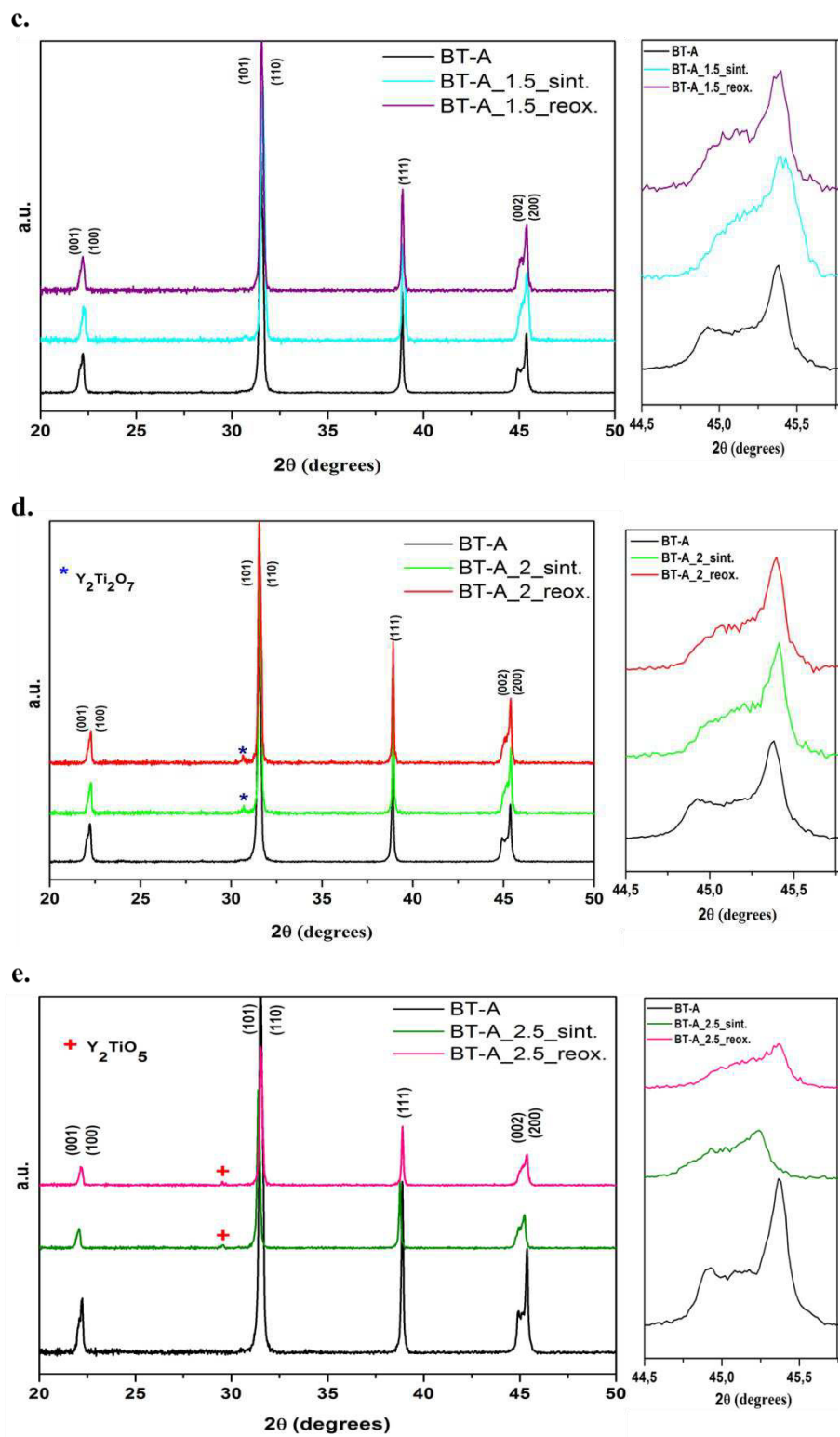
Figure 4.16. *XRD patterns of BT-A powder and ceramics sintered in reducing atmosphere and re-oxidized. Lateral enlargements of zone around 45° are presented for doped samples.*

A summary of the principal observations from the XRD analyses performed on BT-A ceramics sintered in reducing conditions is presented in Table 4.7.

Table 4.7. *Secondary phases detected in BT-A ceramics sintered in reducing atmosphere at 1310 °C.*

BaTiO$_3$ raw material	Y$_2$O$_3$ wt%	Sample ID	Secondary phases
BT-A (reagent-grade)	0	BT-A_0	x
	1	BT-A_1	x
	1.5	BT-A_1.5	x
	2	BT-A_2	Y$_2$Ti$_2$O$_7$
	2.5	BT-A_2.5	Y$_2$TiO$_5$
	5	BT-A_5	Y$_2$O$_3$; Y$_2$Ti$_2$O$_7$
	20	BT-A_20	sint. ceramic: Y$_2$O$_3$; Y$_2$Ti$_2$O$_7$; Y$_2$TiO$_5$. reox. ceramic: Y$_2$O$_3$; Y$_2$TiO$_5$.

x: no secondary phases were detected.

4.3.2.2. BaTiO$_3$ ceramics issued from BT-B powders with Y$_2$O$_3$ content from 1 to 20 wt%.

- **Density**

The density of the ceramics produced from the BT-B formulated powder, is shown in the Table 4.8. The density increases slightly when BT-B ceramics are doped with 1.5 and 2 wt% of Y$_2$O$_3$, then from 2.5 up to 20 wt% it decreases rapidly. The variation of density with Y$_2$O$_3$ content is plotted in Fig. 4.18, where it is seen that the density is clearly lower when Y$_2$O$_3$ level is higher than 2 wt%. The density values of BT-B ceramics (Table 4.8) are about 20% higher than the ones from the BT-A ceramics (Table 4.6). This was expected since the BT-B contains sintering additives that contribute to the improvement of the densification. In this case, the BT-B contains SiO$_2$ (0.30 wt%), which has been reported to contribute to the improvement of the densification process (Liu, & Roseman, 1999; Wu, Wang, McCauley, Chu, & Lu, 2007).

Table 4.8. Density of BT-B ceramics sintered in reducing atmosphere at 1310 °C.

BaTiO$_3$ raw material	[Y$_2$O$_3$] (wt%)	Sample ID	Density (g/cm^3)
BT-B (commercially formulated)	1	BT-B_1	5.45 ± 0.07
	1.5	BT-B_1.5	5.56 ± 0.04
	2	BT-B_2	5.59 ± 0.05
	2.5	BT-B_2.5	5.03 ± 0.10
	5	BT-B_5	4.97 ± 0.04
	20	BT-B_20	4.84 ± 0.10
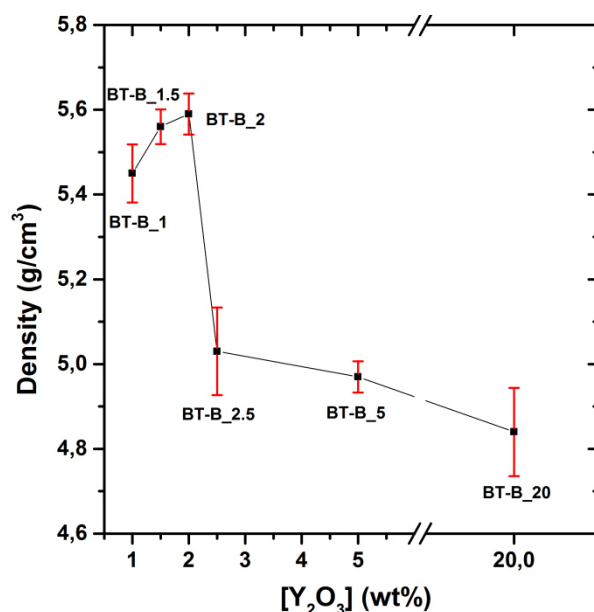
Figure 4.17. Density of BT-B ceramics sintered in a reducing atmosphere as a function of Y$_2$O$_3$ content.

A contrast between the density results obtained for the ceramics BT-B_1, BT-B_2.5, and BT-B_5 sintered under reducing atmosphere (Table 4.8) and the ones sintered in air (Table 4.6) is presented in the Fig. 4.18. This figure shows that the density of the ceramics sintered under the different atmospheres is different. For the BT-B_1 ceramics, the one sintered in air has higher density, but for the ceramics above this dopant level, the ones sintered in reducing conditions present higher

densities. The BT-B_1 fired in air is 6 % denser than the BT-B_1 fired in reducing atmosphere. While BT-B_2.5 and BT-B_5 sintered in air are about 3 % and 10 % respectively less dense than those sintered in reducing atmosphere.
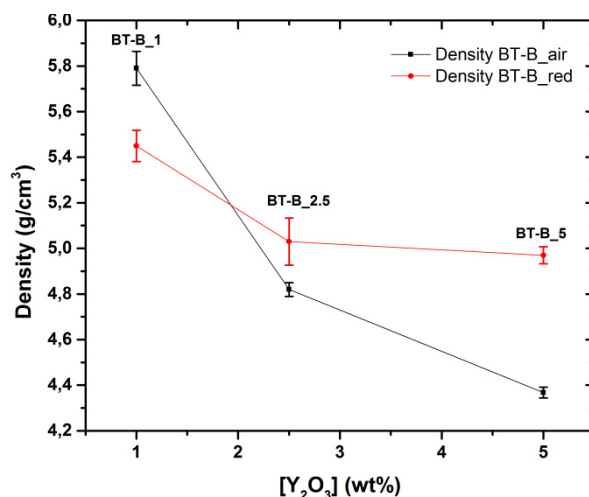
Figure 4.18. *Comparison of the BT-B ceramics density sintered using air or reducing atmosphere as a function of Y_2O_3 content.*

- **Grain morphology and grain size**

SEM images of BT-B doped-ceramics are shown in Fig. 4.19. In this case, the three analyzed ceramics have different Y_2O_3 concentration and are sintered, i.e. without the re-oxidation step. The mean grain distribution sizes can be observed in Fig. 4.20. It is roughly equal for the three samples. The value for BT-B_1.5_sint is 0.43 μm, 0.42 μm for BT-B_2_sint, and 0.41 μm for the BT-B_5_sint (Fig. 4.20). Thus, the grain size does not significantly change with the increase of Y_2O_3 content. Indeed, the morphology of the grains is similar between the three samples, i.e., the three of them present agglomerations of spherical grains and also some grains with a more angular-bordered form (Fig. 4.19).

Despite the differences in the density values of these three ceramics, the SEM images show that they have a similar morphology and surface.
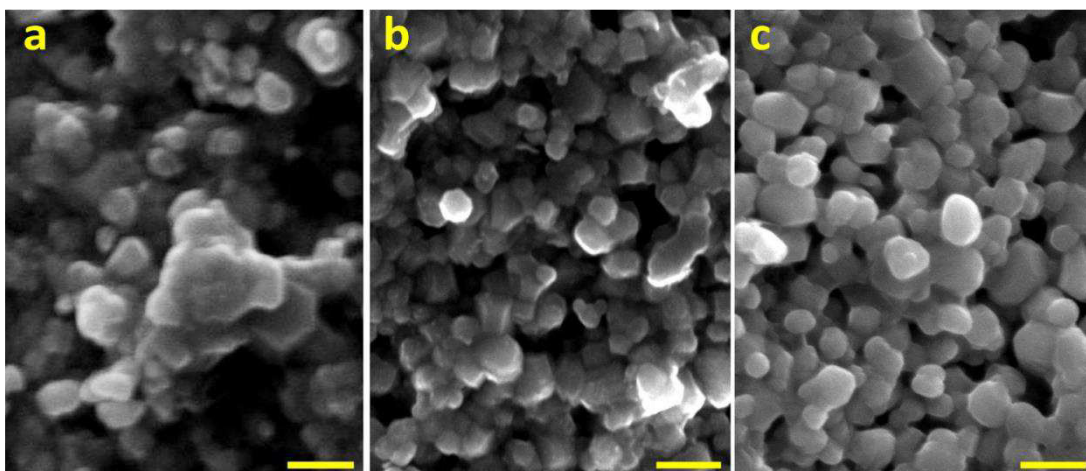
Figure 4.19. *SEM images from BT-B ceramics sintered in reducing atmosphere. (**a**) BT-B_1.5_sint, (**b**) BT-B_2_sint, and (**c**) BT-B_5_sint. Scale bar: 1 μm.*

$$\bar{x} = 0.43 \pm 0.20 \, \mu m$$

$$\bar{x} = 0.42 \pm 0.17 \, \mu m$$

$$\bar{x} = 0.41 \pm 0.11 \, \mu m$$

Figure 4.20. *Mean size distribution of BT-B ceramics sintered in reducing atmosphere. (**a**) BT-B_1.5_sint., (**b**) BT-B_2_sint., and (**c**) BT-B_5_sint.*

- **Structure and phase composition**
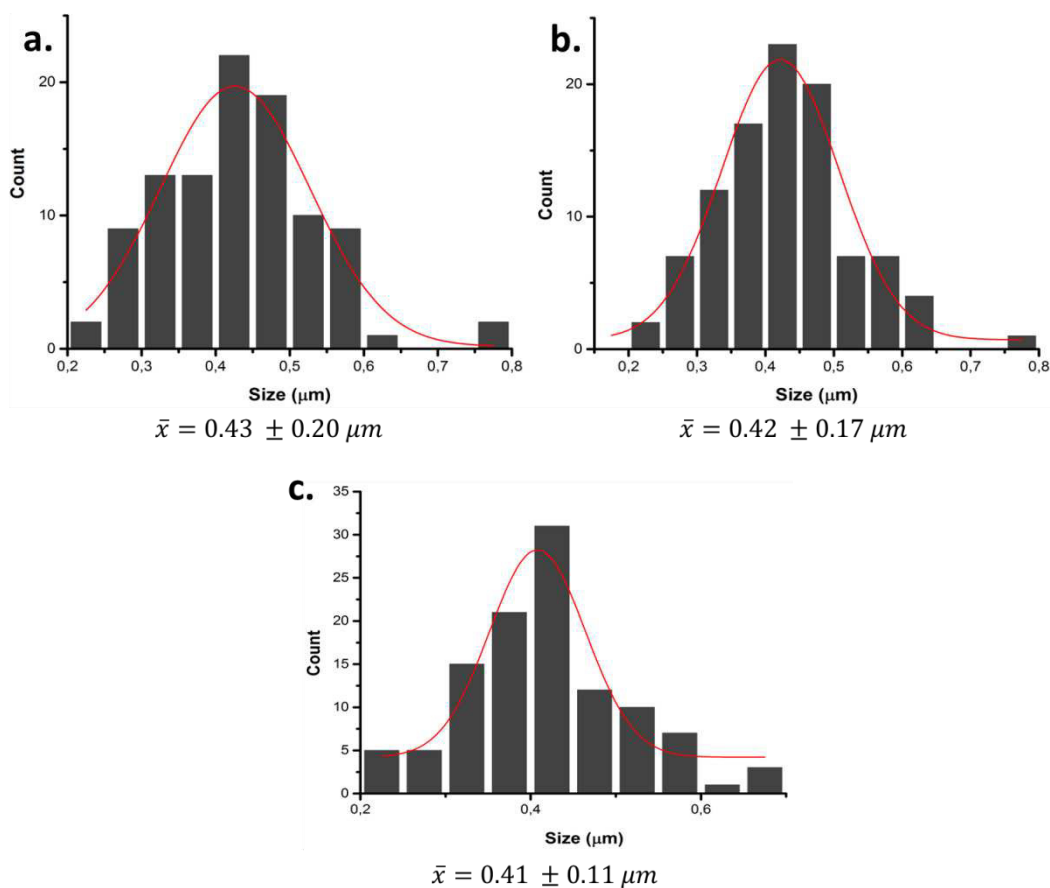
X-ray diffraction patterns corresponding to the ceramics prepared from powder BT-B doped with Y_2O_3 from 1 to 20 wt%, and sintered under industrial conditions are shown in Fig. 4.21.

As shown in Fig. 4.21.a for the lowest Y_2O_3 content (BT-B_1) there is no difference between the structure of the powder and sintered ceramics. The crystalline structure coincides with the tetragonal perovskite phase. All the ceramics with Y_2O_3 level from 1.5 wt% up to 20 wt% also crystallize in the tetragonal structure. The c/a ratio decreases affecting the tetragonality as seen in Fig. 4.21.b-f. The characteristic split of the planes (002) and (200) decreases with the increment of Y_2O_3 doping. The intensity of the peaks is also affected by the amount of Y_2O_3 they look almost like just one broaden peak.

These variations in the tetragonality can also be related with the secondary phases detected in the concerned ceramics. In the case of BT-B_1.5 and BT-B_2.0 (Fig. 4.21.b and 4.21.c), the $Y_2Ti_2O_7$ phase appears in the sintered ceramics and remains after the re-oxidation treatment. In the BT-B_2.5, the Y_2TiO_5 phase is detected in both, sintered and re-oxidized ceramics (Fig. 4.21.d). Finally, for the BT-B_5 and BT-B_20 ceramics, the $Ba_6Ti_{17}O_{40}$ phase was identified (Fig. 4.18.e and Fig. 4.18.f). Also, in the BT-B_20 ceramics, peaks corresponding to the Y_2O_3 phase are observed.

The precipitation of these different phases with respect to the Y_2O_3 concentration in the samples can be given by the interaction among the BT-B matrix and the additives and dopants it contains; i.e., the Y_2O_3 added to reach the specified doping concentrations.

In the case of the BT-B ceramics, it must be reminded that the raw powder contains a high content of Mg^{2+} (0.29 %), while the BT-A being reagent grade is considered practically Mg-free. The formulated powder BT-C has a ratio of Mg^{2+} of 0.0062 %. Since the Mg^{2+} can substitute Ti^{4+}-sites in the BT lattice (Wang et al., 2014a) it leads to the Ba-sites replacement by Y^{3+} until the saturation

in these sites is reached. Then the subsequent Y^{3+} added will enter into the Ti^{4+}-sites. The free Ti^{4+} in the system will increase the possibility of secondary phases rich in Ti^{4+} formation.

The BT-A and BT-B 20 wt% Y_2O_3-doped ceramics present different secondary phases. In BT-A_20 XRD patterns $Y_2Ti_2O_7$ and Y_2TiO_5 are observed (Fig. 4.16.g), while in the ones from BT-B_20 ceramics the $Ba_6Ti_{17}O_{40}$ and Y_2O_3 secondary phases were detected (Fig. 4.20.f). However, is seen that the higher the Y^{3+} dopant level, the higher is the possibility of Ti-rich phases formation.

The raw powder composition must be taken into account at the time of discuss these differences. Since chemical composition of the powders is different, the interactions of the Y_2O_3 dopant are not the same with both BT matrixes. As aforesaid, it is probable that the BT-B additives play a role on the final structural and microstructural ceramics properties.
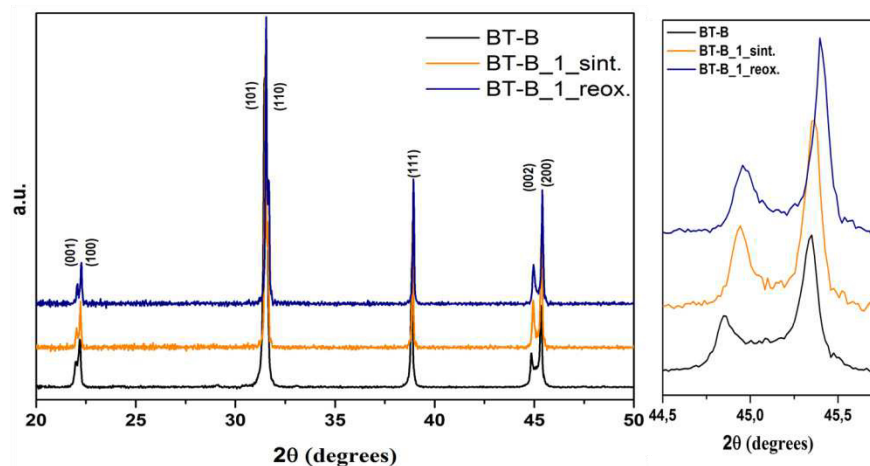
b.
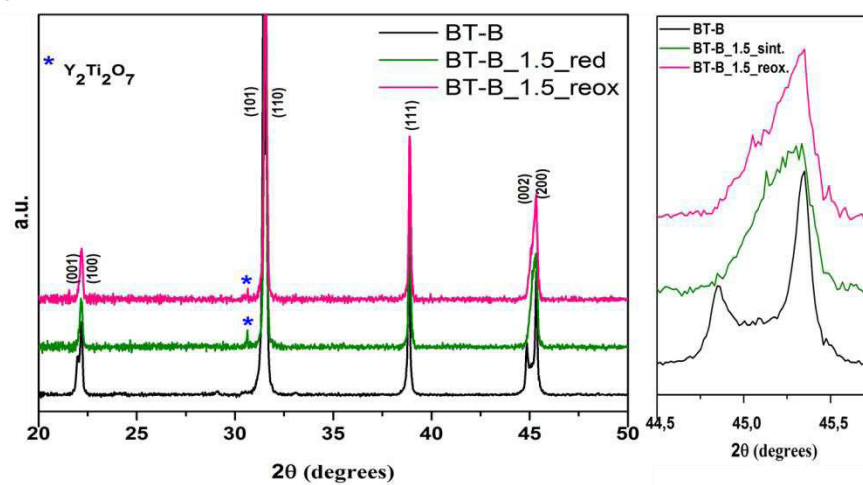
c.
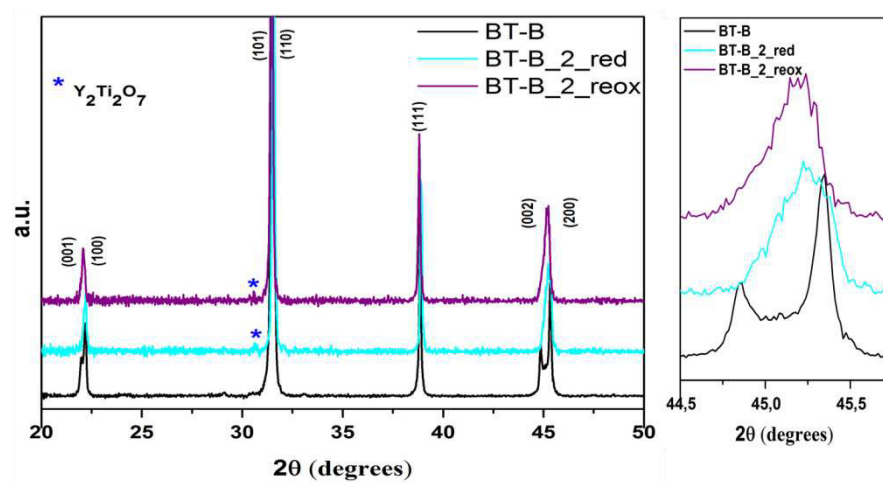
d.
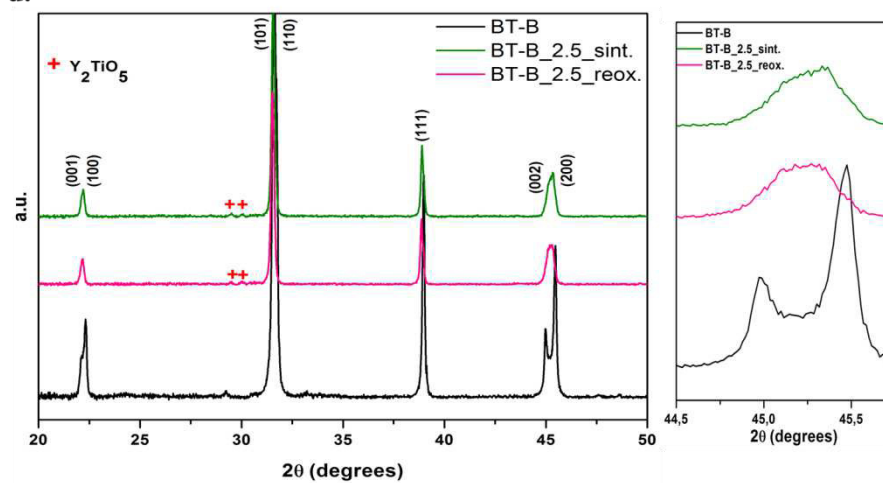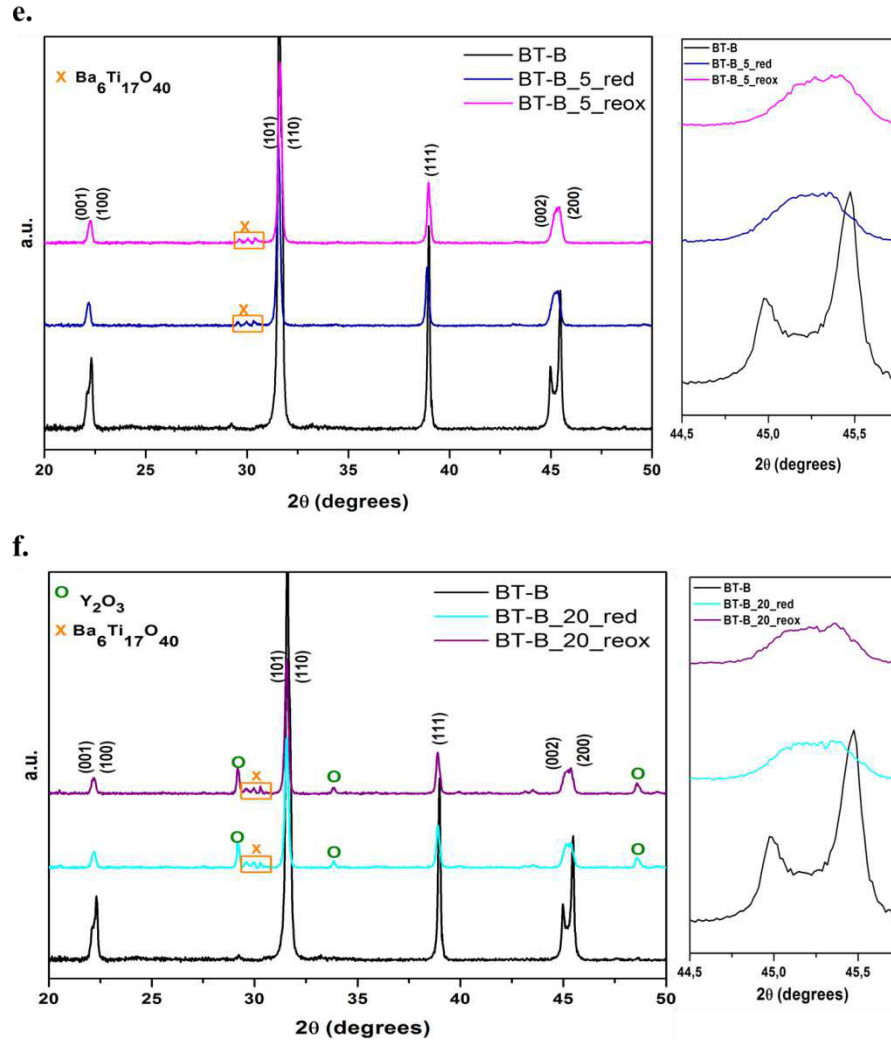
Figure 4.21. XRD patterns of BT-B powder and ceramics sintered in reducing atmosphere and re-oxidized. Lateral enlargements of zone around 45° are presented.

A summary of the principal observations from the XRD analyses performed on BT-B ceramics sintered in reducing conditions is presented in Table 4.9.

Table 4.9. *Secondary phases detected in BT-B ceramics sintered in reducing atmosphere at 1310 °C.*

BaTiO$_3$ raw material	Y$_2$O$_3$ wt%	Sample ID	Secondary phase
BT-B (commercially formulated)	1	BT-B_1	x
	1.5	BT-B_1.5	Y$_2$Ti$_2$O$_7$
	2	BT-B_2	Y$_2$Ti$_2$O$_7$
	2.5	BT-B_2.5	Y$_2$TiO$_5$
	5	BT-B_5	Ba$_6$Ti$_{17}$O$_{40}$
	20	BT-B_20	Y$_2$O$_3$; Ba$_6$Ti$_{17}$O$_{40}$

x: no secondary phases were detected.

4.3.2.3. BaTiO$_3$ ceramics issued from BT-C powders with Y$_2$O$_3$ content: 1 to 2 wt%.

- **Density**

These ceramics discussed in this section are formed from another formulated powder. The composition of BT-C is different from the BT-B (Table 4.1). The main differences attending to the interests of next discussions are on the amount of Ca, Si, and Mg present in these powders, which are higher in the BT-B. A reminder of the concentration of these components in the formulated powders is presented in Table 4.10.

Table 4.10. *Chemical composition of BaTiO$_3$ formulated powders.*

	Ba	Ti	Y	Ca	Si	Mg
BT_B	54.67	19.17	1.05	1.34	0.30	0.29
BT_C	53.86	18.85	1.05	0.57	0.17	0.006

Values are given in wt%.

The density values of BT-C ceramics are presented in the Table 4.11 and Fig. 4.22. The densification for these ceramics is above 90%. Although the marginally difference in the density, it was equal for BT-C_1.5 and BT-C_2, and lower for BT-C_1.

Comparing the density values of the BT-C and BT-B ceramics with the same Y_2O_3 concentration (BT-B_1, BT-B_1.5, and BT-B_2), is possible to see that they are quite similar, being the ones of BT-B ceramics just about 1 % lower. This means that despite the difference in the SiO_2 content (being the double for the BT-B powder) the densification was not improved or diminished by it. This leads to consider that is not just the SiO_2 which exerts an effect over the densification of BT-doped ceramics, but also the rest of additives present in the BT-formulated powders composition.

Table 4.11. *Density of BT-C ceramics sintered in reducing atmosphere at 1310 °C.*

BaTiO$_3$ raw material	[Y$_2$O$_3$] (wt%)	Sample ID	Density (g/cm^3)
BT-C (commercially formulated)	1	BT-C_1	5.48 $\pm$ 0.05
	1.5	BT-C_1.5	5.60 $\pm$ 0.05
	2	BT-C_2	5.60 $\pm$ 0.04
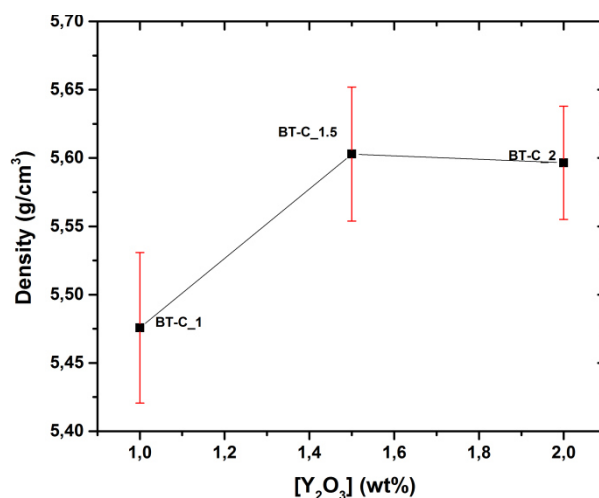
Figure 4.22. *Density of BT-C ceramics sintered in a reducing atmosphere as a function of Y$_2$O$_3$ content.*

- **Grain morphology and grain size**

SEM images of the ceramics formed with BT-C powder doped with 1.5 and 2 wt% Y_2O_3 are shown in Fig. 4.23.a and 4.23.b, respectively. The size distribution of these samples is shown in Fig. 4.23. Their mean grain sizes are 0.46 and 0.48 μm. The yttrium oxide content does not seem to affect the morphology or the grain size. Merged grains with angular borders are observed and no porosity is visible. Ceramics prepared from BT-C are definitively more densified than the ones with the same Y^{3+} content issued from BT-B powders.

With respect to the mean size of BT-C_1.5_sint and BT-C_2_sint (Fig. 4.24) compared with the BT-B_1-5_sint and BT-B_2_sint (Fig. 4.19), the difference among them is hardly noticeable regarding the obtained values and the respective incertitude.
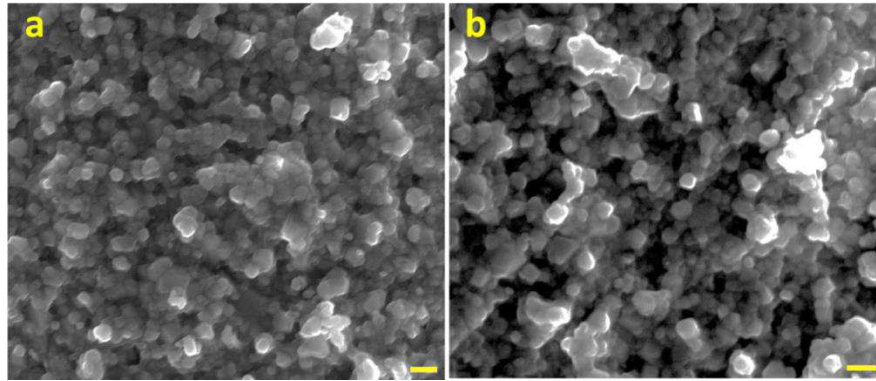
*Figure 4.23. SEM images from BT-C ceramics sintered in reducing atmosphere. (**a**) BT-C_1.5_sint, (**b**) BT-B_2_sint. Scale bar: 1 μm.*

$\bar{x} = 0.46 \pm 0.18\ \mu m$ $\bar{x} = 0.48 \pm 0.19\ \mu m$
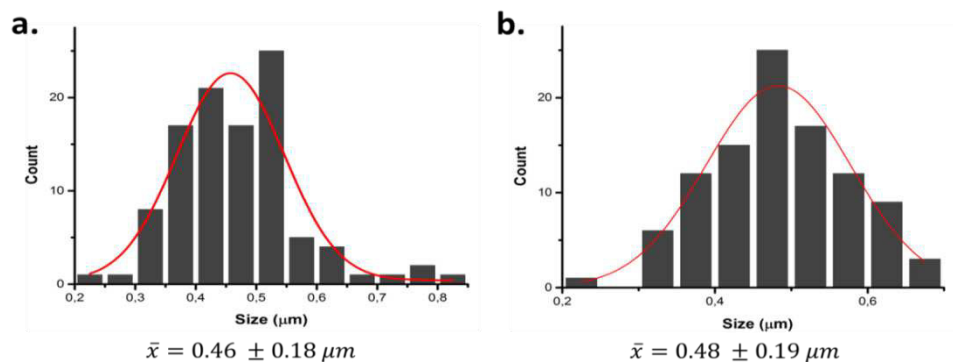
Figure 4.24. *Size distribution of BT-C ceramics sintered in reducing atmosphere. (**a**) BT-C_1.5_sint., and (**b**) BT-C_2_sint.*

- **Structure and phase composition**

In the BT-C case, the doping concentrations are 1, 1.5 and 2 wt% Y_2O_3. The BT-C_1 ceramics (Fig. 4.25.a) crystallize in the tetragonal phase. No secondary phase or phase transitions are observed. The structure does not vary with the post-sintering conditions. In the case of BT-C_1.5 (Fig. 4.25.b) and BT-C_2 (Fig. 4.25.c) ceramics, the XRD analyses evidence the decrease of the tetragonality. The enlargements of peaks around 45° show how the (002) peak becomes less intense and seem to be joined with the (200).

The pyrochlore $Y_2Ti_2O_7$ is detected in BT-C_1.5 and BT-B_2 ceramics. This secondary phase is also observed in the X-ray diffraction patterns of the ceramics issued from BT-B powders with same dopant concentrations. Also, it is worth to mention that apparently the presence of the $Y_2Ti_2O_7$ phase improves the densification (Fig. 4.17 and Fig. 4.22) probably because it has a lower melting point (1580 °C) than $BaTiO_3$ (1625 °C).

Figure 4.25. *XRD patterns of BT-C powder and ceramics sintered in reducing atmosphere and re-oxidized. Lateral enlargements of zone around 45° are presented.*

Finally, a comparison of the characteristics of the different ceramics issued from BT-A, BT-B and BT-C powders and sintered in reducing atmosphere is presented. The density value of each group of ceramics is reported in Fig. 4.25 according to the dopant level. The BT-A_0 ceramic exhibited the highest density being close to the value for BT-B and BT-C ceramics with dopant level from 1 to 2 wt%. 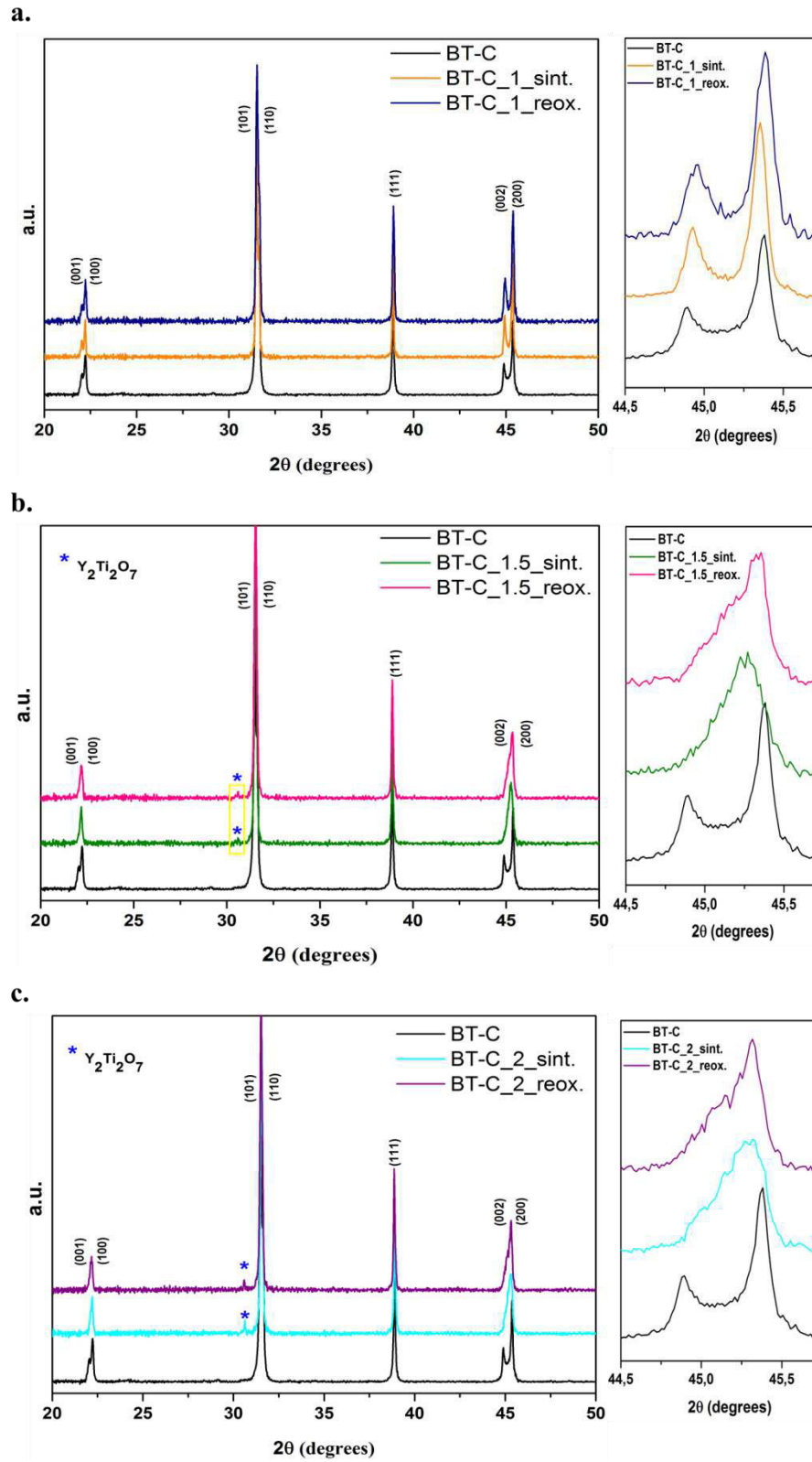In fact, the density of this group of doped ceramics is roughly different, as can be observed in this figure. Regarding the ceramics issued from BT-A with the same dopant level, the density of them compared to the one of the BT-B and BT-C ceramics is considerably different, being 20 and 30 % respectively lower. Additionally, the density of BT-B ceramics with dopant level between 2.5 and 20 wt% is again higher than the one for the BT-A ceramics with the same Y_2O_3 concentration. However, there is a divergence in the behavior of the density as a function of the $[Y_2O_3]$ between BT-A and BT-B ceramics. First, the density of BT-A_1.5 and BT-A_2 is quite equal. Beyond this dopant concentration, it slightly increases and is practically the same for BT-A_2.5, BT-A_5, and BT-A_20. Otherwise, even when the BT-B_1.5 and BT-B_2 have fairly the same density, as in the BT-A case, the behavior of it beyond this dopant level is opposite to the observed in the BT-A ceramics. For these ceramics (BT-B_2.5, BT-B_5, and BT-B_20) the density values decrease when the concentration of Y_2O_3 increases (although the density is rather the same for the three). Not with standing, it was determined that the densification was below 95% in all cases.
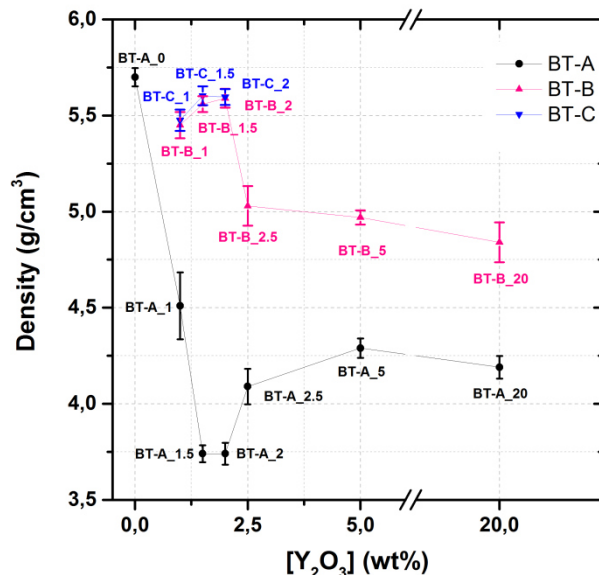
Figure 4.26. *Density values of ceramics sintered in reducing atmosphere at 1310 °C as a function of Y_2O_3 in the starting powder.*

Moreover, the density of ceramics issued from the same powders but sintered under different atmosphere is also different. The ceramics sintered under reducing atmosphere present higher values than the ones fired in air. The atmosphere plays a role in densification mechanism. In fact, when samples are sintered in air, more oxygen vacancies are created which derive in larger volumes and therefore lower densities.

The crystalline structure for all the ceramics obtained in this work is tetragonal. Nonetheless, the tetragonality of the BT is certainly decreased by the incorporation of Y^{3+} ions. As a matter of fact, the increment of its concentration causes stronger modifications on the lattice parameters. In the same way, the introduction of the Y^{3+} in the BT lattice promoted the formation of secondary phases. Indeed, the high levels of doping used in this work were set with the intention to drive the system to it. Y^{3+} replaces Ba^{2+} and Ti^{4+} sites and when the solubility limit in both sites is surpassed, secondary phases can be produced. Of course, the incorporation of Y^{3+} is also markedly affected by the processing conditions and the composition of the raw BT. As seen in this work, the sintering atmosphere played a role in the formation of secondary phases. While in the ceramics fired in air,

only the Y_2O_3 is detected besides the $BaTiO_3$ phase. In the ceramics sintered under reducing conditions various phases besides those were identified. A recall of the phase composition for reduced ceramics is given in Table 4.12. The differences in the degree of secondary phases formation regarding the firing atmosphere are related with the higher degree of substitution of the RE ions when a reducing atmosphere is used. These conditions promote the formation of oxygen vacancies increasing the diffusion of the ions into the system, and leaving as well Ba^{2+} and Ti^{4+} ions free to react among them and with the excess of dopant, forming Ti-rich phases as the ones detected in this work. Therefore, even when no liquid phase was present during the sintering process, the surface diffusion of the ions contributed highly with the precipitation of additional phases. Also, we consider that the interaction of the additives with the BT-matrix and the sintering conditions favored the surface diffusion for above the volume diffusion because not significantly changes in the grain size of the samples were observed.

Table 4.12. Summary of secondary phases detected in ceramics sintered in reducing atmosphere and 1310 °C.

BaTiO$_3$ raw material	Y$_2$O$_3$ wt%	Sample ID	Secondary phases
BT-A (reagent-grade)	0	BT-A_0	x
	1	BT-A_1	x
	1.5	BT-A_1.5	x
	2	BT-A_2	Y$_2$Ti$_2$O$_7$
	2.5	BT-A_2.5	Y$_2$TiO$_5$
	5	BT-A_5	Y$_2$O$_3$; Y$_2$Ti$_2$O$_7$
	20	BT-A_20	sint. ceramic: Y$_2$Ti$_2$O$_7$; Y$_2$TiO$_5$. reox. ceramic: Y$_2$O$_3$; Y$_2$TiO$_5$.
BT-B (commercially formulated)	1	BT-B_1	x[a]
	1.5	BT-B_1.5	Y$_2$Ti$_2$O$_7$
	2	BT-B_2	Y$_2$Ti$_2$O$_7$
	2.5	BT-B_2.5	Y$_2$TiO$_5$
	5	BT-B_5	Ba$_6$Ti$_{17}$O$_{40}$
	20	BT-B_20	Y$_2$O$_3$; Ba$_6$Ti$_{17}$O$_{40}$
BT-C (commercially formulated)	1	BT-C_1	x
	1.5	BT-C_1.5	Y$_2$Ti$_2$O$_7$
	2	BT-C_2	Y$_2$Ti$_2$O$_7$

x: no secondary phases were discerned to the extent of the XRD detection limit.

Regarding the composition of the raw BT powders, the interaction of the rest of the additives and dopants can influence the results too. The A- and B-sites can be replaced not only by the amphoteric Y^{3+} ion but also by ions such as Ca^{2+} and Mg^{2+}, and their interactions will also affect the preference of a site by a specific atom. Their incorporation will also drive to an excess of ions such as the Ti^{4+} in the system, so the formation of secondary phases will be promoted also by the presence of the metal elements. In fact, the compositional design of the formulated powders used in this work included Mg^{2+} and Ca^{2+}. The Mg^{2+} has been reported to inhibit the grain growth because it tends to

segregate at the grain boundaries, improving the coalescence during sintering. Also, when it acts together with RE ions contributes to the formation of the "core-shell" structure which is highly desired to accomplish the MLCC specifications (Huang et al., 2015; Wang et al., 2014b). This will also require a careful control of the MgO/R_2O_3 ratio and the firing parameters (Kishi et al., 2003). In the same way, the Ca^{2+} is used to improve the MLCC reliability by limiting the concentration of oxygen vacancies (Yoon et al., 2010).

References

Ashburn, T., & Skamser, D. (2008, January). Highly accelerated testing of capacitors for medical applications. In *Proceedings of the 5th SMTA Medical Electronics Symposium*.

Belous, A., V'yunov, O., Kovalenko, L., & Makovec, D. (2005). Redox processes in highly yttrium-doped barium titanate. *Journal of Solid State Chemistry, 178*(5), 1367-1375.

Belous, A., V'yunov, O., Glinchuk, M., Laguta, V., & Makovez, D. (2008). Redox processes at grain boundaries in barium titanate-based polycrystalline ferroelectrics semiconductors. *Journal of materials science*, *43*(9), 3320-3326.

Huang, X., Liu, H., Hao, H., Zhang, S., Sun, Y., Zhang, W., & Cao, M. (2015). Microstructure effect on dielectric Properties of MgO-doped $BaTiO_3$–$BiYO_3$ ceramics. *Ceramics International, 41*(6), 7489-7495.

Kim, C. H., Park, K. J., Yoon, Y. J., Hong, M. H., Hong, J. O., & Hur, K. H. (2008). Role of yttrium and magnesium in the formation of core-shell structure of $BaTiO_3$ grains in MLCC. *Journal of the European Ceramic Society, 28*(6), 1213-1219.

Kishi, H., Mizuno, Y., & Chazono, H. (2003). Base-metal electrode-multilayer ceramic capacitors: past, present and future perspectives. *Japanese Journal of Applied Physics, 42*(1R), 1.

Koschek, G., & Kubalek, E. (1987). On the Electronic Structure and the Local Distribution of the Second Phase $Ba_6Ti_{17}O_{40}$ in $BaTiO_3$ Ceramics. *Physica status solidi (a), 102*(1), 417-424.

Liu, G., & Roseman, R. D. (1999). Effect of BaO and SiO_2 addition on PTCR $BaTiO_3$ ceramics. *Journal of Materials science, 34*(18), 4439-4445.

Lu, H. Y., Bow, J. S., & Deng, W. H. (1990). Core-Shell Structures in ZrO_2-Modified $BaTiO_3$ Ceramic. *Journal of the American Ceramic Society*, 73(12), 3562-3568.

Makovec, D., Samardžija, Z., & Drofenik, M. (2004). Solid solubility of holmium, yttrium, and dysprosium in $BaTiO_3$. *Journal of the American Ceramic Society, 87*(7), 1324-1329.

Öksüz, K. M., Torman, M., Şen, S., Şen U. (2016). Effect of sintering temperature on dielectric properties of SiO_2 doped $BaTiO_3$ ceramics. *Materials, Methods & Technologies, 10*, 361-366.

Paredes-Olguín, M., Lira-Hernández, I. A., Gomez-Yañez, C., & Espino-Cortes, F. P. (2013). Compensation mechanisms at high temperature in Y-doped BaTiO$_3$. *Physica B: Condensed Matter*, *410*, 157-161.

Tsur, Y., Dunbar, T. D., & Randall, C. A. (2001). Crystal and defect chemistry of rare earth cations in BaTiO$_3$. *Journal of electroceramics, 7*(1), 25-34.

V'yunov, O. I., Kovalenko, L. L., Belous, A. G., & Belyakov, V. N. (2005). Oxidation of reduced Y-doped semiconducting barium titanate ceramics. *Inorganic Materials, 41*(1), 87–93. Translated from *Neorganicheskie Materialy, 41*(1), 93–100.

Wang, M. J., Yang, H., Zhang, Q. L., Hu, L., Yu, D., Lin, Z. S., & Zhang, Z. S. (2014a). Doping behaviors of yttrium, zinc and gallium in BaTiO$_3$ ceramics for AC capacitor application. *Journal of Materials Science: Materials in Electronics*, *25*(7), 2905-2912.

Wang, M. J., Yang, H., Zhang, Q. L., Lin, Z. S., Zhang, Z. S., Yu, D., & Hu, L. (2014b). Microstructure and dielectric properties of BaTiO$_3$ ceramic doped with yttrium, magnesium, gallium and silicon for AC capacitor application. *Materials Research Bulletin, 60*, 485-491.

Wu, Y. C., Wang, S. F., McCauley, D. E., Chu, M. S., & Lu, H. Y. (2007). Dielectric Behavior and Second Phases in X7R-Formulated BaTiO$_3$ Sintered in Low-Oxygen Partial Pressures. *Journal of the American Ceramic Society, 90*(9), 2926-2934.

Yoon, S. H., Park, Y. S., Hong, J. O., & Sinn, D. S. (2007). Effect of the pyrochlore (Y$_2$Ti$_2$O$_7$) phase on the resistance degradation in yttrium-doped BaTiO$_3$ ceramic capacitors. *Journal of Materials Research, 22*(9), 2539-2543.

Yoon, S. H., Kang, S. H., Kwon, S. H., & Hur, K. H. (2010). Resistance degradation behavior of Ca-doped BaTiO$_3$. *Journal of Materials Research, 25*(11), 2135-2142.

Yuan, Y., Zhang, S., & Li, C. (2004). The effect of doping process on microstructure and dielectric properties of BaTiO$_3$-based X7R materials. *Journal of Materials Science: Materials in Electronics, 15*(9), 601-606.

Zhang, J., Hou, Y., Zheng, M., Jia, W., Zhu, M., & Yan, H. (2016). The occupation behavior of Y$_2$O$_3$ and its effect on the microstructure and electric properties in X7R dielectrics. *Journal of the American Ceramic Society, 99*(4), 1375-1382.

Zhi, J., Chen, A., Zhi, Y., Vilarinho, P. M., & Baptista, J. L. (1999). Incorporation of yttrium in barium titanate ceramics. *Journal of the American Ceramic Society*, *82*(5), 1345-1348.

Conclusion

General Conclusion and Perspectives

The objective of this thesis work was to analyze the behavior of $BaTiO_3$ doped with Y_2O_3. This issue was addressed by two distinct yet related perspectives. The barium titanate (BT) powders that are used in formulations for dielectric materials of multilayer ceramic capacitors (MLCCs) contain different additives and dopants to enhance it electrical properties. However, sometimes the dopants can lead to the formation of secondary phases that are believed responsible for the detriment in the insulation resistance of the MLCCs. One of the most common and suitable dopants is the Y_2O_3, which is related to secondary phases of the pyrochlore type, $Y_2Ti_2O_7$.

In this way, a first approach was made by the electrical characterization of MLCCs of the X7R type, which composition is based on $BaTiO_3$ doped with 1.05 % of Y_2O_3. The characterization of three different groups (A, B and C) of MLCCs was performed by means of high life accelerated tests (HALT) that allowed gathering the data related to its mean time to failure (MTTF). Statistical analyses were performed using the Weibull distribution and then associating the found parameters with the Arrhenius model to determine the activation energy related to the failures produced under controlled conditions. The discrimination of the three groups of samples according to its behavior under the stress tests was achieved. It was evidenced by the time-to-failure (TTF) of the samples under combined stress tests that the Group A appears to be the more reliable followed by the Group B and at least the Group C, which was found to be the most affected by the high stress conditions. Combined tests at different levels of thermal and electrical stress were performed with the aim to determine if the failure of the samples changed at higher levels. It was evidenced that at higher temperatures the expected life of the capacitors is decreased, and a higher value of voltage produces this effect as well. For the Groups A and B, the failures seem to have the same mechanism(s) in a

temperatures range of 100 - 200 °C when tested at 400 and 600 V. Meanwhile, the Group C present this behavior but in a much lower range of 20 – 90 °C. This was reflected thorough the analyses of the time-to-failure (TTF) data using the Weibull distribution, since the plots obtained for these conditions presented a similar behavior. Then, it was possible to determine the activation energy (E_a) value for each set of testing conditions and it was found that at 400 V the Group A has the lower value of E_a (1.06 $\pm$ 0.08 eV) which indicates and confirms that the applied stress has lower effect over this Group compared with the Group B (E_a = 1.25 $\pm$ 0.05 eV) and the Group C (E_a = 1.45 $\pm$ 0.06 eV). Hence, when the electrical stress is 400 V, the Group C is expected to have the life time that will change more rapidly as the temperature changes. On the other hand, when a higher voltage was applied (600 V) even though the TTF observed were lower compared to the ones obtained at 400 V, the activation energy determined was not significantly different for the three groups. However, the values were found to be lower than for the testing conditions at 400 V in the cases of the Group B (E_a = 1.09 $\pm$ 0.02 eV) and the Group C (E_a = 1.08 $\pm$ 0.02 eV). The Group A a similar activation energy despite the higher electrical stress (E_a = 1.01 $\pm$ 0.09 eV), which once again can be an indication of its higher stability compared to the other two groups. Even though the failure mechanisms were not determined, with the determined values for the activation energy related to them is possible to say that since they are above the same for the three groups of samples, this could imply that despite their compositional differences and the way they are affected by the high values of stress, they fail under the same mechanism(s).

In general, the electrical characterization of MLCCs samples was possible, associating an E_a value to the breakdowns and observing the influence of high stress values over the reliability of the samples. This part of the work also allowed us to set-up an in-house device that was completely developed at the LAPLACE laboratory and can be used for the performance of high accelerated life tests over MLCCs in an accurate way to obtain information about its expected life time to use it and relate it with the failure modes and the reliability of the samples. Also, bearing in mind that the

principal differences among these groups of capacitors are given by the composition of its dielectric material i.e., the amount of additives and dopants, these results provided information to confirm that the samples will have different properties (i.e., insulation resistance) according the composition of the dielectric ceramic formulation.

The following step of the study was to evaluate the possibility of the secondary phases' formation due to the presence of Y_2O_3 as dopant. Since it is not the only dopant found in the MLCCs dielectric formulation, the role of the Y_2O_3 as dopant was evaluated in a reagent grade BT powders and two industrially formulated BT powders with the aim to see the interactions that can be given in a BT-Y_2O_3 system and a BT-Y_2O_3-additives/dopants system. The formulated starting powders used for this part, were the same that have been applied in the manufacturing of MLCCs pieces corresponding to the Groups B and C characterized in the first part. Thus, powders and ceramics with different Y_2O_3 concentrations were prepared and subsequently thermally treated or sintered, respectively. Heat treatment of powders was conducted on air, while sintering of ceramics was carried out both, in air and reducing atmosphere. It was evidenced that the crystalline structure of $BaTiO_3$ can be affected by the Y^{3+} presence either in powders or ceramics, being more noticeable when Y^{3+} doping level increases. Also, under some conditions, the formation of secondary phases was promoted, being identified the $Ba_6Ti_{17}O_{40}$, Y_2TiO_5 and $Y_2Ti_2O_7$. These results provide an insight about the behavior of Y^{3+} when it is used as $BaTiO_3$ dopant in high levels. Plus, it the results provide clear evidence that the interactions among additives used in a commercial formulation are quite important and play a role in the final properties and the formation of secondary phases as well.

This work evidences that the BT-based formulations for dielectric applications are very sensitive to the most slightly changes in its compositions and this can lead to important changes of the final properties of the material and the reliability of the same. Other perspectives may be considered in order to have a more accurate study to describe the real role of other additives and dopants and especially the interactions they may have in real systems under the conditions used in their different

applications. Performing an electrical characterization of the MLCCs samples used in this work aiming to determine its failure mechanism(s) could give interesting information about the properties of the dielectric material.